Coherence and polarization of polariton condensates created in the optical parametric oscillation regime

PhD Thesis

Jorge Cuadra

Advisor:

Prof. Luis Viña

Submitted for the degree of

Doctor of Philosophy

Universidad Aútonoma de Madrid

Departamento de Física de Materiales

March, 2014

To my family....

experiencia es lo que se obtiene cuando
piensas que no has obtenido nada

Acknowledgment

First I would like to thanks to my advisor Prof. Luis Viña who trusted on my potential to carry on the research within the SEMICUAM group, the constant support to my daily labor, the good willing to answer any doubt, and especially his concern to any matter not related with the research. Many people have taken part in this work, I would like mention them: Christoph Lingg, Dr. Rita Spano who guided me on the arrival to the laboratory, Dipankar Sarkar who re-joined the group during my final year and supported my day to day labor. The interaction with people among the group Prof. José Manuel Calleja, Dr. M. Dolores Martín, Guilherme Tosi, Carlos Antón, that undoubtedly broadened my point of view regarding the performed research.

I am deeply thankful of the collaboration with the group of Prof. Guillaume Malpuech who modeled our experimental results.

I would like to thanks Prof. Jϕrn M. Hvam for provided the microcavity structure.

Also Prof. P. G. Lagoudakis, who kindly welcome me on a research stay at his group, where the influence of magnetic fields on microcavity-polaritons were studied.

Also people who cheered up my lunch-time with fascinating non-physics related discussion: Carlos, Juancho, Jose Luis, Guille and Dipi.

Special thanks goes to Valentín Guadaño who always solved the problems with our lasers.

This thesis has been funded by the European community through the grant FP7 Spin-optronics project N$^{\underline{o}}$ 237252 and the Spanish grant CAM (S-2009/ESP-1503).

Finally I would like to thanks to all members of the Departamento de Física de Material.

Publications

"Polarized emission in polariton condensates: Switching in a one-dimensional natural trap versus inversion in two dimensions"
J. Cuadra, D. Sarkar, L. Viña, J. M. Hvam, A. Nalitov, D. Solnyshkov, and G. Malpuech.
Phys. Rev. B 88, 235312 (2013).

"Quantum reflections and shunting of polariton condensate wave trains: Implementation of a logic AND gate"
C. Antón, T. C. H. Liew, J. Cuadra, M. D. Martín, P. S. Eldridge, Z. Hatzopoulos, G. Stavrinidis, P. G. Savvidis, and L. Viña.
Phys. Rev. B 88, 245307 (2013).

"Build up of off-diagonal long-range order in microcavity exciton-polaritons across the parametric threshold"
R. Spano, J. Cuadra, C. Lingg, D. Sanvitto, M. D. Martin, P. R. Eastham, M. van der Poel, J. M. Hvam, and L. Viña.
Opt. Express 21, 10792 (2013).

"Coherence properties of exciton polariton OPO condensates in one and two dimensions"
R. Spano, J. Cuadra, G. Tosi, C. Antón, C. A. Lingg, D. Sanvitto, M. D. Martín, L. Viña, P. R. Eastham, M. v. d. Poel, J. M. Hvam.
New J. Phys. 14, 075018 (2012).

Nomenclature

α_1	constant interaction for parallel spins
α_2	constant interaction for antiparallel spins
δW	relative difference between the scattering amplitudes (see Eq. 4.5)
δ	cavity-exciton detuning
Δ_C	cavity TE-TM splitting
Δ_P	polariton TE-TM splitting
Δ_X	exciton TE-TM splitting
ϵ_0	vacuum dielectric constant
γ_C	photon decay rate
γ_X	exciton decay rate
$\hbar$	Planck constant over π
λ	wavelength
λ_{dB}	de Broglie wavelength
$\mathbf{e}_x$	unit vector along x-axis of the Poincare sphere (see Eq. 4.5)
$\mathbf{S}_k$	in-plane polariton pseudo-spin (see Eq. 4.4)

ω	frequency of light times 2π
Ω_R	Rabi splitting
ψ	photonic fraction (see Eq. 4.1)
ρ_C	circular degree of polarization
ρ_D	degree of polarization in a diagonal basis
ρ_L	linear degree of polarization
τ_c	time scale related with the energy distribution (see § 3.1.2)
τ_r	time scale related with fluctuations (see § 3.1.2)
θ	incidence angle
φ	excitonic fraction (see Eq. 4.1)
$\vec{S}$	Stokes vector
a_B	Bohr radius
$a_k^\dagger$	photon creation operator
$b_k^\dagger$	exciton creation operator
bcc	body centered cubic
BEC	Bose Einstein Condensate
c	speed of light
C_B	Conduction band
DBR	distributed Bragg reflector
DLP	degree of linear polarization

e	electron charge
E_C	in-plane photon energy
E_g	Energy gap
E_X	in-plane exciton energy
E_{bind}	exciton binding energy
E_{LPB}	Lower Polariton Branch energy
E_{Th}	energy threshold
E_{UPB}	Upper Polariton Branch energy
f	noise (spontaneous scattering) (see Eq. 4.1)
fcc	face centered cubic
FP	Fabry-Perot
$g^{(1)}$	first order correlation function
g_X	particle-particle interactions constant (see Eq. 1.22)
$GaAs$	Gallium-Arsenide
H_x	effective magnetic field (see Eq. 4.1)
K	exciton center of mass wavevector
k	wavevector
$k_{\parallel}$	in-plane wavevector
L_C	cavity lenght
L_{eff}	effective cavity length

m_C	cavity mass
m_X	exciton mass
m_{band}	mass of the band
m_{conf}	mass in the confinement direction
m_{LPB}	lower polariton mass
m_{UPB}	upper polariton mass
n_C	cavity refractive index
$N_{k\uparrow,\downarrow}$	z projections of the polariton population (see Eq. 4.3)
N_{QW}	number of quantum wells
$ODLRO$	Off-diagonal long-range order
OPA	Optical parametric amplifier
OPO	Optical parametric oscillator
P_d	power density (see § 3.1.2)
p_k	lower polariton operator
P_{Th}	power threshold
q_k	upper polariton operator
QW	Quantum Well
S_1	linear Stokes parameter
S_2	diagonal Stokes parameter
S_3	circular Stokes parameter

T_C	coherence time (see § 3.1.2)
TE	transverse electric
TM	transverse magnetic
U	photonic confinement potencial (see Eq. 4.1)
V_B	Valence band
$V_C\left(r\right)$	potencial affecting the photons (see Eq. 1.22)
X_k, C_k	Hopfield coefficients
Γ_0	exciton radiative decay rate
FWHM	Full Width at Half Maximum

List of Figures

Contents

Abstract

This thesis presents optical studies of a *GaAs* based microcavity in which strong coupling between quantum well excitons and confined photons is observed. In the strong coupling regime, the system is neither described by excitons nor photons, but rather by new eigenmodes called polaritons. This mixed modes inherit characteristics of both components: they are bosons, since their constituents are bosons, therefore they are able to occupy a single energy quantum state; they have a very light mass compared with that of the electron mass; they interact with each other via Coulomb interaction. The latter porperty together with the particular shape of the lower polariton branch allow to obtain optical parametric oscillator (OPO) behavior in microcavity polaritons. In the optical parametric oscillation regime in microcavity-polaritons two pumped polaritons interact via Coulomb interaction and scatter towards states that have low and high energies and momenta, fulfilling phase matching conditions. Above a certain pump power threshold, three states are massively occupied: pump, signal and idler. This is the situation that is presented is this thesis.

In particular two properties that attract great interest are addressed: phase correlation and polarization properties, both allow to get a deep inside sigth into the characteristic behavior of a massively occupied state by the OPO process in microcavity exciton-polaritons.

Chapter 1 introduces the physics behind the exciton-polaritons and the condensation. It starts with a general review of semiconductors band structure. This is followed by a description of the polariton constituents: the confined photons and the quantum well excitons. Then the new eigenmodes that arise from the mixed exciton-photon are introduced, together with its main properties. Moreover, the concepts behind the Bose Einstein condensation are introduced and finally a few of the more remarkable achievements in the field of polaritons are presented.

Chapter 2 describes the sample used in this work and as well as the experimental setups and techniques implemented during this thesis. Firstly, the characteristic of the microcavity structure are presented, it follows a detailed description of the pump laser. Then the imaging techniques are introduced both for real and momentum space. Later the interferometers built during this thesis and the procedure to retrieve the first order correlation function together with the phase of the condensates are described. Finally, the setup used in the polarization resolved measurements is detailed.

Chapter 3 reports the coherence properties of the condensates, both spatial and temporal coherence properties are studied for different regimes. One of the aims is to demonstrate that OPO polariton condensates present spontaneous extended spatial coherence. In order to do so, different pumping power regimes are investigated: diverse behaviors are found for pump powers below, slightly above and well above condensation threshold. Also a particular situation when the microcavity is excited above the condensation power threshold is investigated, in this situation the threshold is defined as a function of the laser's energy and the influence of the laser energy tuning, with respect to phase matching conditions, on the coherence properties is unveiled.

Furthermore the presence of undesired effects caused by the growth process are exploited: the last part of Chapter 3 deals with the coherence properties of a hybrid 2D-1D system composed by a wire-like defect surrounded by a 2D planar structure.

Chapter 4 deals with the polarization properties of the OPO process in polariton condensates, these are studied in the system consisting of the hybrid 2D-1D condensates where selective excitation of either the 1D solely or the composed 2D-1D system can be achieved. In both cases the polarized emission depends on the orientation of the polarization's plane of the pump laser but there are marked differences on this dependence for the 2D and 1D systems. The results are theoretically explained, by the group of G. Malpuech, using two complementary models: a spinor Gross-Pitaevskii equation and a semi-classical Boltzmann model.

Resumen

Esta tesis presenta estudios ópticos de una microcavidad de *GaAs* en la cual existe el acoplamiento fuerte entre excitones de un pozo cuántico y fotones confinados. En el régimen de acoplamiento fuerte, el sistema se describe por nuevas cuasi-partículas llamadas polaritones que son una mezcla de excitones y fotones. Los nuevos modos heredan características de los dos componentes: son bosones, ya que sus constituyentes también lo son; tienen una masa muy pequeña comparada con la masa del electrón; interactúan a través de la interacción de Coulomb. La última característica junto con la forma particular de la rama polaritonica inferior permiten conseguir oscilación paramétrica óptica (OPO) en polaritones. En este proceso dos polaritones interactúan a través de la interacción de Coulomb y se dispersan hacia estados con mayor y menor energía y momento, satisfaciendo las condiciones de ajuste de fase. Por encima de cierto umbral para la potencia de bombeo hay tres estados masivamente ocupados: el bombeo, la señal y el ocioso ("idler"). Esta es la situación que se estudia en esta tesis.

En particular se investigan dos de sus propiedades que atraen gran interés actualmente: las correlaciones de fase y las propiedades de polarización. Ambas permiten obtener un conocimiento profundo sobre el comportamiento característico de un estado ocupado masivamente por el proceso OPO en polaritones de microcavidad.

El Capítulo 1 introduce la física que yace detrás de los polaritones de excitones y de la condensación. Comienza con una revisión general de la estructura de bandas en semiconductores, seguido de una descripción de los constituyentes de los polaritones: los fotones confinados y los excitones de pozo cuántico. A continuación se introducen los modos que aparecen como consecuencia de la mezcla entre el excitón y el fotón junto con sus principales propiedades. Además se presentan los conceptos que dan lugar a la condensación de

Bose Einstein. Finalmente se comentan algunos de los hitos más importantes logrados en polaritones.

En el Capítulo 2 se describe la muestra utilizada en este trabajo así como las técnicas experimentales implementadas y usadas a lo largo de esta tesis. En primer lugar se presentan las características de la microcavidad, seguida por una descripción detallada del láser de bombeo. A continuación se introducen las técnicas de adquisición de imágenes utilizadas en el espacio real y en el espacio de momentos. A esto le sigue una descripción de los interferómetros construidos y del procedimiento para obtener la función de correlación y la fase. Finalmente se presenta el montaje experimental usado para las medidas resueltas en polarización.

En el Capítulo 3 se exponen las propiedades de coherencia del condensado OPO. Sus propiedades de coherencia temporal y espacial se estudian en diferentes regímenes. Uno de los objetivos es demostrar que el condensado OPO presenta coherencia espacial extendida espontanea. Para conseguir esto, se investigan diferentes regímenes de la potencia de bombeo, encontrando diferentes comportamientos para potencias por debajo, apenas por encima y bastante arriba del umbral de condensación. También se investiga una situación particular cuando la microcavidad se excita por encima del umbral de condensación, en esta situación el umbral es definido en función de la energía del láser y se revela la influencia del ajuste de la energía del láser, con respecto a las condiciones de ajuste de fase, sobre las propiedades de coherencia.

A continuación se hace buen uso de la presencia de efectos no deseados causados por el proceso de crecimiento: en la última parte del Capítulo 3 se investigan las propiedades de coherencia de un sistema hibrido 2D-1D compuesto por un defecto de tipo hilo rodeado por una estructura 2D.

El Capítulo 4 presenta las propiedades de polarización del proceso OPO en condensados de polaritones. Estudiamos el sistema hibrido 2D-1D, que permite la excitación selectiva de o bien el sistema 1D únicamente o del sistema compuesto 2D-1D. En ambos casos la emisión polarizada depende de la orientación del plano de polarización del láser de bombeo, sin embargo existen diferencias marcadas en esta dependencia para los sistema 2D y 1D. Los resultados se explican teoréticamente, por el grupo de G. Malpuech, utilizando dos modelos complementarios: la ecuación de espinorial Gross-Pitaevskii y un modelo de Boltzmann semiclásico.

Chapter 1

Introduction to exciton-polaritons

In this chapter we will give a detailed description of the physics behind microcavity exciton-polaritons. The strong light-matter coupling, which is the cornerstone for the existence of microcavity exciton-polaritons is addressed. Properties of the polaritons are pointed out, especially the parametric scattering. Then the physics underlaying the Bose-Einstein condensation is presented and finally some of the milestones achieved in exciton polaritons are reviewed.

1.1 Physics of semiconductors

Semiconductors are well characterized in the framework of solid state physics, since they are ordered periodical structures. In this context, a crystal can be properly described in terms of a unit cell (a_1, a_2, a_3) that allows to reproduce the whole structure by repeating this unit cell an integer number of times.

Thus in order to describe an electron in the periodical structure, it is convenient to write the electron's wavefunction as follows [1]:

$$\psi_{nk}(r) = u_{nk}(r)\, e^{ik\cdot r} \tag{1.1}$$

where $u_{nk}(r)$ is a periodic function (Bloch's function) that represents the periodicity of the

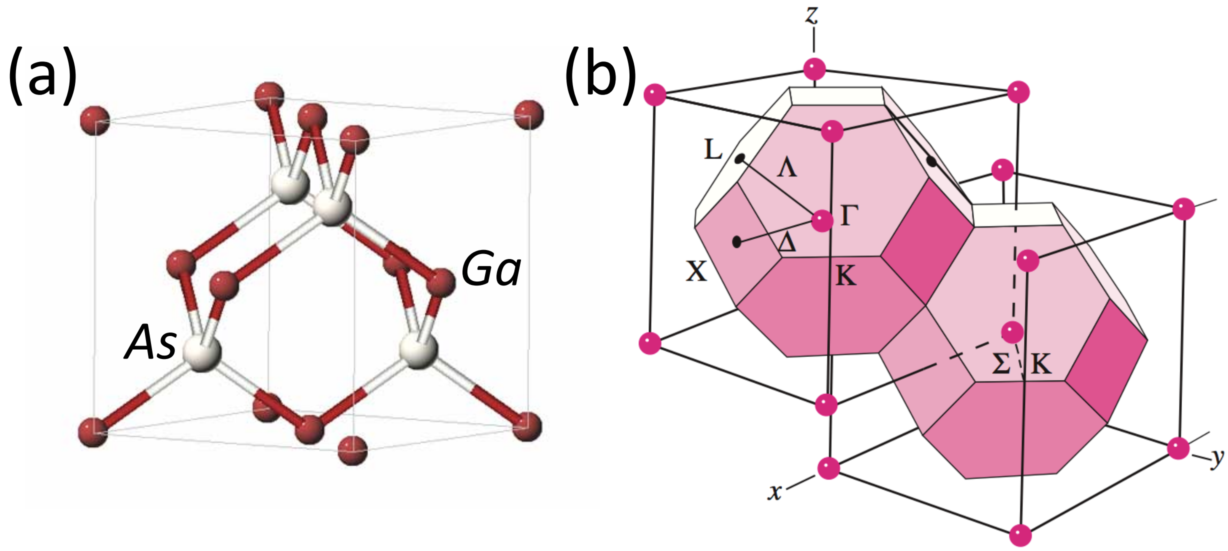

Figure 1.1: Crystal structure in real and reciprocal spaces for $GaAs$. (a) shows the zinc-blende structure formed by the $GaAs$ compound constituting a two interpenetrating fcc. (b) represents the first Brillouin zone, where a few symmetry points have been labeled (adapted from [2]).

crystal, n is an index that represents the band state and k is the electron's wavevector. If the crystal characteristic lateral size is L, and a is the lattice constant ($L = Na$, where N is the number of atoms along the lateral crystal direction), for any linear combination of unit cells, Eq. 1.1 imposes the following constrain for the k vector, $k = \left(\frac{2\pi n}{Na}\right)$, where n can only take values within $\left[-\frac{N}{2}, \frac{N}{2}\right]$, this limits k to $\left[-\frac{\pi}{a}, \frac{\pi}{a}\right]$. The k vectors contained in this range define the first Brilloiun zone which is the unit cell in reciprocal space.

The structures studied in this thesis are made of binary, Gallium-Arsenide ($GaAs$), and ternary, $Al_xGa_{1-x}As$ alloys, which belong to the zinc-blende crystal structure, shown in Fig. 1.1(a). The lattice consists of two interpenetrating face-centered-cubic (fcc) lattices, where Arsenic atoms are put in one fcc lattice and Gallium or Aluminum atoms are placed in the other. The reciprocal lattice of an fcc lattice is a body-centered-cubic (bcc) lattice [see Fig. 1.1(b)]. Points with high symmetry are represented by greek capital letters in the first Brillouin zone, the center ($k = 0$) is denoted by Γ. Few of those points are shown in Fig. 1.1(b).

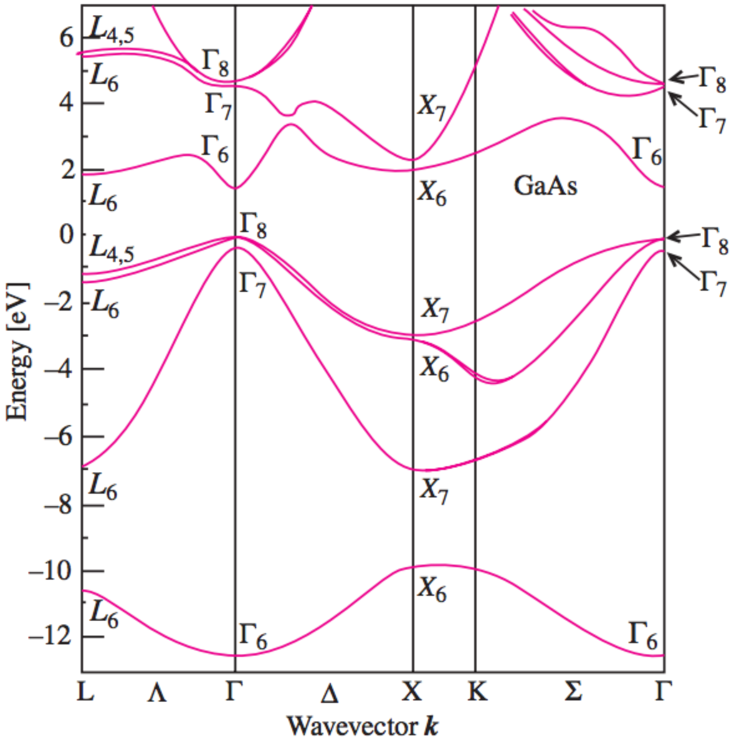

Figure 1.2: Band structure for a *GaAs* structure (adapted from [2]).

In a semiconductor structure there is an energy gap (E_g) between the valence band (V_B), defined as the occupied energy states at zero temperature (the highest occupied energy state is called the Fermi level), and the conduction band (C_B) states where electrons can freely move through the crystal lattice. Figure 1.2 shows the band structure for *GaAs*. The bandgap is direct in *GaAs*, *i.e.* the minima of the valence and of the conduction band are at the same k vector.

At the Γ point the conduction band has an s orbital character ($l = m_l = 0$), so taking into account the electron spin ($s = \pm 1/2$) the band is two-fold degenerated. On the other hand, the valence band has a p orbital character ($l = 1, m_l = 0, \pm 1$), thus, including the electron spin (but neglecting the spin-orbit coupling), the band would be six-fold degenerated. By taking into account the spin-orbit coupling the degeneracy is partially lifted into the Γ_8 and Γ_7 bands (see Fig. 1.2).

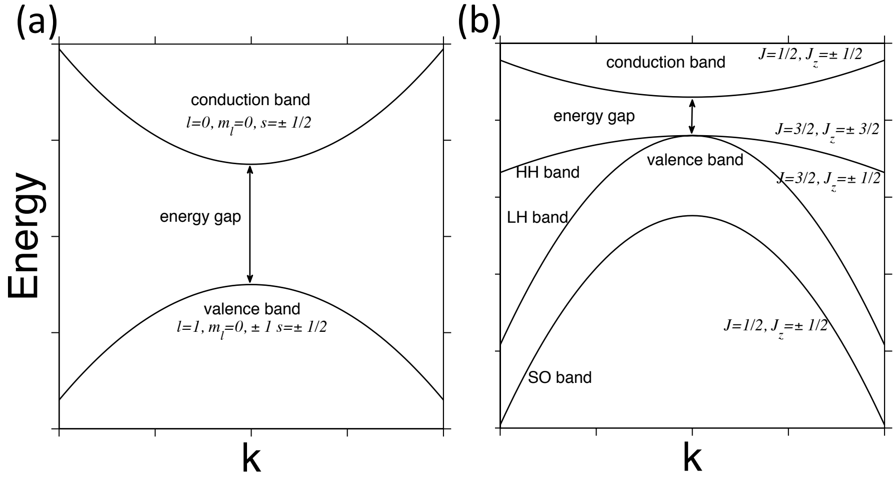

Figure 1.3: Scheme of band structure. (a) Shows the case where the spin-orbit coupling has not been considered, while (b) represents the band structure including spin-orbit coupling

The total angular momentum ($J = l + s$) for the lowest conduction band (Γ_6 band) is $J = \frac{1}{2}$, and considering the third components of the angular momentum $J_z = \pm\frac{1}{2}$, the conduction band results in two states represented as $| \frac{1}{2}, \pm\frac{1}{2} >$. In the valence band the situation is more complex, the total angular momentum is $J = \frac{3}{2}, \frac{1}{2}$, with third components $J_z = \pm\frac{3}{2}, \pm\frac{1}{2}$ for the total angular momentum $J = \frac{3}{2}$ (Γ_8 band), and $J_z = \pm\frac{1}{2}$ for the total angular momentum $J = \frac{1}{2}$. It is convenient to separate the states with $J_z = \pm\frac{3}{2}$ and $J_z = \pm\frac{1}{2}$, since they present different curvatures as they move away from $k = 0$. The $| \frac{3}{2}, \pm\frac{3}{2} >$ is called heavy-hole band, while the $| \frac{3}{2}, \pm\frac{1}{2} >$ is dubbed as light-hole band. The next valence band with $J = \frac{1}{2}$, Γ_7, has third components $J_z = \pm\frac{1}{2}$ and is called the split-off band, since it is split from the heavy- and light-hole band by the spin-orbit interaction [2]. Figure 1.3(a) shows a scheme of the band structure of the conduction and valence band edges without considering the spin-orbit coupling. Figure 1.3(b) depicts a scheme of the band structure that takes into account the spin-orbit coupling.

When an electron is excited from the valence band to the conduction band, a vacancy is left in the valence band, this is described as a quasi-particle called a hole, it is positively charged and has an effective mass $\sim \left(\frac{\partial^2 E}{\partial k^2}\right)^{-1}$. Electrons and holes attract each other via

Coulomb interaction forming an electron-hole pair, dubbed exciton, this pair resembles the hydrogen atom where an electron is bounded to the nucleus. The energy of the exciton is given by:

$$E_X(K) = E_g - E_{bind} + \frac{(\hbar K)^2}{2m_X} \tag{1.2}$$

where E_{bind} is the binding energy of the exciton, $\hbar K$ is the momentum of the center of mass of the electron and hole system and m_X is the exciton effective mass. As it was mentioned before, there are two kind of bands in the valence band, therefore two types of excitons are present. The pseudospin of excitons (as usual, we will name spin, or pseudospin, to the third component of the exciton total angular momentum) is determined by the spin of their constituents, so it is ± 2 or ± 1 for heavy-hole excitons and ± 1 or 0 for light-hole excitons. The fact that excitons have integer spin is crucial since it identifies them as bosons, allowing them to be in the same quantum state.

Excitons can be optically excited by absorption of light with an energy higher than the energy gap. In order to observe these transitions, the momentum and angular momentum must be conserved. Since the momentum of the photon is negligible compared to the momentum of the electrons, only transitions with $\Delta k \sim 0$ fulfill this constrain. The angular momentum conservation, on the other hand, imposes that only the combinations $J_z^H = \frac{3}{2}$, $J_z^e = -\frac{1}{2}$ and $J_z^H = -\frac{3}{2}$, $J_z^e = \frac{1}{2}$ for the heavy-holes and $J_z^H = \frac{1}{2}$, $J_z^e = \frac{1}{2}$ and $J_z^H = -\frac{3}{2}$, $J_z^e = -\frac{1}{2}$ for the light-holes are optically allowed under circularly polarized excitation.

The exciton photon coupling is characterized by the oscillator strength that takes into account the probability transition rate associated to the exciton optical transition, it is defined by:

$$f^{osc} = \frac{2\omega m_X}{\hbar} \left| \left\langle u_v \middle| \vec{r} \cdot \vec{E} \middle| u_c \right\rangle \right|^2 \tag{1.3}$$

where ω is the light frequency, $\hbar$ is the Planck constant and $\left\langle u_v \middle| \vec{r} \cdot \vec{E} \middle| u_c \right\rangle$ is the valence conduction band matrix element, with $\vec{E}$ a unit vector indicating the polarization's direction of the electric field [3].

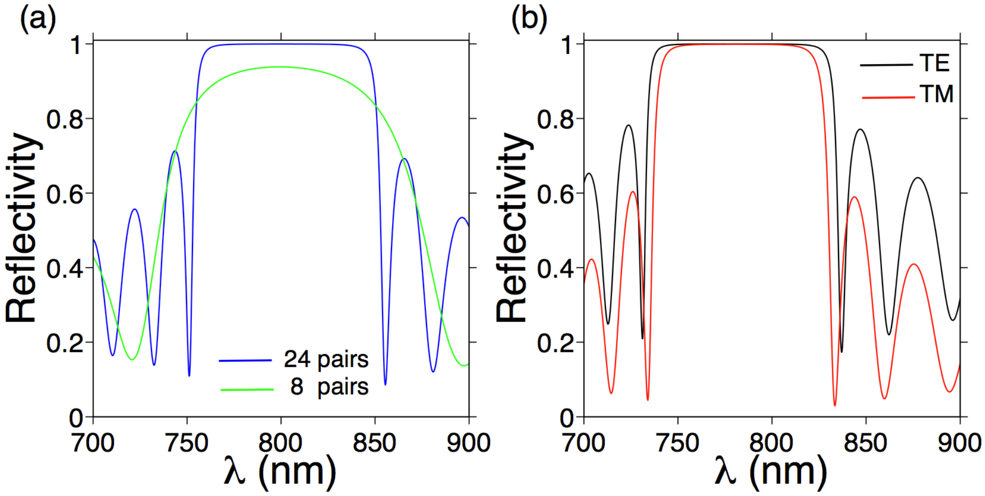

Figure 1.4: Reflectivity of Distributed Bragg Reflectors. (a) The green (blue) curve shows the reflectivity spectrum for a DBR structure composed by 8 (24) pairs of GaAs/AlAs for $\lambda_0 = 800\ nm$. (b) The spectrum in black (red) corresponds to an incident wave at 45º for a TE (TM) polarized wave for a structure composed by 24 layers. Curves calculated with the transfer matrix method [4].

1.2 Confinement of light and matter

1.2.1 Photons

The confinement of light can be achieved in a microresonator that resembles a Fabry-Perot (FP) cavity, where the cavity mirrors are distributed Bragg reflectors (DBR) and the cavity spacer is a dielectric material. A DBR is a periodic structure composed by alternating material layers with different refractive index (n_1 and n_2). The design of such structure has to fulfill the following condition $n_1 L_1 = n_2 L_2 = \lambda_0/4$ (λ_0 is the wavelength for which the DBR is designed), this ensures that the reflection in every interface constructively interfere, while the interference is destructive in transmission. The result is the formation of a stop-band where light cannot propagate perpendicular to the axis of the DBR. Figure 1.4(a) shows the reflectivity spectrum in green (blue) of a DBR structure composed by 8 (24) layers; as one can see, the reflectivity at the so-called stop-band increases with the number of layers.

For oblique incidence the reflectivity changes depending on the polarization of the electromagnetic field, for a transverse electric (TE) (the electric field oscillates in the plane of the DBR) polarized field, the spectrum is shown in Fig. 1.4(b) in black, meanwhile for a transverse magnetic (TM) (oscillation of the magnetic field in the plane of the DBR) polarized field, the spectrum is depicted by the red curve in Fig. 1.4(b), for an angle of incidence of 45º. This causes that the TE and TM modes split in energy and this splitting increases with the angle (k vector) [5].

Semiconductor microcavities are made by staking two DBR structures, that are the cavity mirror's, to a spacer, that itself acts as the cavity. This structure confines the electromagnetic field in the propagation direction (from now on z direction) and allows the free propagation in the transversal direction. The confinement imposes the following constrain to the allowed optical modes in the cavity:

$$k_z L_C = N\pi \tag{1.4}$$

where $k_z = \frac{2\pi}{\lambda_0} n_C$ is the wavevector along z, n_C is the refractive index of the cavity, L_C is the length of the cavity and N is an integer. In Fig. 1.5 the reflectivity spectrum for a $GaAs/AlAs$ based λ-cavity is shown, the central dip of the reflectivity depicts the resonance at 800 nm.

The energy of the cavity is given by $E_C = \hbar\omega$. It is convenient to write the dispersion relation:

$$E_C = \frac{\hbar c}{n_C}\sqrt{k_z^2 + k_\parallel^2} \simeq \frac{\hbar c}{n_C} k_z \left(1 + \frac{k_\parallel^2}{2k_z^2}\right) = E_0 + \frac{\hbar c}{2 n_C k_z} k_\parallel^2 \tag{1.5}$$

where c is the speed of light in vacuum, n_C is the cavity refractive index and $k_\parallel$ is the in-plane wavevector (k_y, k_y). This expression allows to write an effective photon mass, given by: $m_C = \hbar n_C k_z / c = 2\pi n_C \hbar / c\lambda_0$, which is of the order of $\sim 10^{-6} m_0$, where m_0 is the free electron mass.

The in-plane wavevector is related to the angle of incidence θ, defined with respect to the normal of the microcavity, of the electromagnetic field by:

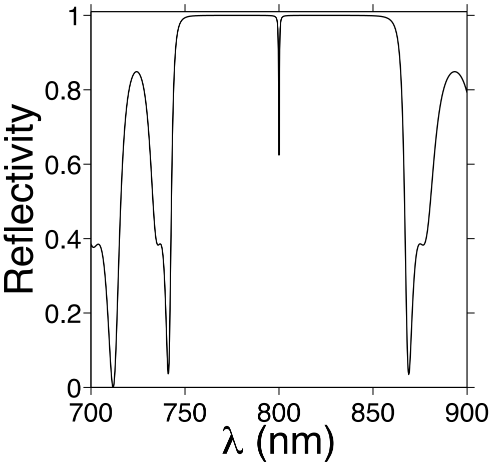

Figure 1.5: Fabry-Perot reflectivity. Reflectivity spectrum of a λ-cavity based on $GaAs/AlAs$.

$$k_{\parallel} = k \sin\theta\,;\; k = \frac{2\pi}{\lambda} \Rightarrow k_{\parallel} = \frac{\omega}{c}\sin\theta \tag{1.6}$$

where ω is the light frequency.

1.2.2 Quantum well excitons

Confinement strongly modifies the energy configuration of excitons. We will see later that it also has an important impact on the light-matter interactions. Excitons can be confined along one (quantum well), two (quantum wire) or three (quantum dot) dimensions.

A quantum well (QW) is formed by growing a thin layer of a material with some bandgap E_B sandwiched between two layers of a material with different bandgap E_A, as is shown in Fig. 1.6. In the growth direction, the confinement restricts the allowed k vectors, according to the following constrain $k_z = N\left(\frac{\pi}{L}\right)$, where L is the length of the embedded layer and N is an integer.

Therefore, the QW energy band is given by:

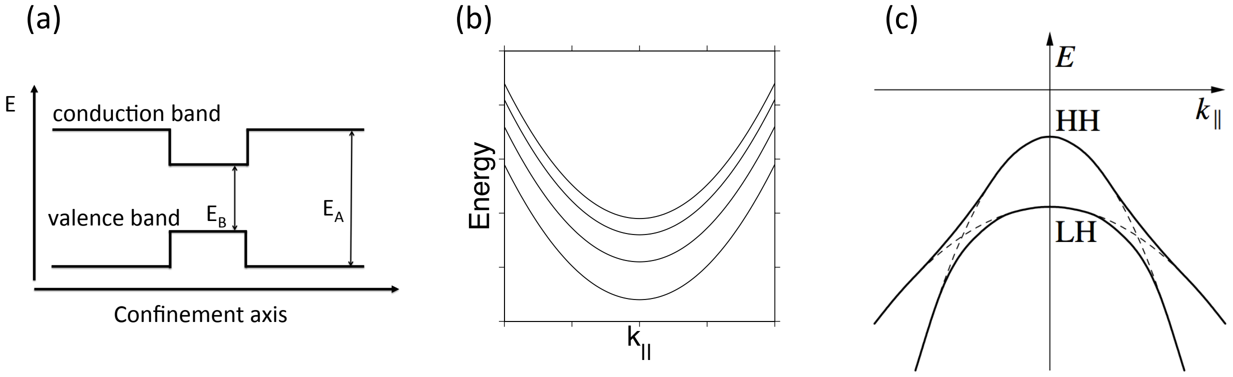

Figure 1.6: Scheme of quantum well structure. (a) shows a schematic draw of the QW for *GaAs* based materials. (b) The effect of the confinement is shown for the conduction band. (c) Dashed (continuos) line depicts the crossing (anticrossing) between the heavy and light hole bands (adapted from [7]). Note that the heavy (light)-hole band becomes light (heavy) in the plane of the QW.

$$E_{band}(k) = E_{bind} + \frac{(\hbar k_z)^2}{2m_{conf}} \left(\frac{\pi}{L}\right)^2 N^2 + \frac{(\hbar k_{\|})^2}{2m_{band}} \tag{1.7}$$

where the first term is the binding energy, the second one is the band energy in the confinement direction (for infinite high barriers, where m_{conf} is the mass in the confinement direction), and the third term is the band energy in the plane of the QW (m_{band} is the mass of the band). Both the conduction and valence bands open up into subbands [see Fig. 1.6(b)]. In the valence band the confinement lifts the degeneracy, since the heavy- and light-hole bands have different masses. As a result, the heavy-hole band has lower energy than the light-hole band. Moreover, a reversal of the heavy- and light-holes masses appears in the in-plane direction, that gives to the heavy-hole a lighter mass than the light hole for small k and therefore they would present a crossing at high k. Interaction between the bands leads to a significant mixing between them and anti-crossing can be observed [6, 7] [see Fig. 1.6(c)].

The optical excitation of QW excitons follows similar restrictions to those for bulk exciton. The in-plane momentum of the photon must be the same as the in-plane momentum of the exciton in the QW. Moreover conservation of angular momentum in the optical transitions imposes the same constrains as in the case of bulk excitons.

Excitons in QWs present a splitting in energy for non-zero momentum between states with dipole moment oriented along and perpendicularly to the wavevector, caused by the long-range exchange interaction between the electron and hole. This splitting increases with the k vector [8] and induces an effective magnetic field that makes excitons precess and therefore influences their spin relaxation processes [9].

1.3 Exciton-polaritons

In § 1.2 the effects of the confinement of light and matter were addressed, setting the basis to describe the coupling between those confined modes. The first report of polaritons formed by a confined exciton and photon modes in a semiconductor microcavity was done in Ref. [10].

When a radiative system is placed at the antinode of the electromagnetic field inside a FP-like cavity, its emission is enhanced, this is know as the Purcell effect [11]. Let us consider, for the sake of simplicity, that we have a two-level system, if the coupling between the two-level system and the electromagnetic field is enough, *i.e.* the energy exchange is faster than the decoherence mechanisms, the whole system is described by a superposition of the two-level system and the cavity mode. The situation is similar when a QW is placed at the anitnode of the cavity mode in a microcavity. From now on, we will describe this case.

In a quantum description, exciton and photon constitute a system of two bosonic oscillators coupled through light-matter interaction, the Hamiltonian describing the interaction is given by:

$$H = \sum_k \left[E_X(k)\, b_k^\dagger b_k + E_C(k)\, a_k^\dagger a_k + \hbar\Omega_R \left(b_k^\dagger a_k + a_k^\dagger b_k \right) \right] \tag{1.8}$$

where $b_k^\dagger$, b_k $\left(a_k^\dagger, a_k\right)$ are the creation and annihilation operator for the exciton (photon), $E_X(k)$ and $E_C(k)$ are the in-plane exciton and photon energies, respectively and Ω_R (called Rabi splitting) is the light-matter coupling energy, which is given by [12]:

$$\hbar\Omega_R \approx \hbar\sqrt{\frac{2\Gamma_0 N_{QW}}{n_C L_{eff}}} \tag{1.9}$$

here N_{QW} is the number of QWs, L_{eff} is the length of the cavity plus the penetration depth of the electric field inside the DBR mirrors and Γ_0 is the radiative decay rate of the exciton, which is proportional to the exciton oscillator strength [13]:

$$\Gamma_0 = \frac{\pi}{4\pi\epsilon_0 n_C}\frac{e^2}{m_0 c} f^{osc} \tag{1.10}$$

where is ϵ_0 the vacuum dielectric constant and e is the electron charge.

The Hamiltonian in Eq. 1.8 can be written in the matrix form:

$$H = \begin{pmatrix} E_C\left(k\right) & \hbar\Omega_R \\ \hbar\Omega_R & E_X\left(k\right) \end{pmatrix} \tag{1.11}$$

whose eigenvalues are the E_{LPB} and E_{UPB}, which correspond to the lower and upper polariton branch, respectively:

$$\begin{aligned} E_{LPB} &= \tfrac{1}{2}\left(E_C\left(k\right) + E_X\left(k\right) - \sqrt{4\hbar^2\Omega_R^2 + \left(E_C\left(k\right) - E_X\left(k\right)\right)^2}\right) \\ E_{UPB} &= \tfrac{1}{2}\left(E_C\left(k\right) + E_X\left(k\right) + \sqrt{4\hbar^2\Omega_R^2 + \left(E_C\left(k\right) - E_X\left(k\right)\right)^2}\right) \end{aligned} \tag{1.12}$$

These states have been obtained by diagonalizing the Hamiltonian in Eq. 1.8 introducing the following transformation in terms of the polariton's basis [14]:

$$\begin{pmatrix} p_k \\ q_k \end{pmatrix} = \begin{pmatrix} X_k & C_k \\ -C_k & X_k \end{pmatrix} \begin{pmatrix} b_k \\ a_k \end{pmatrix} \tag{1.13}$$

where p_k and q_k are the operators for the lower and upper polariton, respectively and X_k, C_k are the Hopfield's coefficients, which satisfy the condition $X_k^2 + C_k^2 = 1$. These coefficients represent the excitonic and photonic component of the polaritons respectively.

Figure 1.7 shows the upper and lower polariton branches together with the bare exciton and photon dispersion relations for a cavity exciton energy difference equal to zero ($(E_C - E_X)_{k=0} = 0$). This energy difference is known as a detuning (δ) and determines whether the lower polaritons are excitonic-like ($\delta > 0$) or photonic-like ($\delta < 0$). The quadratic dependence on k of the the exciton is not visible in the figure, due to the fact that the exciton mass (m_X) is much heavier than the photon mass.

If Eq. 1.12 is expanded around $k = 0$, an effective mass for the lower and upper polariton can be defined as follows:

$$\frac{1}{m_{LBP}} = \frac{|C_k|^2}{m_C} + \frac{|X_k|^2}{m_X}$$

$$\frac{1}{m_{UBP}} = \frac{|X_k|^2}{m_C} + \frac{|C_k|^2}{m_X} \tag{1.14}$$

as $m_C \ll m_X$ at $k = 0$, the polariton mass is mainly given by the photon mass weighted by the photonic or excitonic component, this result in a very light effective mass for the polariton of the order of $\sim 10^{-6} m_0$.

So far the finite lifetime of both excitons and photons has not been taken into account, they play an import role in the polariton formation and now we discuss it. Excitons have a decay rate γ_X (considering radiative and non radiative decay), while the decay rate of photons is γ_C. By introducing this decay rates in Eq. 1.12, and for zero cavity exciton detuning, the Rabi splitting can be defined as:

$$\Omega_R^\gamma = \sqrt{4\Omega_R^2 - (\gamma_C - \gamma_X)^2} \tag{1.15}$$

If $\Omega_R < \left(\frac{\gamma_C - \gamma_X}{2}\right)$ is purely imaginary both solutions in Eq. 1.12 have the same energy, under this condition, the system is described by the bare cavity and exciton modes. On the other

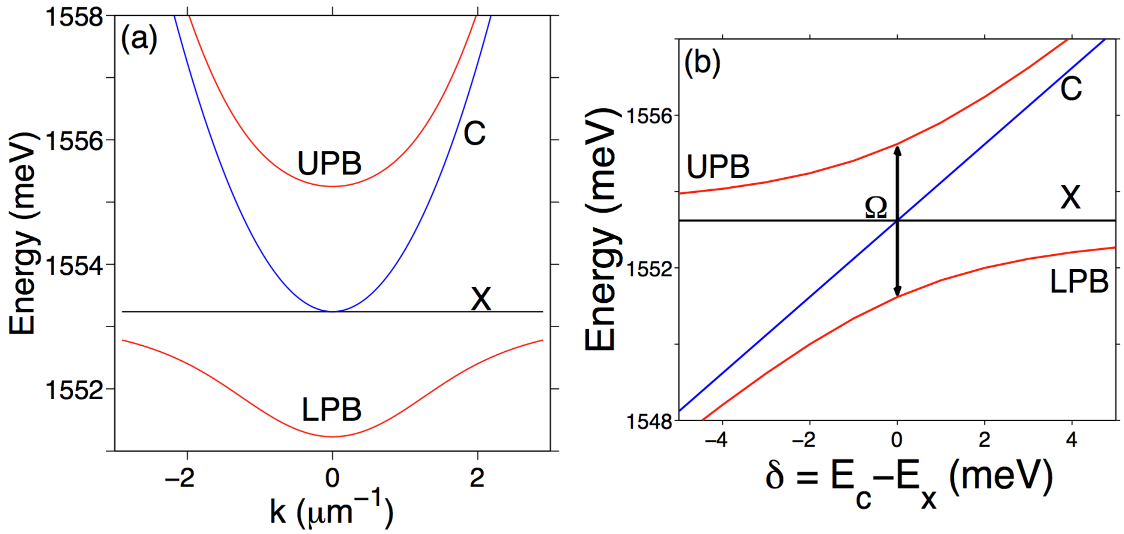

Figure 1.7: Polariton dispersion. (a) Shows the polariton dispersion (in red the upper and lower branches) as a function of the k-vector together with the bare exciton and photon modes, for a $\delta = 0$. (b) Depicts the polariton dispersion at the bottom of the bands as a function of the cavity-exciton detuning.

hand, when $\Omega_R > \left(\frac{\gamma_C - \gamma_X}{2}\right)$ is a real number, Eq. 1.12 shows two solutions, the upper and lower polariton branch. This can be understood as follows: excitons and photons exchange energy, when this exchange occurs several times before the decay rates are significant, the system is in the strong coupling regime and the normal modes are given by Eq. 1.12.

The effect of the exciton splitting depending on their orientation with respect to their wavevector is increased in microcavities due to the exciton-light coupling, since the electromagnetic modes also present a TE-TM splitting. Therefore, one can express the polariton TE-TM splitting as [15]:

$$\Delta_P = \Delta_X \left|X_k\right|^2 + \Delta_C \left|C_k\right|^2 \tag{1.16}$$

where X_k and C_k are the exciton and photon Hopfield coefficients, Δ_X and Δ_C are the TE–TM splitting corresponding to the exciton [9] and cavity modes[5], respectively. Δ_P strongly depends on the detuning between the cavity mode and the exciton resonance as shown in Ref. [16].

1.4 Pseudospin of the exciton-polaritons

The polarization properties of the polaritons are determined by the properties of their constituents. The spin of photons in the circular basis is ±1 , meanwhile optically active excitons (heavy excitons) have spin ±1 (in fact, light excitons with spin ±1 are able to couple light as well, but the likelihood is a third of that for heavy excitons, moreover they lay at higher energies and will not be considered. Also light excitons with spin 0 are able to couple light as long as the light is linearly polarized). As both excitons and photons have integer spin, so the polariton spin is integer as well, this allows to treat them as bosons, in the limit of dilute system where the excitonic component does not show its fermionic nature. Polaritons interact between them, this interaction can be attractive or repulsive, depending on the spin configuration, and it is described in terms of two constant that quantifies the strength of the interaction: α_1 for polaritons with parallel spin and α_2 for polaritons with opposite spin. The factors responsible for attraction are the Van-der-Waals coupling (independent on spin and small), the indirect exchange coupling via the dark states, and interaction via the biexciton state (main factor). The two latter factors contribute only in the parallel polariton's spin configuration (α_1); the mechanisms responsible for the repulsion of the exciton-polaritons are the mean-field electrostatic interaction, which does not depend on spin and direct exchange interaction (only valid for opposite polariton's spin configuration α_2) [17].

A very convenient and useful method to describe the polarization properties of the exciton-polariton is to use the pseudospin representation, due to the fact that the polarization of an emitted photon has a one to one correspondence with the polariton pseudospin.

Light can be fully characterized by the Stokes parameters, which are the degree of polarization in the linear (H,V) diagonal (D, A) and circular (σ^+, σ^-) basis, defined as follows:

$$\rho_L = \frac{I_H - I_V}{I_H + I_V},\ \rho_D = \frac{I_D - I_A}{I_D + I_A},\ \rho_C = \frac{I_{\circlearrowright} - I_{\circlearrowleft}}{I_{\circlearrowright} + I_{\circlearrowleft}} \tag{1.17}$$

by using the Poincare sphere representation; the Stokes vector $\vec{S}$ is a point in the surface of

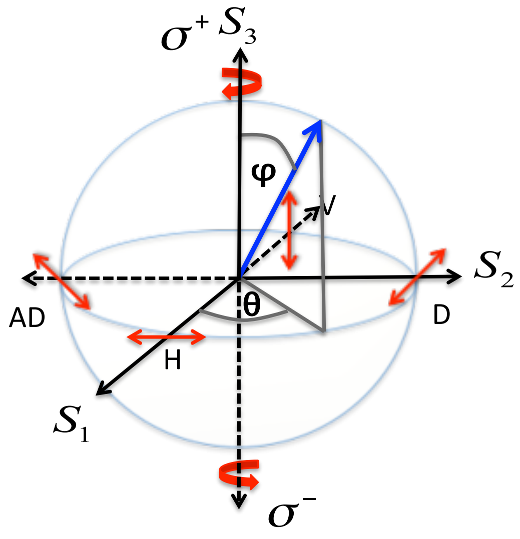

Figure 1.8: Poincare Sphere. Circularly polarized light lays on the poles of the sphere, while linearly polarized light is on its equator.

the sphere, for fully polarized light is defined by:

$$\vec{S} = \sqrt{\rho_L^2 + \rho_D^2 + \rho_C^2} \tag{1.18}$$

where the azimuth and inclination angles are given by:

$$\theta = \arctan \frac{\rho_D}{\rho_L};\ \varphi = \arccos \frac{\rho_C}{\sqrt{\rho_L^2 + \rho_D^2}} \tag{1.19}$$

respectively. Figure 1.8 shows a general state of light with elliptical polarization.

The poles of the sphere represent a purely circularly polarized state of light, and linearly polarized states are represented on the equator of the sphere. Any other polarized state corresponds to the general case of an elliptical polarization.

1.5 Polariton optical parametric oscillator

Polaritons show a strong non linear behavior due to their excitonic component that allows them to interact via Coulomb interaction, this non linear behavior gives rise to parametric scattering processes. When the LPB is quasi resonantly pumped at a certain angle, close to its inflection point, for a given pump power, the polaritons created at this point, the pump state (k_p), interact between them and scatter in pairs, one of them goes to the signal state (k_s) and the other one jumps to the idler state (k_i). In this process the polariton at the idler state gains energy and momentum, while the polariton at the signal state looses the same amount of energy and momentum with respect to the polaritons at the pump state, *i.e* the scattering process [see Fig. 1.9(a)] must fulfill energy and momentum conservation (phase-matching conditions) according to:

$$\begin{gathered} 2\vec{k}_p = \vec{k}_s + \vec{k}_i \\ 2E_p = E_s + E_i \end{gathered} \tag{1.20}$$

where $\vec{k}_p$, $\vec{k}_s$ and $\vec{k}_i$ are the $\vec{k}$ vectors, and E_p, E_s, and E_i are the energies of the pump, signal and idler states, respectively. This process was first reported in microcavities in Ref. [18] in the form of an optical parametric amplifier (OPA), where the parametric scattering was triggered by a probe laser at $k = 0$. The gain of the signal state ($k_s = 0$) was highly increased when the k vector of the pump was close to the inflection point of the LPB [see Fig. 1.9(b)]. This increment of the signal state is due to the bosonic amplification induced by stimulated scattering. Furthermore, the OPA process highly depends on the polarization of the pump and probe beam [18-20], showing the rich phenomenology of the scattering process.

When the parametric scattering is achieved with only a pump beam [21-23], the process is dubbed optical parametrical oscillator (OPO) and is characterized by the macroscopy occupation of the three states. The OPO behavior is possible in microcavities, due to a) the excitonic component which gives them a strong non linear behavior and b) the very peculiar shape of the lower polariton branch (s shape), that allows to easily fulfill the phase-matching conditions.

In the parametric scattering process, the phase of the pump state (ϕ_p) is imposed by

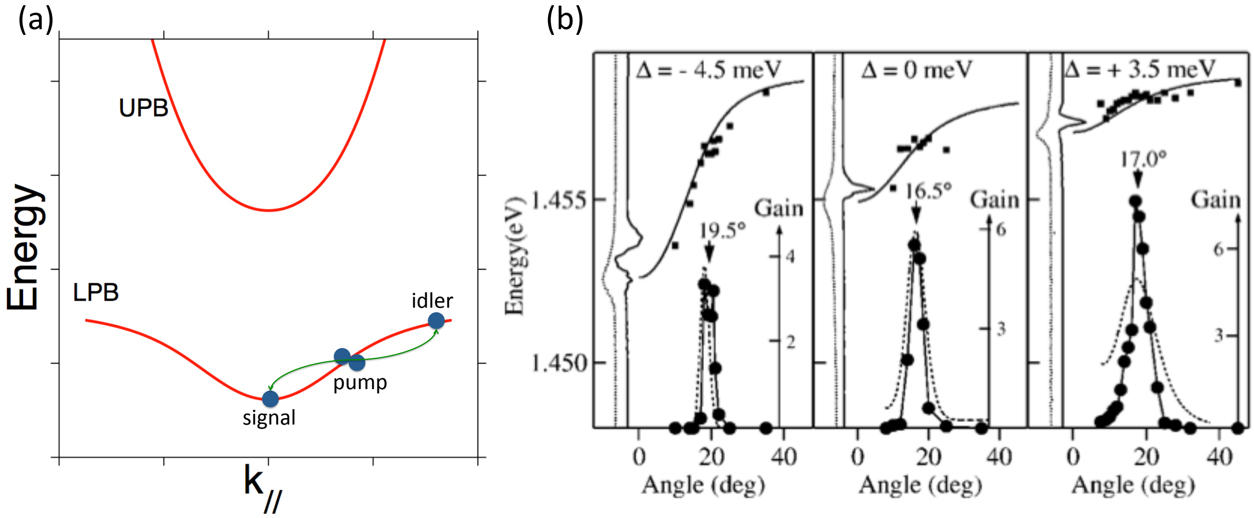

Figure 1.9: OPO scheme. (a) shows a scheme of the OPO process, where the pump creates polaritons with a certain momentum and energy and the scattering process allows them to jump towards the signal and idler states. (b) shows the gain achieved by the signal state when the phase-matching condition are satisfied, for three different detunings (adapted from [18])

the pump laser. On the other hand, the phase of the signal and idler states is free, since it remains invariant under simultaneous phase rotation of both signal and idler. The phase of the full process is given by [24]

$$2\phi_p = \phi_s + \phi_i \tag{1.21}$$

In the OPO configuration, the phase of the signal and idler states, is spontaneously chosen, but the Eq. 1.21 is still valid. This fact, which is important because it breaks the symmetry of the system will be addressed later on in § 1.6.4

The coherence of the signal state was investigated in an OPA configuration by coherent control in Ref. [25]. In that work, a 1 *ps* pulse was applied at non-zero incidence angle to create a pump population; then two phase locked probe pulses were sequentially applied to

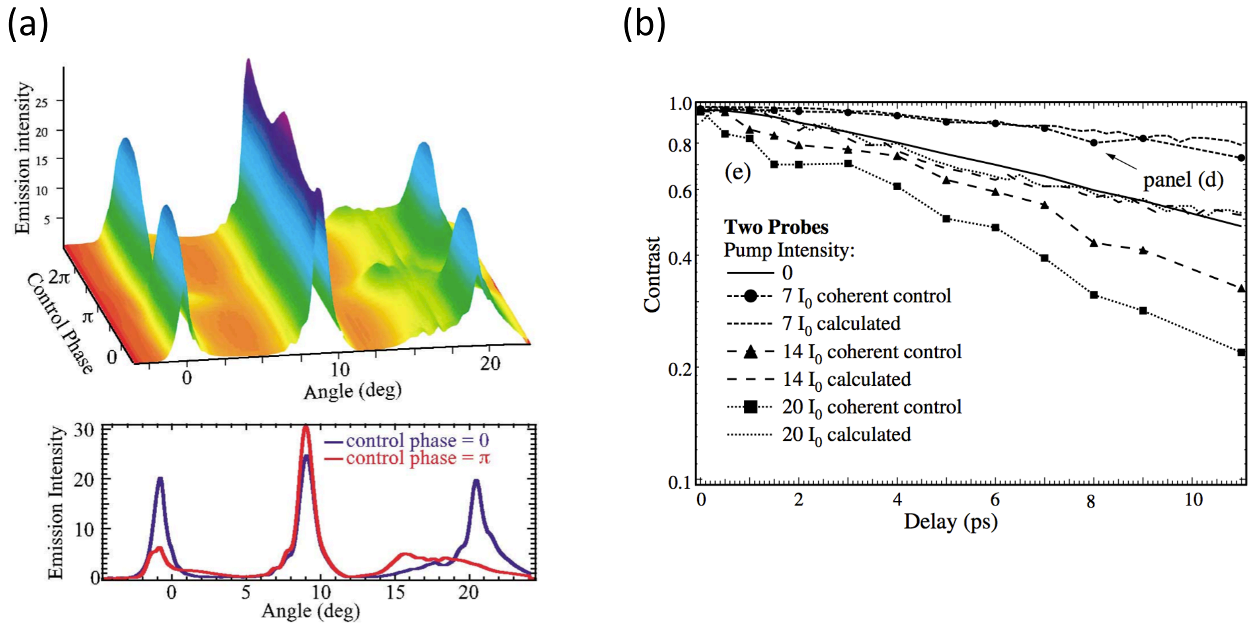

Figure 1.10: Coherence of the signal state by means of coherent control. (a) Angular pattern of the emission in transmission geometry as a function of the control phase (time delay 2 ps). The lower panel shows plots for constructive and destructive control phase. (b) Contrast of coherent control oscillations versus the delay between the two probe pulses; the first probe pulse is synchronous with the pump. I_0 is the threshold intensity of the first probe which triggers stimulated scattering (adapted from [25]).

the sample at normal incidence. The first probe pulses above certain threshold, P_0, triggered stimulated scattering of the pump polaritons towards the $k = 0$ state. Then, the second probe pulse fed polaritons that would interfere with the existing population at $k = 0$. The results demonstrated [see Fig. 1.10] high coherence of polaritons at $k = 0$, and very long coherence times of the order of 10 ps [see Fig. 1.10].

One can describe the OPO process by either using the Gross-Pitaevskii equation or a semi-classical Boltzmann model (both are used by the group of G. Malpuech to model the results shown in Chapter 4). Here we introduce them, we start with the Gross-Pitaevskii equation, which is basically a non linear Schrodinger equation that includes interactions, it reads:

$$i\hbar\frac{\partial}{\partial_t}\begin{pmatrix}\psi\\ \varphi\end{pmatrix}=\left[\begin{pmatrix}\frac{\nabla^2}{2m_C}-i\Gamma & \frac{\Omega_R}{2}\\ \frac{\Omega_R}{2} & \frac{\nabla^2}{2m_X}\end{pmatrix}+\begin{pmatrix}V_C\left(r\right) & 0\\ 0 & g_X\left|\varphi\right|^2\end{pmatrix}\right]\begin{pmatrix}\psi\\ \varphi\end{pmatrix}+\begin{pmatrix}P\\ 0\end{pmatrix} \tag{1.22}$$

where the polariton wavefunction is written in terms of its photonic ψ and excitonic φ components, respectively, Γ is the decay rate of the photon, Ω_R is the Rabi splitting, $V_C\left(r\right)$ is a potential affecting the photons, g_X accounts for the particle-particle interactions and P in the pump term acting only on the photonic component.

In the semi-classical Bolztmann model, the population of the three states involved in the OPO process are considered, thus the model is:

$$\frac{dn_k}{dt}=-n_k\Gamma+W_{k\to k'}n_k+P_k \tag{1.23}$$

where the n_k for $k=s,i,p$ are the population for the signal, idler and pump states respectively, Γ is the decay rate and W describes the polaritons scattering rate from one state to another, P_k is the pump term and it is different from zero only for $k=p$.

1.6 Condensation

In 1925 Einstein proposed a new state of the matter where a system composed by identical particles, below certain temperature, can occupy a single energy state [26], called Bose Einstein condensate (BEC). Many years passed until this proposal was used to describe an actual system, when London explained the superfluidity behavior of liquid Helium [27]. Great theoretical efforts were done between the 40's and 60's in order to give a more general description of the BEC phase [28-30].

An experimental realization of a BEC was done in 1995 in a dilute atomic ^{85}Rb gas [31], this achievement brought a huge interest into the field.

Microcavity exciton-polaritons represent a solid state system where massive occupation of a single state also occurs [32].

1.6.1 Ideal Bose gas

Now we present the derivation of the BEC transition for an ideal Bose gas (non interacting) that follows the approach found in [4, 33, 34]. In a grand canonical ensemble, at thermal equilibrium, the probability of a configuration with N_r particles and energy E_s is given by:

$$P_{r,s} = \frac{e^{\beta(\mu N_r - E_s)}}{Z(\beta,\mu)} \tag{1.24}$$

where $\beta = 1/k_BT$, k_B is the Boltzmann constant, T the temperature of the reservoir, μ is the chemical potential that represents the needed energy to add a particle to the system and $Z(\beta,\mu)$ is the grand partition function:

$$Z(\beta,\mu) = \sum_{N_r}^{\infty}\sum_{S} e^{\beta(\mu N_r - E_s)} \tag{1.25}$$

Applied to an ideal gas of indistinguishable particles distributed in 'microstates i' of energy ϵ_i and occupation number N_i in each state:

$$Z(\beta,\mu) = \sum_{N_i} e^{\beta(\mu\sum_i N_i - \sum_i \epsilon_i N_i)} = \prod_i \sum_{N_i} e^{\beta(\mu-\epsilon_i)N_i} \tag{1.26}$$

for a Bose gas the sum is extended to $N_i = 0, 1, 2, ...,$

$$Z(\beta,\mu) = \prod_i \left(1 - e^{\beta(\mu-\epsilon_i)}\right) \tag{1.27}$$

Using Eq. 1.27 one can obtain the Bose-Einstein distribution function $f_{BE}(\epsilon_i)$, the total number of particles N, and the total internal energy of the gas $E(T,\mu)$:

$$f_{BE}(\epsilon_i) = n_i = -\frac{\partial}{\partial \beta \epsilon_i} \ln Z = \frac{1}{e^{\beta(\epsilon_i - \mu)} - 1} \tag{1.28}$$

$$N = \frac{\partial}{\partial \mu} \beta \ln Z = \sum_i \frac{1}{e^{\beta(\epsilon_i - \mu)} - 1} = \sum_i f_{BE}\left(\epsilon_i\right) \tag{1.29}$$

$$E\left(T, \mu\right) = \sum_i \epsilon_i f_{BE}(\epsilon_i) = \frac{\epsilon_i}{e^{\beta(\epsilon_i - \mu)} - 1} \tag{1.30}$$

Due to the fact that $n_i \geq 0$ the constraint for a Bose gas $\mu < \epsilon_0$ is imposed (ϵ_0 is the energy of the ground state). Hence, at given T, $f_{BE}(\epsilon_i > \epsilon_0)$ reaches a finite maxima, while $f_{BE}(\epsilon_0)$ diverges. So Eq. 1.29 can be rewritten in terms of the particle number in the ground state, N_0, and N_T the particles in any excited state:

$$N = N_0 + N_T = \frac{1}{e^{\beta(\epsilon_0 - \mu)} - 1} + \sum_{i \neq 0} f_{BE}\left(\epsilon_i\right) \tag{1.31}$$

for $\mu \to \epsilon_0$ from below, N_0 takes values increasily large, this means that the ground state becomes massively occupied, on the other hand, N_T takes a maximum value (N_C) for $\mu = \epsilon_0$, thus if $N > N_C$, the exceeding particles must go to the lower state in order to satisfy Eq. 1.31. The massive occupation of a ground state and the "depletion" of any excited state is the mechanism that gives rise to the Bose-Einstein condensation.

Considering a three dimensional gas where the particles are able to move free in the volume, *i.e.* the particles have a parabolic dispersion, $E = P^2/2m$, the density of particles in an excited state can be written as

$$\frac{N_C}{V} = \left(\frac{m k_B T}{2\pi\hbar^2}\right)^{3/2} \int\limits_0^\infty \frac{\sqrt{\epsilon}}{e^{\epsilon/k_B T} - 1} d\epsilon = \frac{2.612}{\lambda_{dB}^3} \tag{1.32}$$

the term $\sqrt{\frac{2\pi\hbar^2}{m k_B T}}$ is the de Broglie wavelength (λ_{dB}). When the separation between particles is of the order or smaller than λ_{dB}, the individual wavefunctions start to overlap and all the particles are in the same state.

Condensation can be achieved by either increasing the number of particles above N_c, keeping the temperature constant, or by decreasing the temperature while keeping the number of particles fixed.

1.6.2 Weakly interacting Bose gas

In the previous section a description of the ideal Bose gas, where the particle-particle interactions are not considered, was introduced giving the main mechanism that allows Bose-Einstein condensation. Here a Bose gas with interaction between particles is presented.

The Hamiltonian describing a dilute interacting Bose gas is given by [35]:

$$H = \sum_p \frac{p^2}{2m} a_p^\dagger a_p + \frac{U_0}{2V} \sum_{p,p',q} a_{p+q}^\dagger a_{p'-q}^\dagger a_p a_{p'} \tag{1.33}$$

where a_p $\left(a_p^\dagger\right)$ is the annihilation (creation) operator, V is the volume of the system and U_0 is an approximation to the microscopic two body potential.

In the Bogoliubov approximation [36], at $T = 0$ the assumption that only small deviations are possible is made, therefore all terms with higher order than 2 in a_p and $a_p^\dagger$ will be neglected. Let N_0 denote the occupation number of the ground state, thus the zero-momentum operators a_0 and $a_0^\dagger$ can be replaced by $\sqrt{N_0}$.

The energy of the ground state is given by taking into account the states at $p = 0$:

$$E_0 = N^2 \frac{U_0}{V} \tag{1.34}$$

and the chemical potential is given by:

$$\mu = \frac{\partial}{\partial N} E_0 = U_0 \frac{N}{V} \tag{1.35}$$

The total number of particles is $N = a_0^\dagger a_0 + \sum_{p \neq 0} a_p^\dagger a_p$, then the Eq. 1.33 reads:

$$H = N^2\frac{U_0}{V} + \sum_{p\neq 0}\left[\left(\frac{p^2}{2m}+\mu\right)a_p^\dagger a_p + \frac{\mu}{2}\left(a_p^\dagger a_{-p}^\dagger + a_p a_{-p}\right)\right] \tag{1.36}$$

the above Hamiltonian can be diagonalized by introducing the following coefficients:

$$\begin{aligned} a_p &= u_p b_p + v_{-p}^* b_{-p}^\dagger \\ a_p^\dagger &= u_p^* b_p^\dagger + v_{-p} b_{-p} \end{aligned} \tag{1.37}$$

where u_p and v_{-p} are given by:

$$u_p, v_{-p} = \pm\sqrt{\frac{p^2/2m+\mu}{2\epsilon(p)} \pm \frac{1}{2}} \tag{1.38}$$

where $\epsilon(p)$ is the Bogoliubov spectrum, defined by:

$$\epsilon(p) = \sqrt{\frac{p^2}{2m}\left(2\mu + \frac{p^2}{2m}\right)} \tag{1.39}$$

then, the Eq. 1.33 is diagonalized in the form $H = E_0 + \sum_p \epsilon(p)\, b_p^\dagger b_p$.

1.6.3 Long range order

In § 1.6.1 the description of a BEC transition was presented, here we introduce a more suitable definition of a transition, where massive occupation of a single state occurs. In this transition the different particle wavefunctions forming the system collapse into a macroscopic wavefunction in the ground state that describes the system, this is given by:

$$\Phi = \sqrt{N_0}\phi(r) \tag{1.40}$$

where N_0 is the number of particles in the ground state and $\phi(r)$ is the phase. This has a non zero mean value, and it is defined as the order parameter of the transition. At the transition, the phase in Eq. 1.40 represents the phase of the whole condensate and it is spontaneous fixed, therefore the "rotational" symmetry is broken, and the system becomes phase coherent [30, 37].

Another way to state condensation is through the single particle density matrix (dubbed as well as correlation function), defined as:

$$\rho\left(r, r'\right) \equiv \left\langle \psi^{\dagger}\left(r\right) \psi\left(r'\right)\right\rangle \tag{1.41}$$

where ψ $\left(\psi^{\dagger}\right)$ is the particle annihilation (creation) operator. The diagonal elements in the density matrix ($\rho(r, r)$) represent the number of particles at the position r.

The density matrix also determines the momentum distribution $\rho\left(p\right) = \left\langle \psi^{\dagger}\left(p\right) \psi\left(p\right)\right\rangle$, where $\psi\left(p\right) = \left(2\pi\hbar\right)^{-3/2} \int dr \exp\left(ip \cdot r/\hbar\right) \psi\left(r\right)$ is the annihilation operator in momentum space.

In a homogeneous system consisting of N particles occupying a volume V, in the thermodynamics limit, the single particle density matrix depends on the relative distance $r - r'$, therefore one can write

$$\rho\left(r - r'\right) = \frac{1}{V} \int dp \rho\left(p\right) e^{\left(ip \cdot \left(r - r'\right)/\hbar\right)} \tag{1.42}$$

In a non interacting Bose gas the ground state ($p = 0$) is macroscopically occupied and the momentum distribution can be written as:

$$\rho\left(p\right) = N_0 \delta\left(p\right) + \rho_{exc}\left(p\right) \tag{1.43}$$

here N_0 is proportional to the total number of particles δ is the Dirac delta function and $\rho_{exc}\left(p\right)$ is a smooth function. For $r - r' \to \infty$ Eq. 1.42 has a finite non zero value given by:

$$\rho\left(r - r'\right)_{r - r' \to \infty} \to \frac{N_0}{V} \tag{1.44}$$

this behavior is referred as off-diagonal long-range order (ODLRO) since involves the components out of the diagonal in the single particle density matrix and was proposed in Ref. [28] as a general definition of a BEC.

Normalizing the single particle density matrix by the total number of particle at the positions r and r', one obtains

$$g^{(1)}\left(r,r'\right)=\frac{\left\langle\psi^{\dagger}\left(r\right)\psi\left(r'\right)\right\rangle}{\sqrt{\left\langle\psi^{\dagger}\left(r\right)\psi\left(r\right)\right\rangle\left\langle\psi^{\dagger}\left(r'\right)\psi\left(r'\right)\right\rangle}}\tag{1.45}$$

This can be expressed in terms of the electromagnetic field, giving the first order correlation function

$$g^{(1)}\left(r,t:r',t'\right)=\frac{\left\langle E^{-}\left(r,t\right)E^{+}\left(r',t'\right)\right\rangle}{\sqrt{\left\langle E^{-}\left(r,t\right)E^{+}\left(r,t\right)\right\rangle\left\langle E^{-}\left(r',t'\right)E^{+}\left(r',t'\right)\right\rangle}}\tag{1.46}$$

with $E(r,t)=\int_{-\infty}^{\infty}\zeta(\omega,r)e^{-i\omega t}d\omega=E^{-}+E^{+}$, where E^{-} is the equivalent to the creation operator and corresponds to the negative frequencies of the electric field and E^{+} corresponds to the annihilation operator and represents the positive frequencies of the electric field [38].

1.6.4 Condensation of polaritons

Exciton-polaritons were proposed to show condensation (massive occupation of a single state) and lasing by bosonic amplification in Ref. [39], the exciton-polariton laser was demonstrated by optically exciting a microcavity in Ref. [40], and more recently, by means of electrically injection of polaritons [41]. Condensation was first claimed in Ref. [42], where the second order correlation function showed the feature of a coherent state above certain pump power, however the lack of proof about whether the system was in the strong coupling regime or not raised doubt about their assertion.

The firm demonstration of polariton BEC was achieved in Ref. [32], in that work most of the footprints shown by a BEC were measured: narrowing in momentum space [see Fig. 1.11(a)], the appearance of off-diagonal long-range order [shown in Fig. 1.11(b)], build-

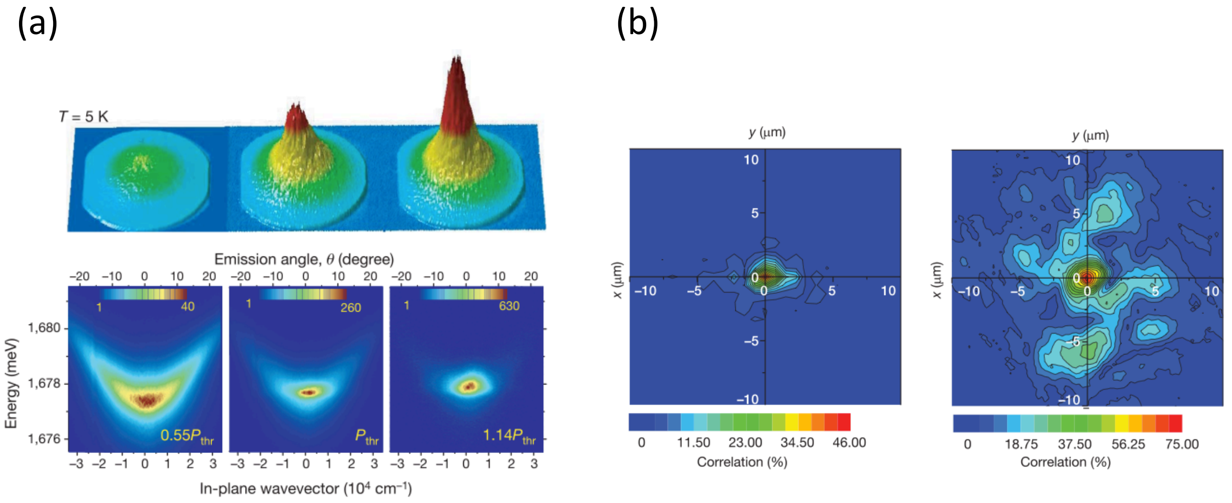

Figure 1.11: Polariton BEC. (a) Narrowing of the emission in momentum space. (b) Correlation maps below/above (left/right panel) condensation threshold (adapted from [32]).

up of linear polarization, and the massive occupation of a state when the energy of the condensate is close the the chemical potential. Since then, there have been further reports of polariton BEC [43, 44]. More intriguing behavior associated to the BEC phase transition have been reported: the observation of quantized vortices and half vortices [45, 46] and the appearance of an antivortex after printing a vortex in the condensate [47]; superfluidity has been demonstrated in Ref. [48, 49] by the diffusionless flow of a polariton condensate against a defect and permanent flow, where polaritons rotate much longer than the duration of an initial impulse [50]. Solitonics features of the polariton BEC have been reported in Ref. [51] for dark solitons, and bright solitons in Ref. [52].

When the microcavity is pumped in OPO regime, *i.e.* there are three state macroscopically occupied, the solutions of Eq. 1.22 are three (pump, signal and idler) states [53]. Such solutions are in principle invariant under simultaneous rotation of the phase of both signal and idler states, nevertheless the signal and idler spontaneously select their phase in the OPO regime, therefore the phase rotation is spontaneously broken. This symmetry breaking implies the appearance of Goldstone modes ($\omega_G(k) = c_G k$) that go to zero around the signal state in the long-wavelength limit. The intensive study done in Ref. [53] shows that in the case of non equilibrium system, there is no singularity in $\omega_G(k)$ in the vicinity of the signal state (the equilibrium case shows a discontinuity in $k = 0$) [54]. A Goldstone mode can be understood as a spatially slowly varying twist of the signal and idler phases. A localized perturbation will not propagate as a sound wave, but rather relax back to the equilibrium state while being dragged by the pump polariton flow: this over-damped and diffusive character is a remarkable difference with respect to the equilibrium case. In the case of non-resonant excitation of the polariton condensate the Goldstone mode has been predicted to be diffusive [55]

Moreover, the emission from the signal state has the following characteristics: narrowing in momentum space [21], threshold-like behavior as the pump intensity is increased [23, 56], coherence times lasting longer than the polariton lifetime (which have been measured by means of coherent control [25] and also through the first order correlation function [57]), and spontaneous spatial coherence has been predicted to appear [58].

Despite all these properties, that are attributed to the BEC phase transition, the OPO polariton condensate cannot be considered as a genuine, "classical" BEC, since the system is in a dynamic equilibrium between three states macroscopically occupied and therefore thermalization is never reached.

Chapter 2

Sample and experimental techniques

This section is devoted to give a discussion of the sample and the experimental techniques used in this thesis. After the description of the sample, we start giving the specifications of the excitation source, then the imaging techniques are described for both, the real and momentum space, later the interferometer techniques are introduced and finally the polarization resolved setup is described.

2.1 Sample

The sample used in this work is provided by the group of professor Jϕrn M. Hvam at the Danmarks Tekniske Universitet (DTU). It is a $GaAs$ based microcavity, grown by molecular beam epitaxy. The sample consists of a single 10 nm $GaAs/Al_{0.3}Ga_{0.7}As$ quantum well (QW) placed at the antinode of the electromagnetic field of a λ cavity. The bottom (top) Bragg reflector is composed by 25 (16) pairs of $AlAs/Al_{0.15}Ga_{0.85}As$. A schematic draw of the microcavity is shown in Fig. 2.1(a). From the measured polariton emission a cavity linewidth of 0.13 meV and an excitonic linewidth of $\sim$0.06 meV were inferred, the cavity lifetime is of order of 2 ps and the Rabi splitting is about 4.2 meV [59]. The cavity presents a wedge across the sample that enables the tuning of the cavity-mode energy by changing the position of the excitation spot on the sample. Figure 2.1(b) shows the measured polariton half width at half maximum (HWHM) as a function of the detuning (adapted from [60]). The heavy-

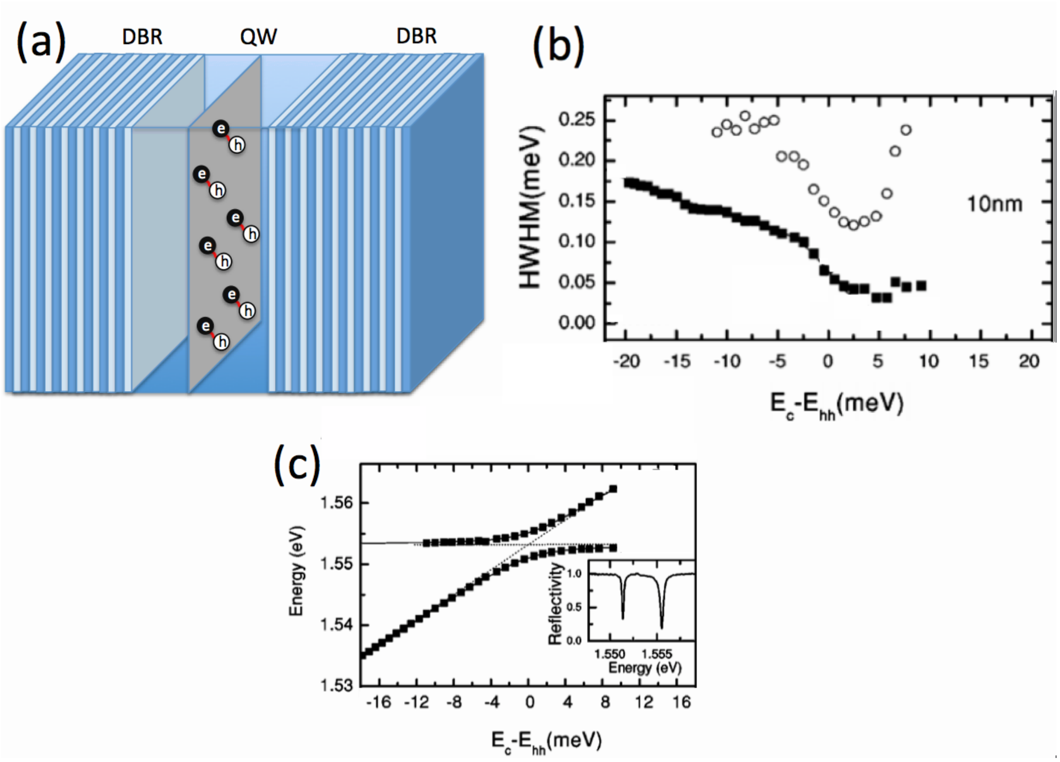

Figure 2.1: Scheme of a microcavity. (a) Represents the microcavity structure composed by two DBR and a spacer with a quantum well embedded at the antinode of the electromagnetic field. (b) Linewidth vs detuning of the lower (closed squares) and upper (open circles) polariton branches (adapted from Ref. [60]) (c) Polariton energies as a function of the detuning. The inset shows the reflectivity spectrum of the microcavity at zero detuning (adapted from Ref. [60]).

hole exciton resonance is at 1553.24 meV (798.24 nm), the light-hole exciton resonance is at 1565.5 meV (791.97 nm) far detuned from the heavy-hole resonance (not shown), therefore the sample acts as having a single resonance over the detuning range.

The polariton energies as a function of the detuning are depicted in Fig. 2.1(c).

2.2 Excitation source

A key issue in this thesis, and in any high resolution spectroscopy experiment, is the use of a frequency locked laser, which allows to study the otherwise masked properties of the studied system due to the intrinsic laser fluctuations in power and frequency. The laser is a $Ti : Al_2O_3$ (Ti:Sa) crystal in a ring cavity geometry (Sirah Lasertechnik model Matisse TX/light), pumped by a CW laser (Spectra Physics Millenia Pro 10S, whose laser medium is a $Nd : YVO_4$ crystal, doubled in frequency by a LBO crystal), which is pumped by diode bars. This laser has a linewidth as narrow as 75 kHz (manufacture specifications). In order to achieve this narrow emission, several frequency filters are used: first the cavity configuration in a ring geometry, where the length of the cavity is changed by the tuning mirror [see Fig. 2.2(a)], allows to have oscillation in two distinct counter-propagating direction, (rather than the standing wave in linear cavities, with the possibility to get a different mode oscillating with its anti-node where the lasing mode has its nodes). The existence of two traveling waves, back and forth, with the same frequency could lead to a complicated intensity dynamics, so as to get rid off this problem an optical diode is placed in the path letting just one direction oscillate. Due to this, a single longitudinal mode is easier to reach, besides a homogeneous saturation of the laser medium allows to use most of the atoms for amplification, hence a higher power is achieved, which at the working wavelength 800 nm, is about 2 W.

To reduce the available lasing modes in the cavity, coated cavity mirrors that are highly reflective only for a certain range of wavelengths are used, decreasing the broad emission from the Ti:Sa crystal, in this case the coating is made for the range 750- 880 nm.

Within this range, a coarse frequency selection is done by a birefringence filter (BiFi), which is compose by three quartz plates, with its axes aligned and oriented at the Brewster angle with respect to the incident light. The working principle is based on birefringent properties of the quartz plates, which are acting as a retardation plate and thus rotate the polarization of the incoming beam. On the other hand, the BiFi works as a polarization filter, due to the fact that the incoming p-polarized light does not reflect at the Brewster's angle whereas the s-polarized light will encounter high losses due to reflection. The desire wavelength is achieved by rotating the axes of the plates with respect to the normal surface to the plates, in this way, the optical axis of the quartz crystal will also be rotated, hence yielding new wavelengths of the incoming light for which there is no change of the polarization state, and therefore no losses through reflection at Brewster's incidence.

The single mode operation is achieved by placing etalons in the cavity, one of them is a quartz etalon of 400 μm thickness with a free spectral range of 250 GHz. The principle here is try to make one of the etalon modes to coincide with one of the laser cavity modes; this is done by tilting the etalon. The other etalon is a formed by two Littrow prisms functioning as a Fabry-Perot cavity with an air gap adjustable by a piezo element in one of the prisms: the free spectral range is in this case about 20 GHz. The piezo etalon ensures that all except one longitudinal mode have so high losses that lasing is not possible. Therefore, the spacing of the etalon must be matched to an multiple of the favored longitudinal mode's wavelength. Because of the tight spacing and in order to be able to perform a scan, the spacing is actively controlled. The control loop is based on a lock-in technique and the etalon spacing is varied by a piezo drive.

With the elements described in the previous paragraph the laser linewidth is in the order of MHz, further narrowing in the laser linewidth needs to suppress the laser intrinsic frequency noise, this is obtained by using an external frequency reference, a Fabry-Perot cavity (FP), and locking the laser frequency to this reference.

The technique used to lock the laser frequency is called Pound-Drever-Hall [61] and consists on generating an error function derived from the resonance's maximum, that controls a piezo driver set in one of cavity's mirror and therefore the frequency of the laser. In this method, a small part of the light is separated from the main laser and modulated in frequency by an electro-optic modulator, this adds sidebands to the laser beam, then this is sent to a FP. Since sidebands are out of resonance, they are reflected by the FP, while the laser beam is in resonance. Nevertheless a small part of the laser can escape the FP, carrying phase information about the cavity. This is sent to a photodetector. The output of the photodetector varies as follows: when the frequency is above the resonance, increasing the laser's frequency increases the signal in the photodetector, on the other hand if the frequency is below the resonance, increasing the laser's frequency decreases the signal in the photodetector, thus the frequency modulated light gives information about the actual position of the frequency about the resonance. Then the photodetector's signal is mixed with the modulation signal, extracting the part that is at the same frequency as the modulation signal (the mixer's output

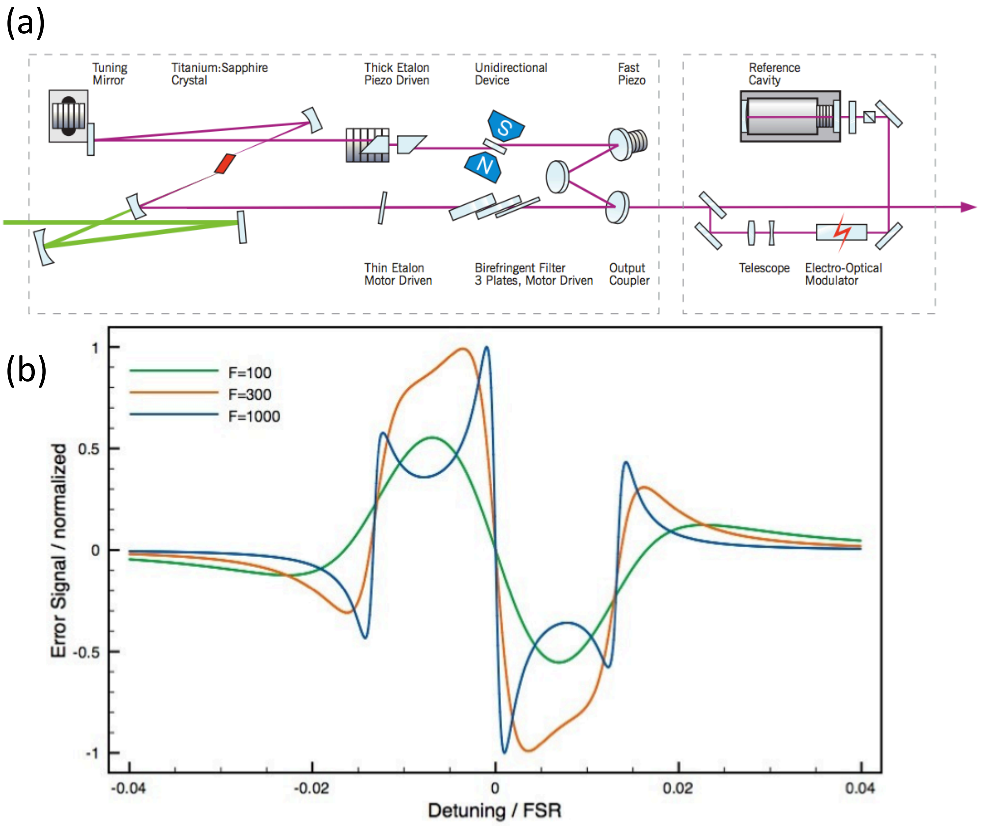

Figure 2.2: Scheme of the laser. (a) A schematic draw of the laser with the reference cavity the more important elements are indicated. (b) The error signal generated with the PDH method for three different values of the cavity's finesse.

is just the product of its inputs). The sign of the mixer's output is different on either side of resonance, and it is zero when the system is exactly on resonance. This is error signal that feeds the fast piezo [see Fig. 2.2(a)] and locks the laser's frequency to the cavity's resonance.

Figure 2.2(a) shows a scheme of the laser and the cavity reference. Figure. 2.2(b) depicts the Pound-Drever-Hall error signal for three different values of the cavity's finesse.

2.3 Imaging techniques

Condensation of polaritons takes place due to the peculiar shape of the polariton's dispersion, which allows the polaritons to massively occupy the bottom of the dispersion [4], therefore in order to fully characterize their emission, it is required to image both real and momentum space.

The microcavity sample is excited through an objective lens with a N.A. ~ 0.75 and a focal length f_0 of $\sim$20 mm, which allows to collect a cone of light of about $\sim 70^{\text{o}}$, however the total N.A. is limited by the imaging optics in our experimental setup, therefore the range of collected angles is about $\sim 40^{\text{o}}$.

In § 3.1.2 the size of the excitation spot is changed to observe how the coherence properties of the condensate are affected. In order to do so, a suitable pair of lenses is added to the optical path of the excitation beam before the excitation lens. The spot size on the sample's surface, for a Gaussian beam, can be estimated using the following formula [62] $S_f = 1.2 \times \lambda \frac{f_0}{S_i}$, where S_f is the spot size on the sample, λ is the wavelength, f_0 is the focal length of the excitation lens and S_i is the spot size before the excitation lens. Thus the spot size on the sample's surface is given by the magnification of the pair of lenses and the focal length of the excitation lens.

The photoluminescence is collected through the same excitation lens, so as to image the real space, the emission is focalized by a lens of 1000 mm focal length, on the entrance slit of a spectrometer/CCD (*Acton SpectraPro 2500i* with a 1200 grooves/mm diffraction grating/*Acton Pixis 1024* with 1024x1024 pixels and the pixel size is 13 μm), where the grating is set at zeroth order in order to have energy integrated images. The magnification of the system is given by the ratio between the imaging lens and the collection lens which, in this case is M $\approx$ 50x. The principle of real space imaging is shown in Fig. 2.3(a), moreover the setup is built in such way that allows to perform filtering in real space by placing a pinhole or a slit in order to investigate a small region of the microcavity structure. Figure 2.3(b) shows a typical real space emission for a pump power below threshold and non-resonant pumping in a region of the microcavity sample without defects.

In order to obtain the emission in momentum space, the angular distribution of the emitted light must be imaged, this can be obtained in the back focal plane of the excitation

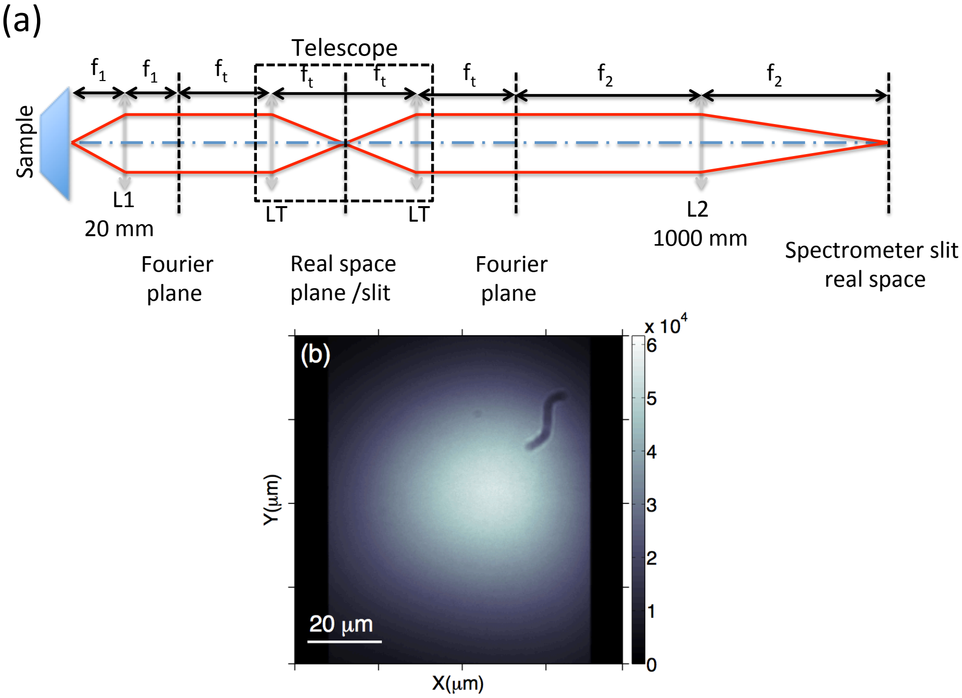

Figure 2.3: Principle of real space imaging. (a) Schematic draw of the lenses and its position, also shown the principle of real space filtering, where two lenses of the same focal length (LT), forming a telescope, create an intermediate real space image where a slit or pinhole filters out the undesired emission. (b) is the real space image below threshold for non-resonant pumping of the microcavity sample.

lens, L1, which corresponds to the Fourier plane. This plane is also found after the telescope [see Fig. 2.3(a)]. The lens L2 is placed at a distance equal to its focal length, f_2, from the Fourier plane. Therefore an image of the momentum space is obtained by placing an additional lens, L3, [see Fig. 2.4(a)] which is focused on the entrance slit of the spectrometer. The positioning of the three lenses is shown in Fig. 2.4(a) (for the sake of simplicity the telescope is not shown): here light emitted with the same angle (red lines) reach the same point in the Fourier plane, with a displacement, Δx, with respect to the optical axis given by $\tan\theta = {}^{\Delta x}/_{f_1}$. Photons emitted by the cavity have the same momentum than the polaritons inside the microcavity, so, the momentum of the polaritons is determined by $k_{\|} = k_0 \sin(\theta)$.

Spectral resolution is achieved by partially closing the entrance slit of the spectrometer

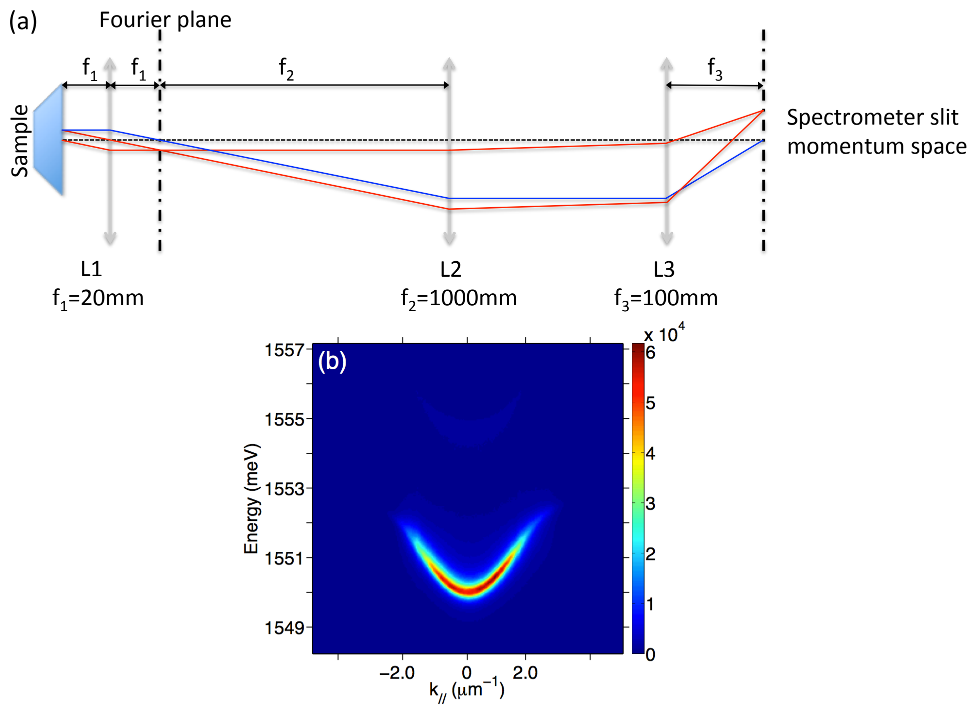

Figure 2.4: Principle of momentum space imaging. (a) Schematic draw of the principle and the lenses positions (red lines represent light emitted with a certain angle, while the blue line displays light emitted at 0º). (b) Polariton's dispersion achieved by spectrally resolving the full momentum space emission.

(40 μm opened), in that way the image on the CCD becomes a one dimensional image in the vertical direction. By setting the diffraction grating at its first order, the horizontal direction becomes energy resolved: the spectral resolution of our spectrometer is of the order of $\sim$100 μeV.

Figure 2.4(b) shows a spectrally resolved momentum space image, *i.e.* the polariton's dispersion, of the same region of the sample shown in Fig. 2.3(b).

2.4 Interferometric setup

In this thesis two interferometric setups have been built and used, depending on whether the coherence properties have to be studied or the phase of the condensate is needed. The former requirements are achieved by using a Michelson interferometric setup and the later is fulfilled with a Mach-Zehnder interferometer.

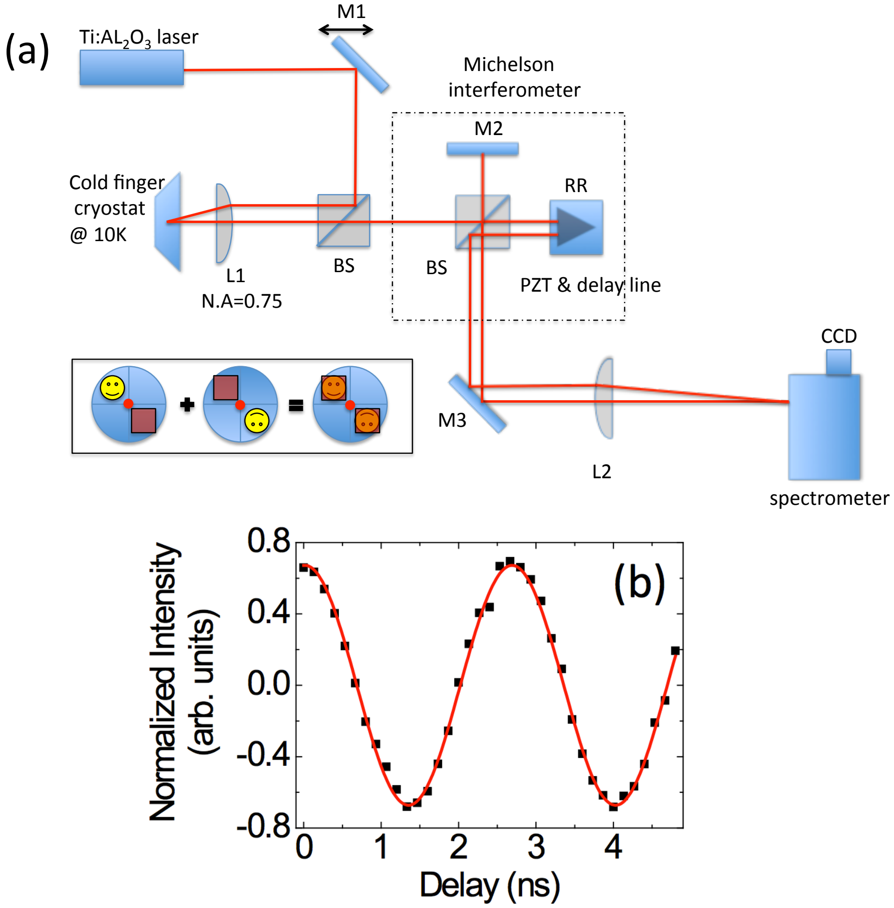

Figure 2.5: Michelson interferometer setup and its working principle. (a) M1, M2 and M3 are mirrors. M_1 is mounted in a linear translation stage to change the k vector. BS are 50/50 beam splitters, L1 is an objective lens with an NA = 0.75, L2 is the real space imaging lens, RR is a retroreflector mounted in a computer controller piezo-element and also mounted in a delay line. The dashed square represents a shield to protect the interferometer from air currents. A scheme of the image and the retroreflected image is shown in the rectangle. (b) A sinusoidal fit to experimental data obtained by scanning the relative length of on arm of the interferometer, the amplitude of this fit gives the $g^{(1)}$.

The interference formed by two fields $\psi_1 = A_1(r)e^{i(\varphi_1(r))}$ and $\psi_2 = A_2(r)e^{i(\varphi_2(r))}$ is given by:

$$\begin{aligned} I &= \left\langle |\psi_1 + \psi_2|^2 \right\rangle \\ &= \left\langle |\psi_1|^2 + |\psi_2|^2 + \psi_1^* \cdot \psi_2 + \psi_2^* \cdot \psi_1 \right\rangle \\ &= \left\langle |A_1|^2 \right\rangle + \left\langle |A_2|^2 \right\rangle + \left\langle A_1^* A_2 e^{i(\varphi_2 - \varphi_1)} \right\rangle + \left\langle A_2^* A_1 e^{-i(\varphi_2 - \varphi_1)} \right\rangle \end{aligned} \tag{2.1}$$

where $A(\vec{r})$ is the amplitude at $\vec{r}$, and $\varphi(\vec{r})$ is the phase of the field. The last term in the above equation can be re-arrenged considering that $\langle \psi_1^* \cdot \psi_2 \rangle = g^{(1)} \cdot \sqrt{\left\langle |\psi_1|^2 \right\rangle \cdot \left\langle |\psi_2|^2 \right\rangle}$, where $g^{(1)}$ is the first order correlation function between the fields ψ_1 and ψ_2, defined as in § 1.6.3. Therefore Eq. 2.1 reads:

$$I = \left\langle |A_1|^2 \right\rangle + \left\langle |A_2|^2 \right\rangle + \sqrt{\langle A_1^2 \rangle \langle A_2^2 \rangle} \left(g^{(1)} + g^{(1)*} \right),$$

where $g^{(1)} = \frac{\left\langle A_1 \cdot A_2 \cdot e^{i(\varphi_2 - \varphi_1)} \right\rangle}{\sqrt{\left\langle |A_1|^2 \right\rangle \cdot \left\langle |A_2|^2 \right\rangle}}$ is expressed in terms of the field's amplitude.

In the Michelson interferometer a retroreflector configuration has been chosen, this allows to correlate opposite points of the condensate. The retroreflector is mounted in a computer controller piezo-electric element, which has a displacement in a nanometric scale. By moving the piezo, the length of one arm of the interferometer is changed, allowing a very precise scanning of the relative phase (Θ) between the two arms. Besides, the retroreflector has a long delay line (maximum delay of 1.7 ns) that allows to prove the temporal coherence properties. Figure 2.5(a) shows the experimental setup with the Michelson interferometer.

The intensity of the interference pattern formed by the field $E_M(\vec{r})$ and the symmetrically inverted field $E_R(\vec{r})$ at the output of the interferometer reads:

$$\begin{aligned} I_{int}(\vec{r}, -\vec{r}) &= \mid E_M(\vec{r}) \mid^2 + \mid E_R(\vec{r}) \mid^2 \\ &+ 2A_M(\vec{r}) A_R(-\vec{r}) cos(\vec{k}\vec{r} + \Theta + (\phi(\vec{r}) - \phi(-\vec{r}))) g^{(1)}(\vec{r}, -\vec{r}) \end{aligned} \tag{2.2}$$

where just the real part of Eq. 2.1 has been considered, Θ is the relative phase between the two arms of the interferometer and $\vec{k}\vec{r} = k_x x + k_y y$, with $k_x = k\frac{d_x}{f}$ and $k_y = k\frac{d_y}{f}$ takes into a count the displacement induced by the retroreflector. The term $g^{(1)}(\vec{r}, -\vec{r})$ is the first order spatial correlation function of the condensate.

Equation 2.2 can be re-expressed in terms of experimental variables:

$$\begin{aligned} I_{norm} &= g^{(1)}(\vec{r}, -\vec{r}) cos(\vec{k}\vec{r} + \Theta + (\phi(\vec{r}) - \phi(-\vec{r}))) \\ &= \frac{I_{int}(\vec{r}, -\vec{r}) - I_M(\vec{r}) - I_R(-\vec{r})}{2\sqrt{I_M(\vec{r}) I_R(-\vec{r})}} \end{aligned} \tag{2.3}$$

here I_{int} is the intensity of the interference pattern, and I_M, I_R are the intensities of the mirror and retroreflector arm, respectively. Then, scanning the phase Θ of the interferometer a sinusoidal function will be obtained for each pixel, whose amplitude is $g^{(1)}(\vec{r}, -\vec{r})$, a sinusoidal fit of each measurement is shown in Fig. 2.5(b).

To obtain the first order temporal correlation function, a slightly different procedure is followed: now the scan over the interferometer phase Θ is done with the delay line, achieving a significant phase difference between the two arms of the interferometer and recording the interferogram. Here $g^{(1)}$ is extracted from the contrast, c, of the interference fringes, given by

$$c(t) = \frac{I_{max}(t) - I_{min}(t)}{I_{max}(t) + I_{min}(t)} = \frac{2\sqrt{I_M(t) I_R(t)}}{I_M(t) + I_R(t)} g^{(1)}(t) \tag{2.4}$$

where I_{max} and I_{min} are the intensities of the maximum and minimum of the interference fringes.

This is the general expression for the case where the intensities of the two arms are different; in our setup the intensities are equal, hence the contrast gives the first order temporal correlation function.

When the phase of the condensate needs to be measured, a Mach-Zehnder interferometer setup is used [see Fig. 2.6].

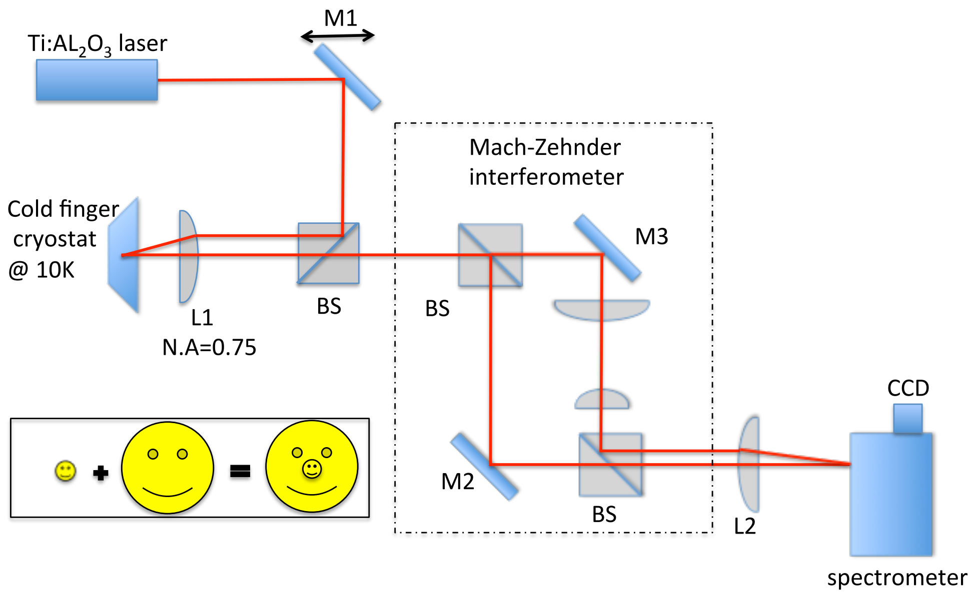

Figure 2.6: Mach-Zehnder interferometer setup. Here M1, M2, M3 are mirrors, BS are beam splitters L1 and L2 are the objective lens and the real space imaging lens respectively, RR is the retroreflector. A telescope is put in one of the interferometer arms to enlarge the condensate image and get a constant phase reference, this is shown by the inset.

The phase of the condensate is obtained by using the Fourier transform method, in the so-called digital off-axis holography [63]. Applying a Fast Fourier Transform (FFT) to an interference pattern [Fig. 2.7(a)] measured at the output of the interferometer, formed by the emission of the condensate and a reference field, and taking into account the interference pattern is given by Eq. 2.1, one obtains:

$$\begin{aligned} FFT(I) &= FFT(|A_1|^2 + |A_2|^2) \\ &+ FFT\left(A_1^* A_2 e^{i(\varphi_2-\varphi_1)}\right) \\ &+ FFT\left(A_2^* A_1 e^{-i(\varphi_2-\varphi_1)}\right) \end{aligned} \tag{2.5}$$

The first term after the equality is located at the origin of the Fourier space, the other two terms are placed symmetrically with respect to the origin and its position is determined by the relative angle between the two arms of the interferometer [see Fig. 2.7(b)]. By filtering out the term at the origin and one of the oscillatory term, the remaining term corresponds to a complex number in real space [see Fig. 2.7(c)]. Therefore when this term is brought back to the real space by performing an inverse FFT (iFFT), the result is a complex number whose phase gives the phase difference between the two fields that form the interference. In order to obtain the phase of the emission, and not the relative phase, a pair of lenses is set in one of the arms of the interferometer to get an enlarged image of the condensate, which acts as a reference field with a constant phase [see Fig. 2.7(d)].

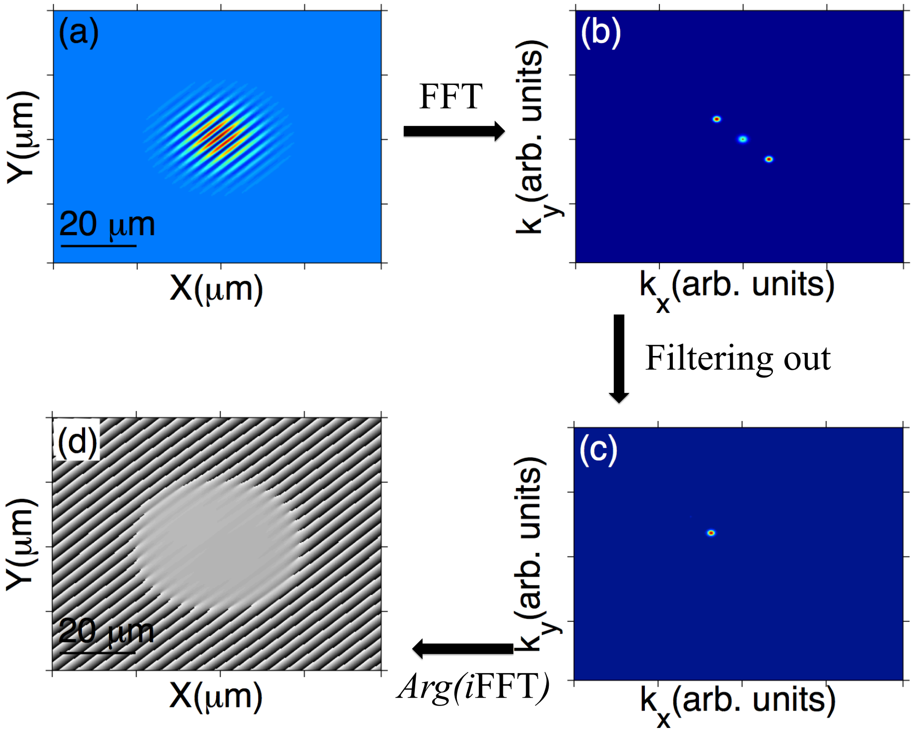

Figure 2.7: Retrieval of the phase. (a) Interference pattern formed by the fields defined in Eq. 2.1. (b) Fourier transform of Fig. (a) where three term are seen. (c) Result of filtering out the term at the origin and one of the oscillatory terms. (d) Phase extracted from (c)

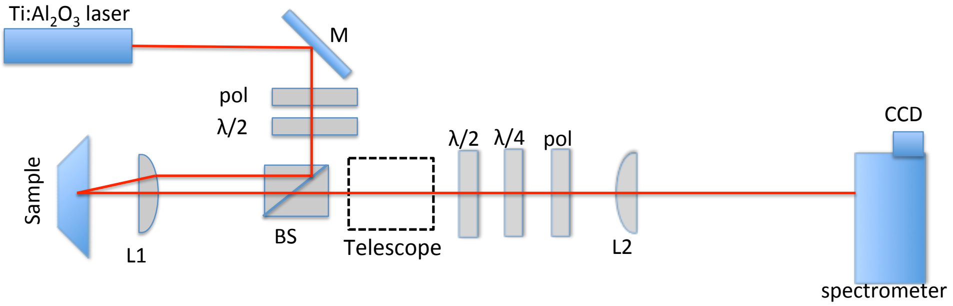

Figure 2.8: Setup for polarization measurements. M is a mirror, pol are linear polarizers, $\lambda/2$ are half waveplate, BS is a beam splitter, L1 and L2 are the objective lens and the real space imaging lens, respectively and $\lambda/4$ is a quarter waveplate. The combination of the half and quarter waveplates plus the linear polarizer allows to determine the Stokes parameters from the emission of the sample. The dashed square represents the same telescope described in Fig. 2.4(a)

2.5 Setup for polarization resolved studies

The polariton's pseudo-spin can be determined by measuring the Stokes parameters (S_0, S_1, S_2, S_3), where S_0 is the total intensity and the last three components are related to a degree of polarization by:

$$S_1 = \frac{I_H - I_V}{I_H + I_V},\ S_2 = \frac{I_D - I_A}{I_D + I_A},\ S_3 = \frac{I_{\circlearrowright} - I_{\circlearrowleft}}{I_{\circlearrowright} + I_{\circlearrowleft}} \tag{2.6}$$

where I_j are the intensities in the horizontal (H), vertical (V), diagonal (D), anti-diagonal (A) linear basis, and right- ($\circlearrowright$), left-handed ($\circlearrowleft$) correspond to the intensity in the circular basis. Therefore, S_1 is the degree of linear polarization in the basis given by H/V, S_2 is the degree of linear polarization in the basis given by D/A and S_3 is the degree of polarization in the basis given by $\circlearrowright/\circlearrowleft$. To measure each one of these intensities, a combination of half- and a quarter-waveplates with a linear polarizer was set up, as shown in Fig. 2.8. In order to remove the polarization sensitivity of the spectrometer's diffraction grating, the linear polarizer is oriented vertically (0^{o}) and fixed, what implies that the detected signal will be always linearly polarized in the vertical direction. Thus, the intensities are measured by proper alignment of the axes of each waveplate with respect to the linear polarizer. It is worthwhile noticing that, for an incoming vertically polarized light, when the axes of the three elements are aligned to 0º, all the intensity is detected. The following table shows the orientation angles at which each of the polarization optics elements should be aligned so that all the light reaches the detector for different linearly- (V, H, D, A) and circularly- (↻, ↺) polarized intensities intensity.

Incoming polarization state	$\lambda/2$	$\lambda/4$	Pol.
V (1)	0º	0º	0º
H (2)	45º	0º	0º
D (3)	22.5º	0º	0º
A (4)	-22.5º	0º	0º
↻ (5)	0º	45º	0º
↺ (6)	0º	-45º	0º

Table 2.1: Orientation of the different polarization elements to detect the maximum intensity for different polarization states of the incoming light.

A proof of the validity of this Table is presented in the Annex at the end of the Chapter.

2.6 Cryostat

As the microcavity sample is a *GaAs* based sample, the working temperature has to be low enough to avoid the dissociation of excitons, therefore the sample is put in a cold finger cryostat (*Janis* ST-500 Microscopy Cryostat) with a nominal vibration of ∼60 *nm* in 30 *min.* when the cryostat is mounted in an isolated optical table. A temperature controller (*Lakeshore* Mod. 331S) allows to cool down the sample with liquid helium up to 4 K (all the experiments were done at 10 K). Moreover the cryostat is mounted in a three dimensional travel stage which allows to scan the position of the sample.

2.7 Annex

We present here the Mueller matrix method to show that the combinations of the polarization elements written in Table 2.1 are the correct ones. We apply, as an example, this formalism to the case of right-handed circularly polarized input light.

In this description, light is represented by a column vector given by the four Stokes paramaters:

$$\begin{pmatrix} S_0 \\ S_1 \\ S_2 \\ S_3 \end{pmatrix} \tag{2.7}$$

The first element represents the total intensity S_0; the second, S_1, corresponds to the degree of linear polarization in the horizontal/vertical basis; the third one, S_2, constitutes the degree of linear polarization in the diagonal/anti-diagonal basis and the fourth one, S_3, is the degree of circular polarization.

For the sake of compactness we shall write the column vector as a row $\left[\begin{pmatrix} S_0 & S_1 & S_2 & S_3 \end{pmatrix}\right]$, in the following text.

The Mueller matrix for a retarder with its axis oriented at an angle θ and retardation δ is given by;

$$\begin{pmatrix} 1 & 0 & 0 & 0 \\ 0 & cos^2 2\theta + cos\delta sin^2 2\theta & cos2\theta sin2\theta - cos2\theta cos\delta sin2\theta & sin2\theta sin\delta \\ 0 & cos2\theta sin2\theta - cos2\theta cos\delta sin2\theta & cos\delta cos^2 2\theta + sin^2 2\theta & -cos2\theta sin\delta \\ 0 & -sin2\theta sin\delta & cos2\theta sin\delta & cos\delta \end{pmatrix} \tag{2.8}$$

Turning back to our example, for a half and a quarter waveplate the retardation are $\delta = 180^{\text{o}}$ and $\delta = 90^{\text{o}}$, respectively, therefore when the $\lambda/2$ plate is vertically oriented (0^{o}) and the $\lambda/4$ plate is oriented at 45^{o} the previous matrix reduces to:

$$\begin{pmatrix} 1 & 0 & 0 & 0 \\ 0 & 1 & 0 & 0 \\ 0 & 0 & -1 & 0 \\ 0 & 0 & 0 & -1 \end{pmatrix}_{\frac{\lambda}{2},0^{\underline{o}}} \quad and \quad \begin{pmatrix} 1 & 0 & 0 & 0 \\ 0 & 1 & 0 & 1 \\ 0 & 0 & 1 & 0 \\ 0 & -1 & 0 & 0 \end{pmatrix}_{\frac{\lambda}{4},45^{\underline{o}}} \tag{2.9}$$

Finally, for the linear polarizer (retardation $\delta = 0^{\underline{o}}$), which is vertically oriented ($0^{\underline{o}}$), its Mueller matrix is given by:

$$\frac{1}{2}\begin{pmatrix} 1 & -1 & 0 & 0 \\ -1 & 1 & 0 & 0 \\ 0 & 0 & 0 & 0 \\ 0 & 0 & 0 & 0 \end{pmatrix}_{L,0^{\underline{o}}} \tag{2.10}$$

Light with an initial state of polarization $\vec{S}_{in}$ passing through an optical element M, will come out in the polarization state $\vec{S}_{out}$, this is represented by: $\vec{S}_{out} = M\vec{S}_{in}$. For our setup, there are three optical elements M: a half waveplate, a quarter waveplate and finally a linear polarizer, which are represented by $M_{\frac{\lambda}{2}}$, $M_{\frac{\lambda}{4}}$ and M_L respectively, hence light that passes through this system is represented by:

$$\vec{S}_{out} = M_L M_{\frac{\lambda}{4}} M_{\frac{\lambda}{2}} \vec{S}_{in} \tag{2.11}$$

We apply the aforementioned formalism to the example of an input defined by a righ-handed circularly polarized light, given by the vector $\left[\begin{pmatrix} 1 & 0 & 0 & 1 \end{pmatrix}\right]$. According to Table 2.1, using the combination (5) all the light should reach the detector. Keeping in mind that the linear polarizer is always oriented vertically ($0^{\underline{o}}$), the $\vec{S}_{out}$ should be $\left[\begin{pmatrix} 1 & -1 & 0 & 0 \end{pmatrix}\right]$.

Equation 2.11 for the combination (5) reads:

$$\vec{S}_{out} = M_{L,0^{\underline{o}}} M_{\frac{\lambda}{4},45^{\underline{o}}} M_{\frac{\lambda}{2},0^{\underline{o}}} \vec{S}_{in}$$

$$\vec{S}_{out} = \frac{1}{2}\begin{pmatrix} 1 & -1 & 0 & 0 \\ -1 & 1 & 0 & 0 \\ 0 & 0 & 0 & 0 \\ 0 & 0 & 0 & 0 \end{pmatrix}\begin{pmatrix} 1 & 0 & 0 & 0 \\ 0 & 1 & 0 & 1 \\ 0 & 0 & 1 & 0 \\ 0 & -1 & 0 & 0 \end{pmatrix}\begin{pmatrix} 1 & 0 & 0 & 0 \\ 0 & 1 & 0 & 0 \\ 0 & 0 & -1 & 0 \\ 0 & 0 & 0 & -1 \end{pmatrix}\begin{pmatrix} 1 \\ 0 \\ 0 \\ 1 \end{pmatrix}, \qquad (2.12)$$

operating one obtains:

$$\vec{S}_{out} = \begin{pmatrix} 1 \\ -1 \\ 0 \\ 0 \end{pmatrix}$$

which proves that all the intensity reaches the detector ($S_0 = 1$).

Chapter 3

Phase correlation in 2D and 1D systems

The signature of a transition from a thermal distribution to a condensed phase is given by the build up of the off-diagonal long-range order (ODLRO) [28] and is characterized by the existence of an order parameter, in the case of a condensate a macroscopic wave function with a well defined phase. This chapter describes the properties of the first order correlation function for the signal state of the OPO process in microcavity exciton-polaritons. As it was pointed out in § 1.6, the appearance of ODLRO can be measured by the normalized single particle density matrix, which is the first order correlation function. We will use this quantity to measure the phase correlation of a polariton field created under OPO configuration. Even though the OPO polariton condensate is a system in dynamic equilibrium between three states massively occupied, we will show that, it presents a non-vanishing ODLRO.

3.1 Coherence in a 2D OPO system

Spatial coherence properties have been studied theoretically for the OPO condensate by Carusotto and Ciuti [58]. In that work, the first order correlation function ($g^{(1)}$) is studied numerically for a finite condensate, paying special attention to its behavior across the OPO parametric threshold, defined as a function of the detuning of the excitation laser with respect to the phase-matching conditions (E_{Th}). It is found that, for excitation frequencies ω_p below that of the threshold $\hbar\omega_p < E_{Th}$, $g^{(1)}$ has a finite correlation length. Increasing ω_p in order to approach E_{Th}, maintaining fixed the pump angle (and therefore the wavevector), they predict the build up of macroscopic phase coherence extending over the entire condensate [58].

In this regime, when the phase coherence extends over the full condensate, the spatial fluctuations are negligible, therefore the temporal coherence properties should be captured by a theory developed by Whittaker and Eastham [64]. In their theory, the temporal coherence is limited by fluctuations in the particle number, which due to the polariton-polariton interactions imply a broadening of the emission [57, 65-67]. This broadening mechanism, however, would be suppressed if the intensity fluctuations become very fast, in a form of motional narrowing effect [68]. Thus, for appropriate pump powers and condensate areas, very long coherence times could be obtained. Using a high-quality sample and a very narrow-bandwidth pump laser, we obtain spatially extended single-mode polariton condensates, with uniform spatial coherence extending over the entire pump spot. The temporal coherence decay of the condensates reveals two timescales associated with the interaction-induced broadening of the condensate and the intensity fluctuations, respectively. We show that the finite-size scaling laws describing the variation of these timescales with condensate area qualitatively agree with the theory. The main factor that limits the coherence is the quality of the cavity: the presence of defects creates a disorder potential that traps the condensate, leading to multi-mode and inhomogeneous states [69]. Another, very important, detrimental effect in the coherence that needs to be considered is due to the fluctuations in intensity and frequency of the excitation laser. This hinders the attainment of the intrinsic coherence of the condensate. Previous studies [32, 69, 70] have been performed by non-resonantly pumping the microcavity, and in such cases the resulting distribution of the population at the bottom of the lower polariton branch is subjected to fluctuations due to the reservoir of particles at the bottleneck. These fluctuations, broadening the distribution of polaritons in energy and momentum space, translate, according to the Wiener-Khinchin identity [71, 72], into a faster decay of the temporal and spatial coherence.

Although analogous broadening by the fluctuating population of pump polaritons can occur in the OPO [57], the pump power threshold (P_{Th}) for a resonant-gain process is much lower than that for non-resonant gain and the effect of the reservoir polaritons is not relevant, since the reservoir is either completely empty or very weekly occupied. Thus the coherence exhibited by an OPO polariton-condensate is expected to decay over much longer times and larger distances than that produced by non-resonant techniques. Here we realize experimentally a spatially extended, and with long temporal coherence, condensate in the OPO configuration and identify the mechanism driving the extended temporal coherence. This is mainly due to the fact that the pump laser, frequency locked, has a spectral bandwidth in the order of $\sim 10^{-10}$ electron-volts (75 kHz frequency width), which allows us to control very precisely the OPO phase-matching conditions.

3.1.1 Power threshold

In order to have a complete control over the OPO conditions leading to the formation of extended condensates, in this section the decay of the first order correlation function is studied as a function of the pump power. The microcavity is excited with a pump spot of 40 μm diameter, and three different regimes are investigated: below power threshold for condensation, about power threshold and well above power threshold. For each one of this regimes the OPO phase-matching conditions are set, first, by fixing the pump power and then adjusting the k vector and energy of the laser, in order to fulfill the conservation of energy and momentum.

By pumping the system below the power threshold (the power threshold is about $\sim$50 mW), with a pump power of $\sim$ 40 mW, with an energy of $\sim$1551.1 meV and at a k vector of $\sim$ 1.5 μm^{-1} (angle of incidence $\sim$11°), condensation is not achieved; and the corresponding emission from the sample covers the whole pump spot size, as is shown in Fig. 3.1(a). The interference pattern, shown in Fig. 3.1(b), displays a significant contrast only at the center of the emission, which corresponds to the autocorrelation point. Figure 3.1(c) presents the coherence map, that is the first order correlation function, which appears in the region corresponding to the autocorrelation point. By taking a horizontal profile of the coherence map, of 0.26 μm (1 pixel width), centered at the maximum of it, a coherence length of about 2.4 μm is extracted from a Lorentzian fit, as shown in Fig. 3.1(d). This value corresponds to the thermal de Broglie wavelength for a gas of non-condensed polaritons. Figure 3.1(e) shows the phase map of this non-condensed emission. Under these conditions, the microcavity is in the linear regime, as corroborated by the coherence and phase maps (Figs. 3.1(c) and 3.1(e) respectively), and the coherence is limited to the autocorrelation region.

In order to bring the microcavity into condensation, the pump power is increased, keeping the excitation area constant. Therefore, a proper adjustment of the phase-matching condition needs to be done: the energy and k vector of the laser must be increased to compensate for the blueshift caused by polariton-polariton interactions, which renormalize the LPB. Thus, the pump power corresponds to 60 mW, slightly above the power threshold, the laser energy is tuned at 1551.76 meV and the k vector at 1.7 μm^{-1} (∼12.5°).

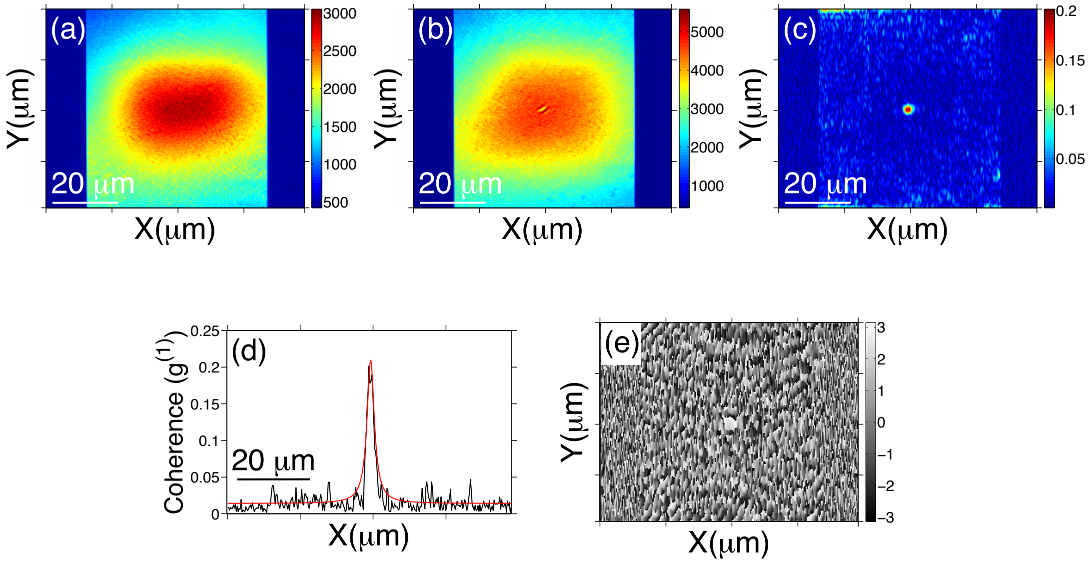

Figure 3.1: Microcavity pumped below power threshold (40 mW). The laser at 1551.1 meV is impinging on the sample at an angle of 11°. (a) Shows the real space emission of the microcavity. In (b) the interference pattern is depicted, it observed a significant contrast just at the autocorrelation point. (c) depicts the coherence map. In (d) is shown a slice of the coherence map presented in (c), the red line corresponds to a fit with a Lorentzian function, with a linewidth of 2.4 μm (FWHM). The phase map of the emission is shown in (e). All the data are energy integrated and the temperature of the sample is kept at 10 K.

Under these conditions, the condensation takes place in a smaller region than the pump spot size. This is due to the fact that the pump beam has a Gaussian profile, therefore it does not have a homogeneous power distribution, being higher at the center of the beam and decreasing towards its rim. Thus, the necessary pump power to trigger the OPO process is limited to a smaller area that of the actual pump spot size leading to condensation in a reduced size. The real space emission, shown in Fig. 3.2(a), depicts a emission of the condensate in a reduced zone compared to the non-condensed case.

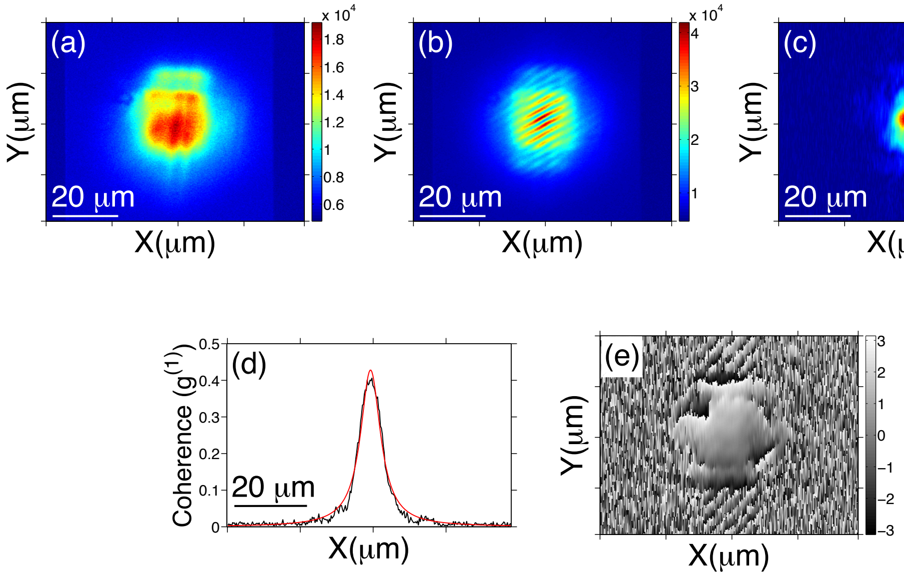

Figure 3.2: Microcavity pumped slightly above the power threshold (60 mW). The laser is set at 1551.76 meV at an angle 12.5° with respect to the normal. (a) Shows the real space emission of the microcavity pumped slightly above power threshold. In (b) the interference pattern is shown, which is more extended compared to the non-condensed case, but is smaller than the pump spot size; (c) depicts the coherence map and (d) represents a slice of the coherence map shown in (c), the red line corresponds to a fit with a Lorentzian function, with a linewidth of 6.5 μm (FWHM). The phase map of the condensate, which does not present any singularity where the condensate is defined, is given in (e).

The interference pattern is shown in Fig. 3.2(b), which now extends along all the condensate emission area. The coherence map and a horizontal slice of it are shown in Figs. 3.2(c) and 3.2(d), respectively. A fit with a Lorentzian function of the profile shown in Fig. 3.2(d) reveals that the coherence length in the condensed phase has increased up to 6.5 μm, which corresponds to 2.7 times the coherence length for the uncondensed situation. The phase map also shows a size increment as can be seen in Fig. 3.2(e).

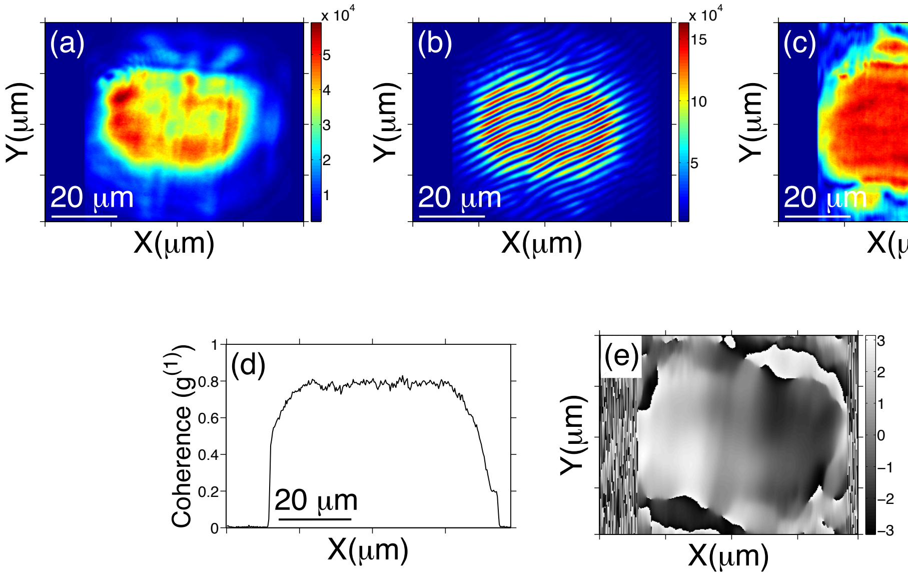

Figure 3.3: Microcavity pumped well above power threshold (458 mW). The laser's energy is 1551.81 meV and the angle is at 13.6°. (a) shows the real space emission of the microcavity, which is extended to the whole pump spot size. (b) presents the interference pattern, whose contrast covers the full emission. (c) depicts the coherence map, where a constant degree of coherence is observed in all the condensate. (d) Represents a slice of the coherence map shown in (c). The phase map of the condensate, without any singularity in the condensed region, is presented in (e).

A further increase of the pump power causes that the OPO process is triggered in the whole pump area, therefore the condensate area is determined by the pump spot size. Figure 3.3(a) shows the real space emission for a pump power of 458 mW, with a k vector of

1.85 μm^{-1} (~13.6°) and an energy of 1551.81 meV. This emission is quite homogeneous and covers the whole pump spot. An inspection of the interference pattern, shown in Fig. 3.3(b) reveals a very uniform contrast all over the emission area. The coherence map, shown in Fig. 3.3(c), demonstrates that the coherence is almost constant over all the pump spot. A horizontal slice of the coherence map is shown in Fig. 3.3(d): now the coherence does not decay within the pump spot but rather is extended and almost flat. Figure 3.3(e) shows the phase map, here the phase, as it can be deduced from the coherence map, is also extended.

A extended coherence for a finite size condensate under an OPO regime is predicted in [58], this will be discussed in more detail in § 3.1.3.

Now we focus on the temporal decay of the first order correlation function. Here, we study the same three regimes described above, the temporal decay of $g^{(1)}(\tau) = \left(\frac{\langle E^*(t)E(t+\tau)\rangle}{\langle E^*(t)\rangle\langle E(t)\rangle}\right)$ is extracted following the procedure explained in § 2.4. The temporal decay of $g^{(1)}$ is shown in Figs. 3.4 for three different excitation powers: a clear increase in decay time with increasing power is observed (notice the different ranges of the abscissa in the figures).

By pumping the microcavity below the power threshold for condensation (0.8 P_{Th}), the interference pattern has significant contrast just in the autocorrelation point as is observed in Fig. 3.1(b). The temporal decay is shown in Fig. 3.4(a), where the fit to the data is given by a mono-exponential function with a characteristic decay time of 7 ps, which is of the order of the polariton lifetime for this microcavity. The fitted curve to the experimental data is given by:

$$g^{(1)}(t) \sim e^{-t/\tau} \tag{3.1}$$

The temporal decay for a pump power above the power threshold (1.2 P_{th}), is shown in Fig. 3.4(b). Here, the observed decay has a Gaussian shape rather than the mono-exponential one observed in the non-condensed case (the change of the function describing the decay will be addressed later in this section). The red curve shown in Fig. 3.4(b) is a Gaussian fit, from where a characteristic decay time of 86 ps has been extracted (a mono-exponential fit gives a decay time of 80 ps, however, as one can see by direct inspection, the decay is not

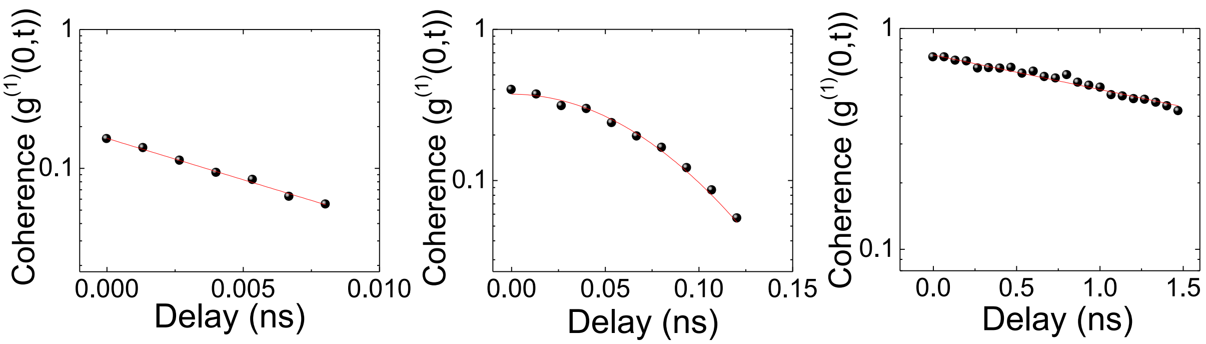

Figure 3.4: Temporal decay of the first order correlation function. In (a) the temporal decay is shown when the system is pumped below the power threshold (0.8 P_{Th}), it presents a fast exponential decay, with a decay time of 7 *ps* given by the fit shown by the red curve. (b) shows the decay for a pump power slightly above the power threshold (1.2 P_{Th}), under these conditions the decay can be fitted by a Gaussian function, as depicted by the red line, which obtains a characteristic time of 86 *ps*. In (c) the decay is depicted for pump power well above the power for condensation threshold (9 P_{Th}). By fitting an exponential curve (red curve) a decay time of 2.7 *ns* is extracted. The three graph are in semilog scale to facilitate the perception of the different characteristic shapes of the decays.

exponential), this represents an increment of one order of magnitude with respect to the decay time for non-condensed case. The curve used to fit the experimental data is:

$$g^{(1)}(t) \sim e^{-(t/\tau)^2} \tag{3.2}$$

Increasing further the pump power to 9 P_{Th}, the condensate becomes spatially extended to the whole spot size, as is shown by the coherence map of Fig. 3.3(c). The increase in the spatial coherence is accompanied by an increase in the temporal decay. This is depicted in Fig. 3.4(c), where Eq. 3.1 has been used to fit the experimental data (red curve): the characteristic decay time is 2.7 *ns*. This coherence time, for polariton condensates created under the OPO regime, is much longer than the previously reported times. We have even achieved longer coherence times lasting up to 3.2 *ns* as we will show in § 3.1.3.

The temporal decay of $g^{(1)}$ gives the time scale during which the phase of the condensate can be consider coherent, but it also provides a measurement of the spectral distribution of the emission source, in this case the polariton condensate. Applying a Fourier transform to $g^{(1)}$, the spectral distribution is obtained [37]. The genuine linewidth of the condensate cannot be obtained in our case by a direct measurement, due to the spectral resolution of the spectrometer (100 μeV). It is worth to notice that, for the sake of convenience, the spatial and the temporal correlations are considered to be independent, thus the power spectrum can be written as: $S(\omega) = \mathcal{F}(g^{(1)}(0,t))$, where the symbol $\mathcal{F}$ denotes the Fourier transform operator. Figure 3.5 shows the Fourier spectrum, calculated using Eq. 3.1, with the respectively decay time, for the cases that show an exponential decay, and using Eq. 3.2 for the case with a Gaussian decay, for the three situations exposed above. Figure 3.5(a) shows the lineshape of the distribution corresponding to a Lorentzian curve with a full width at half maximum of 75 GHz, corresponding to an energy width of 310 μeV. This value is considerably lower than the experimentally determined from Fig. 3.5(d), which obtains a width of 110 GHz. The difference arises from the fact that, below threshold the emission comes from different k vectors, so the Fourier spectrum has the form $S(\omega, k)$, which cannot be separated as assumed above. Despite the fact that the spatial and temporal frequencies cannot be considered as independent, as we have done in our approximation, the Fourier transform obtains a relatively good estimation of the linewidth.

When the system is condensed, the linewidth decreases drastically, but, as aforementioned, this cannot been measured in our setup due to the spectral resolution of the spectrometer. Thus, the linewidth is extracted from the Fourier spectrum shown in Fig. 3.5(b), obtaining 5.2 GHz (21.5 μeV), whilst the experimental measured one is given by the FWHM of Fig. 3.5(e), which is 31 GHz (128 μeV). Here, as the condensation takes place at $k = 0$, the Fourier spectrum can be considered independent of the spatial frequencies.

The longer coherence time achieved by pumping harder the microcavity should be also reflected in a further narrowing of the linewidth. Figure. 3.5(c) shows the Fourier spectrum, from where a linewidth of 0.18 GHz (0.7 μeV) is extracted. The experimentally measured value is 27 GHz (112 μeV) obtained from Fig. 3.5(f). In both cases above threshold, the experimentally determined linewidth is similar, but if the linewidth is extracted from the Fourier spectrum, notable differences appear. Since the temporal decay of the first order correlation function shows different shapes and decay times, the genuine spectra are also different in shape and width.

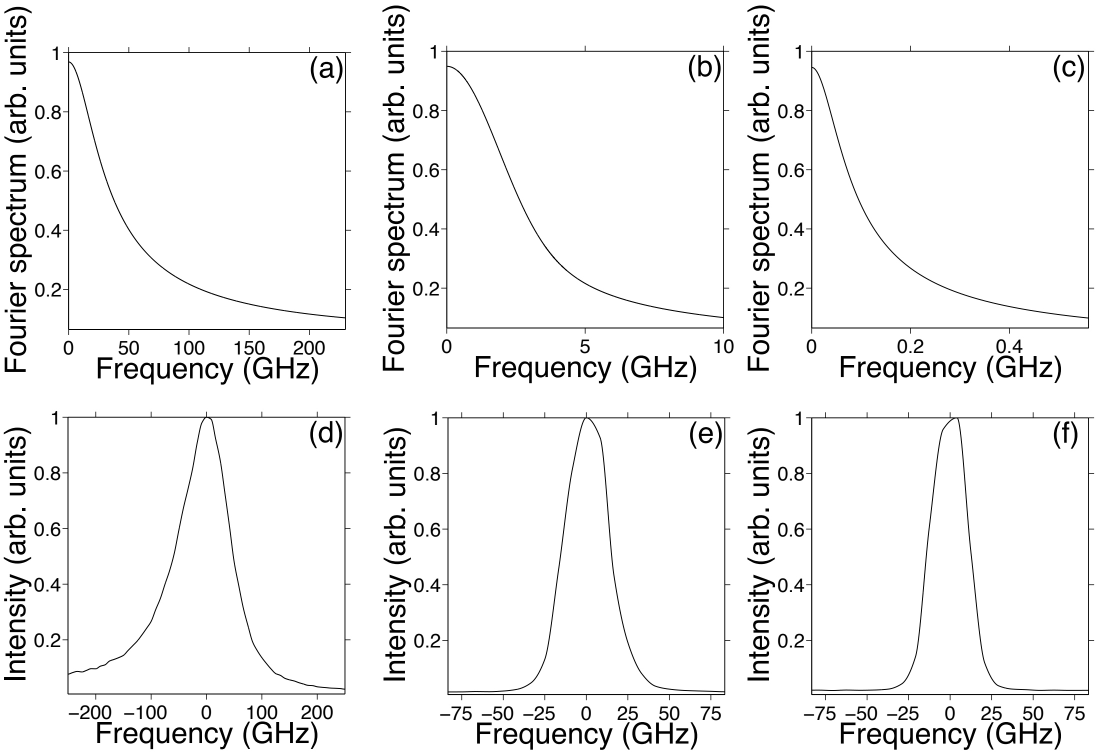

Figure 3.5: Fourier transform of the $g^{(1)}$. (a) shows the Fourier spectrum for the non-condensed case ($0.8\ P_{Th}$), with a Lorentzian lineshape (FWHM of 75 GHz). In (b) the case where the sample is pumped slightly above the threshold is presented ($1.2\ P_{Th}$), here the lineshape is Gaussian with a linewidth of 5.2 GHz. (c) depicts the spectrum when the pump power is well over the power threshold ($9\ P_{Th}$), the lineshape is Lorentzian with a FWHM of 0.18 GHz. Note the different ranges of the abscissas in (a), (b) and (c). In (d) the experimentally measured linewidth with a FWHM of 110 GHz. The panel (e) renders the linewidth, when the pump power is slightly above threshold, the width is 31 GHz. (f) displays the measured linewidth pumping the microcavity well above the power threshold, here the width is 26 GHz very close to the value when the microcavity is pumped slightly above threshold, and in both cases limited by the experimental resolution.

The different lineshapes shown by the decay of $g^{(1)}$, indicates that the condensate experiences several regimes, depending on the strength of the pump. Below threshold $g^{(1)}$ shows a fast exponential decay: in this case the system is dominated by the losses. Slightly above threshold, there is a close match between gain and losses, that brings the condensate into a static regime [64], *i.e.* the number fluctuations become slow as compared with the coherence time. This was also the case in Ref. [73] where the temporal decay of $g^{(1)}$ showed a characteristic Gaussian shape reaching coherence times up to 200 ps. A further increase of the pump power, causes a saturation of the gain, thus the slowing-down in the number fluctuations no longer occurs and the condensate falls into a motional narrowing regime, where very long coherence times can be achieved. This regime is characterized by an exponential decay [64].

3.1.2 Spot size dependence

Here, the influence of the pump spot size on the coherence time is investigated; in order to do so, the pump power is chosen to be well above the power threshold. The variation in area is obtained changing the optics before the lens focusing on the sample, so that the range of pump angles is kept as close as possible in the different cases. In this way we are able to perform a controlled comparison with theory, by varying the area while maintaining the same power density. We obtain a predominantly exponential decay for $g^{(1)}$, with a coherence time reaching $T_C = 3.2$ ns (see the definition of T_C below). This is six times longer than the largest value reported in the literature until now for the same material system under OPO conditions [57]. Despite the lack of spatial fluctuations, the coherence time of the condensate, though long, is clearly finite. In general, such a finite correlation time in a state with perfect spatial order is caused by finite-size fluctuations [74], and reflects the absence of true phase transitions in finite systems. A well-known example is the Schawlow-Townes formula for the coherence time of a single laser mode with an average of N photons, $T_c \propto N$. Since $N \propto A$ when the control parameter, defined as the ratio between the pump power P_{ave} and the condensed area A_c ($P_d = {}^{P_{ave}}/_{A_c}$) is constant, the Schawlow-Townes result implies the scaling form $T_c \propto A$. However, as shown in detail below, this scaling law is violated by more than an order of magnitude for the polariton condensates, and the results cannot be understood as a straightforward effect of increasing the particle number. Nevertheless, the results presented may be interpreted in terms of the theoretical model of Ref. [64], in which the linewidth arises from fluctuations in the number of particles. Due to the interactions, such number fluctuations imply energetic fluctuations of the emission, leading to a broad line or a decay of $g^{(1)}$. This is captured by Kubo's result

$$\left|g^{(1)}\left(\tau\right)\right| = exp\left[\frac{2\tau_r^2}{\tau_c}\left(e^{\tau/\tau_r} + \frac{\tau}{\tau_r} - 1\right)\right] \tag{3.3}$$

for the emission from a transition whose energy fluctuates, where τ_c is determined by the width of the (generically Gaussian) distribution of the energy level and τ_r is the characteristic timescale on which the fluctuations occur. If $\tau_r \gg \tau_c$ the fluctuations are slow and the emission reflects the energy distribution of the level, so that the coherence decays on a timescale τ_c. If, however, $\tau_r \ll \tau_c$, a motional narrowing effect leads to an exponential decay, with a much longer coherence time given by $T_C = \frac{\tau_c^2}{2\tau_r}$.

Figure 3.6(a) shows the temporal decay of the first order correlation function, where we have used the Kubo formula Eq. 3.3 to fit the data, for a power density of $\sim$ 10 kW/cm^2, which corresponds to a pump power of $\sim$ 265 mW and an area of $\sim$2.7x10^3 μm^2; a coherence time T_C of $\sim$3.2 ns is obtained. The results shown in Fig. 3.6(b), corresponding to the temporal decay of $g^{(1)}$ for two different power densities keeping the size of the condensate constant ($A = 70\mu m^2$), demonstrate that increasing the power a longer coherence time is achieved. In fact, the coherence time for this condensate of relatively small area $A = 70$ μm^2 increases from $T_c = 0.5$ ns at $P_d = 5.4$ kW/cm^2, to $T_c = 0.9$ ns at $P_d = 10$ kW/cm^2. We note that the coherence decay of the smallest condensate at the lowest power, black squares in Fig. 3.6(b), has considerable structure and does not follow well the Kubo form: in fact neither a Gaussian nor exponential decay provides a good fit to this data, suggesting that this condensate is not a single mode condensate.

In order to elucidate the effects of the number fluctuations, the Kubo formula is used to fit the data for three different areas, keeping the power density fixed at $P_d = 10$ kW/cm^2. For the condensate with a larger area $A = 2.7 \times 10^3$ μm^2, $\tau_c = 0.97$ ns and $\tau_r = 0.15$ ns are obtained fulfilling the inequality for the motional narrowing regime and giving a coherence time $T_c = 3.2$ ns. For an intermediate area $A = 1.3 \times 10^3$ μm^2, we observe a decrease of both parameters $\tau_c = 0.76$ ns and $\tau_r = 0.14$ ns corresponding to $T_c = 2.1$ ns. A further reduction of the area to $A = 70$ μm^2 obtains $\tau_c = 0.20$ ns and $\tau_r = 0.023$ ns, corresponding to a shorter $T_c = 0.9$ ns, still indicating in both cases that the system is in the motional narrowing regime.

This is summarized in Figs. 3.6(c) and 3.6(d), where τ_c and τ_r are respectively plotted as a function of the condensate area. The error bars of the fit parameters τ_r and τ_c are estimated from the regression to Eq. 3.3 and explicitly shown in Figs. 3.6(c) and 3.6(d).

As well as moving to larger areas, another way to have longer decay times, suggested in Ref. [64], is to increase the pump power, with the pump always in the conditions to drive the system in the OPO regime, this was the situation discussed in § 3.1.1.

From the Kubo fits to the data, for a given power, we can extract the scaling $\tau_c \propto A^{0.41\pm0.05}$ [Fig. 3.6(c)]. This is consistent with the dominant dephasing mechanism being the polariton-polariton interaction, suppressed by motional narrowing, in which case the Kubo formula should hold with $\tau_c \propto A^{0.5}$ [64]. Although this implies an increase in the coherence time, T_C, with area, our results show that this increase is restrained because τ_r also increases with area as $\tau_r \propto A^{0.41\pm0.17}$ [Fig. 3.6(d)], so that motional narrowing becomes less effective, giving to the coherence time the trend $T_C \propto A^{0.5}$. This is shown in Fig. 3.7 that depicts T_C as obtained from a fit to an expression similar to Eq. 3.3 which has been rewritten to explicitly contain T_C as a parameter,

$$\left|g^{(1)}(\tau)\right| = exp\left[-\frac{\tau_r}{T_c}\left(e^{\tau/\tau_r} + \frac{\tau}{\tau_r} - 1\right)\right] \tag{3.4}$$

Note that the error bars of T_c are estimated from the regression to Eq. 3.4. The red solid line shows the best fit to a square root dependence on A, while the dashed line corresponds to a linear dependence (Schawlow-Townes mechanism). We note that the square root form provides a better fit to the data, consistent with the linewidth due to polariton-polariton interactions in the motional narrowing regime. The small size of our system and the use of pump powers which are relatively close to threshold, P_{Th}, are responsible for the observed increase of τ_r with area.

Finally, let us discuss briefely the area dependence of τ_r. In the thermodynamic limit, $A \to \infty$, the occupation, n, of a single mode with linear gain γ, linear loss γ_c and nonlinear gain Γ obeys the mean-field rate equation $dn/dt = (\gamma - \gamma_c - \Gamma n)n$ [75]. Linearizing we see that the damping time for number fluctuations is $\tau_r = 1/|\gamma - \gamma_c|$. This timescale is therefore

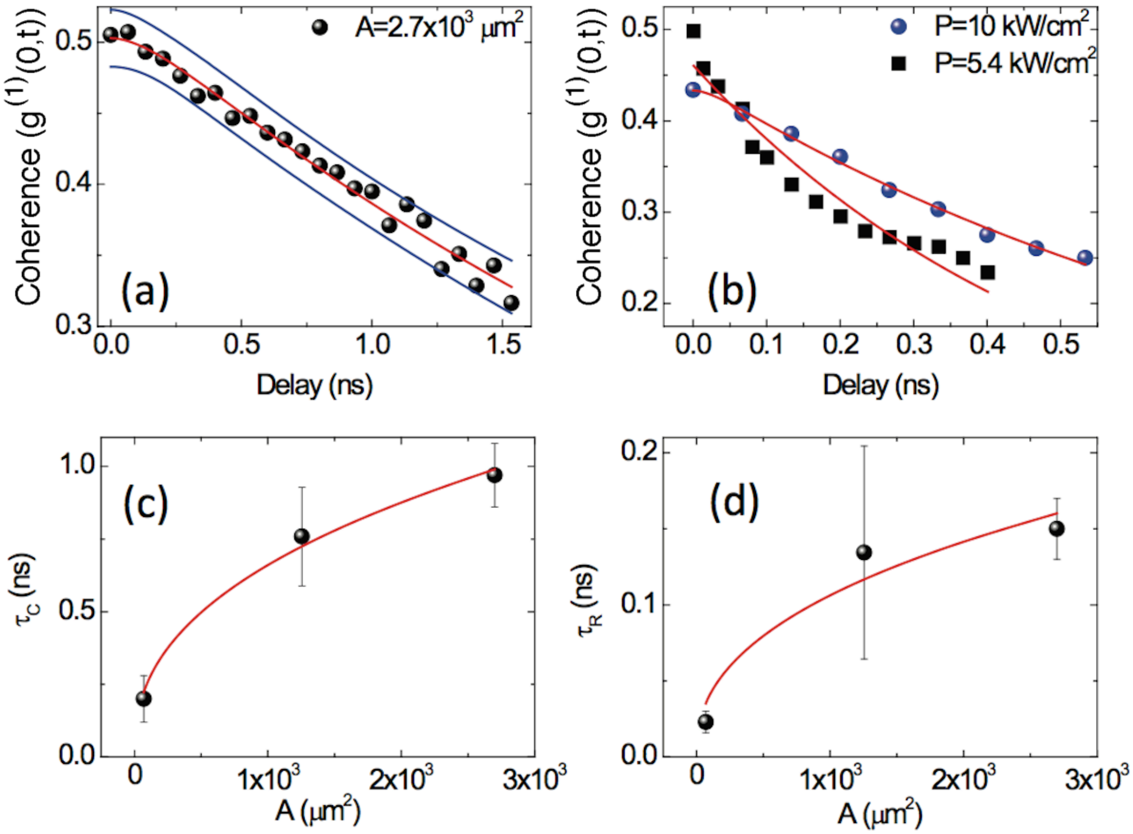

Figure 3.6: (a) Temporal coherence decay above threshold for condensate area 2.7×10^3 μm^2 at a pump power density $P_d = 10$ kW/cm^2, the central line is a fit to Eq. 3.3, side bands define the confidence range in which the experimental points fall within a probability of 95%. (b) Temporal coherence decay for $P_d = 5.4$ kW/cm^2 (black squares) and $P_d = 10$ kW/cm^2 (blue dots) at $A = 70$ μm^2. Lines are fits to Eq. 3.3. Fig. (c) depicts the dependance of τ_c with the condensate area A, the line is a fit to $\tau_c \propto A^x$, with $x = 0.41$ $\pm$ 0.05. In Fig. (d), τ_r as a function of condensate area A is shown, the line is a fit to $\tau_c \propto A^x$ with $x = 0.41 \pm 0.17$. In the last two figures the power density is kept constant at $P_d = 10 kW/cm^2$.

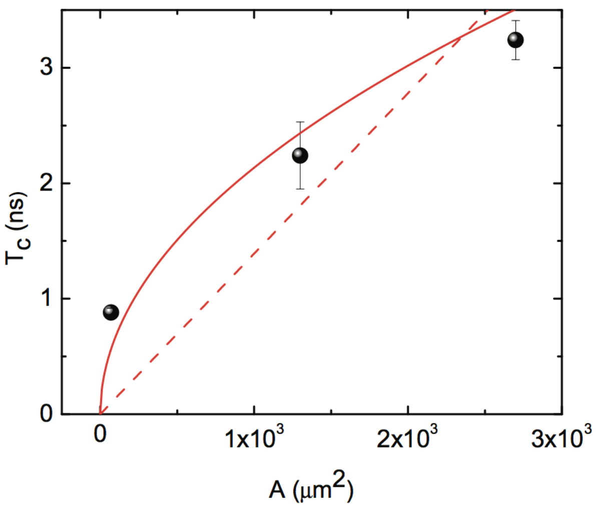

Figure 3.7: Temporal coherence T_c as obtained from Eq. 3.4 as a function of the condensate area A, for the same power density shown in Fig. 3.6 ($P_d = 10\ kW/cm^2$). Red solid line is a fit to square root dependence on area A, , the dashed line corresponds to the best fit to a linear dependence.

independent of area when the rate equation is valid. However, at power threshold, $\gamma = \gamma_c$ and the rate equation predicts a divergence in the relaxation time, which in the finite system must be cut off by fluctuations. Thus, in the threshold region, τ_r initially grows with area, as we observe, before eventually saturating. The scaling in the threshold region may be obtained from the dynamical model described in Ref. [64], which when solved numerically at threshold gives $\tau_r \propto \sqrt{A}$, consistent with Fig. 3.6(d).

3.1.3 Parametric threshold as a function of pump laser-energy

In order to experimentally proof the prediction of [58], the parametric threshold is proved for two different spot sizes. In both cases the pump power is kept well above the power threshold, thus the condensate is spatially determined by the spot size. The phase-matching conditions are properly set for each size, *i.e.* the k vector and energy for the corresponding pump power. Once condensation is achieved, the energy of the laser is varied leaving the pump power and the k vector unchanged.

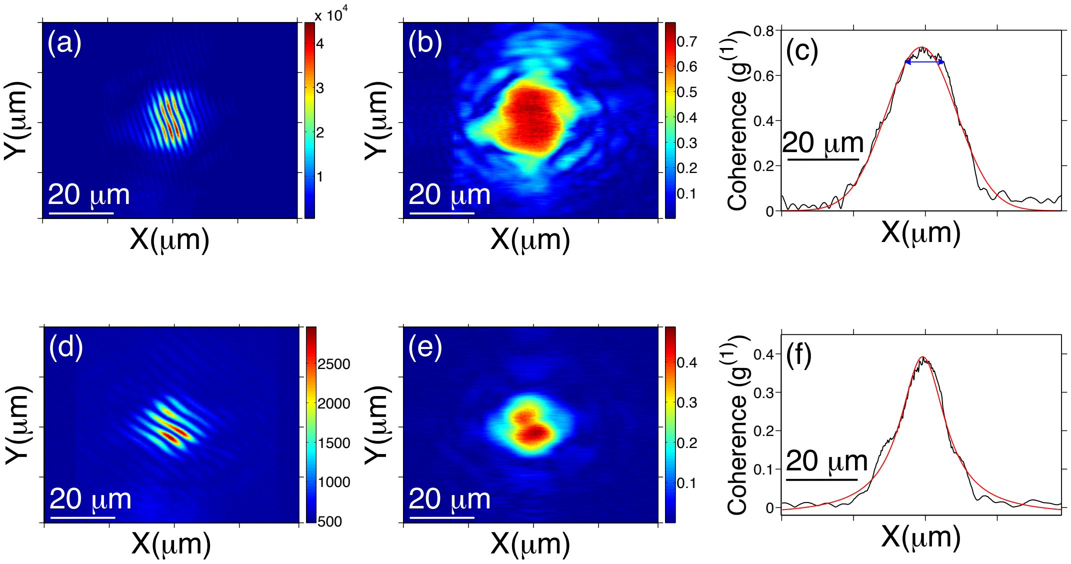

Figure 3.8: Interference pattern (a/d) and corresponding coherence (b/e) of the condensate generated at/below the parametric threshold, E_{Th}, corresponding to a pump energy $E_1 = 1552.28\ meV$/ $E_2 = 1551.51\ meV$ and a power density $P = 13.5\ kW/cm^2$. Horizontal profile at the center (c/f) showing a constant coherence (extended about ∼10 μm, shown by the blue arrow) along the entire condensate for E_1/an exponentially decaying one for E_2. The red lines are Gaussian function used to fit the data.

We start describing the case of a pump spot size of $\sim 10\ \mu m$ with the laser energy set a E_{Th}. The interference pattern and the coherence map are shown in Figs. 3.8(a) and 3.8(b), respectively. The maps are extended to the whole pump spot size. This can be better observed in Fig. 3.8(c), where a horizontal profile of 0.26 μm width (1 pixel) of the coherence map is represented. A fit of a Gaussian function to the profile obtains a width of 13 μm, which is defined as the coherence length (L_C). The longer L_C value than that of the pump spot size is due to a diffusion of polaritons outside the pumping area. The blue arrow displays the region where the coherence map presents a constant value. When the energy of the laser is decreased by $\delta E \equiv E_{Th} - E = 0.77\ meV$ towards lower energies, leaving fixed the pump power and angle, the phase-matching conditions are still partially fulfilled, as it is demosntrated by the observation of the interference pattern depicted in Fig. 3.8(d). By looking at the coherence map, shown in Fig. 3.8(e), a decrease of $g^{(1)}$ is clearly seen, both in the area and in the magnitude, but it still presents a considerable value. More details are given in Fig. 3.8(f), which is a horizontal profile of the coherence map. The fit of a Gaussian function is shown in by the red curve, obtaining a value of $L_C \sim 9\ \mu m$. This decrease is smaller than that proposed in [58], since even pumping well detuned from the energy E_{Th}, the condensate presents an extended and significant coherence.

Increasing the pump spot size to 40 μm, the same measurements are performed. At the parametric threshold, see Fig. 3.9(a), the interference is extended to the entire condensate, and the coherence map, see Fig. 3.9(b), reveals that the condensate's phase is locked across the entire area (as it was observed in the previous case). In this situation, one cannot extract a value for L_C since the condensate is extended to the whole pump spot and abruptly decays. This is shown again in more detail in Fig. 3.9(c), where a horizontal profile of the coherence map is represented. By decreasing the pump energy by $\delta E \equiv E_{Th} - E = 0.008\ meV$ towards lower energies, leaving fixed the pump power and angle, the phase-matching conditions for the OPO are not fulfilled anymore and an emission of thermally populated states is obtained at the bottom of the LPB. The interferometric analysis of the emission from the cloud of non-condensed polaritons gives an interference pattern with a high contrast of the interference fringes only at the center of the emission [Fig. 3.9(d)]. The corresponding coherence map [Fig. 3.9(e)] reveals a $\sim 7\ \mu m$ coherence length, extracted by fitting a Lorentzian function [Fig. 3.9(f)].

The fact that, for both cases 10 and 40 μm, the degree of coherence is almost flat along the entire condensate, when the conditions for the parametric threshold are satisfied, demonstrates that a single coherent mode is formed, in contrast with what has been found in previous works [69, 73] where disorder of the sample caused the development of several modes. In both situations, the extension of the coherence is limited by the pump spot size. Until now only in the work of Baas et al. [76] similar levels of extended spatial coherence in the OPO condensate have been reported, though without the complete quantitative map of $g^{(1)}$ presented here (the still longer coherence lengths observed in 1D microcavities [77] are associated with polaritons propagating outside the pumped region). It is worth to note that in an OPO process, the coherence properties of the signal are not inherited from the excitation

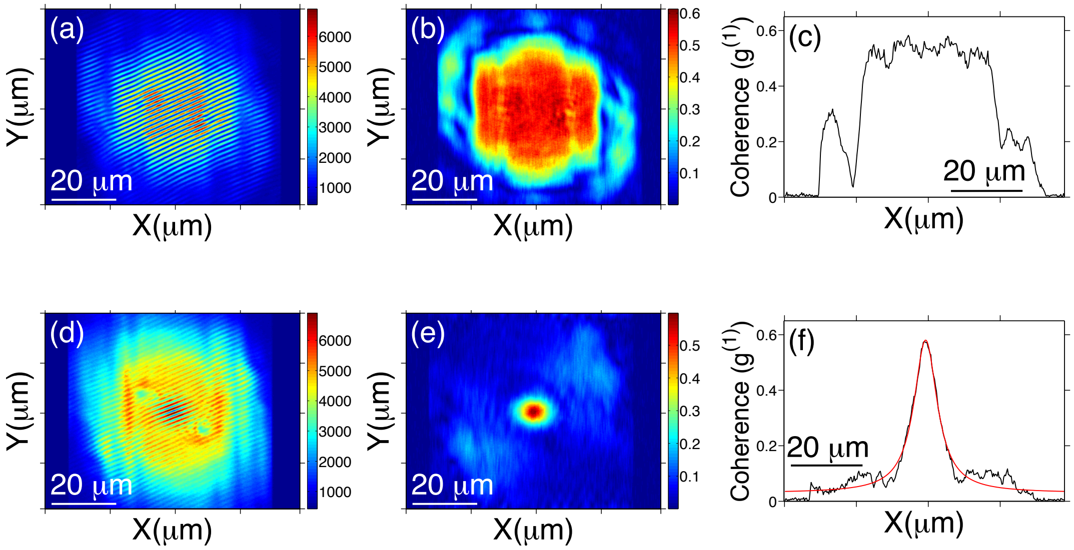

Figure 3.9: Interference pattern (a/d) and corresponding coherence (b/e) of the condensate generated at/below the parametric threshold, E_{Th}, corresponding to a pump energy $E_1 = 1552.57\ meV$/ $E_2 = 1552.56\ meV$ and power density P $= 15.8\ kW/cm^2$. Horizontal profiles at the center (c/f) showing the constant coherence along the entire condensate for E_1/an exponentially decaying one for E_2. The red line is the Lorentzian fit.

laser [53]. It is also important to note that although the theory of an infinite 2D condensate predicts the absence of long-range order, and a power-law decay of the spatial coherence [35] with a decay length inversely proportional to the particles's mass, in a finite dimension system such as the studied here, determined by the pump laser size, which is much smaller than the decay length, a constant coherence of the condensate can be obtained.

Figure 3.10 renders how the coherence length is affected by different values of δE, for each one of the two studied sizes. In Figure 3.10(a) it is observed that the condensate is very robust to changes of the pump energy, so the coherence length shows a smooth decay, even for a very large detuned energy of the excitation source, *e.g.* for $\delta E = 0.77\ meV$ the coherence length is about 9 μm, while at the parametric threshold, the coherence length is

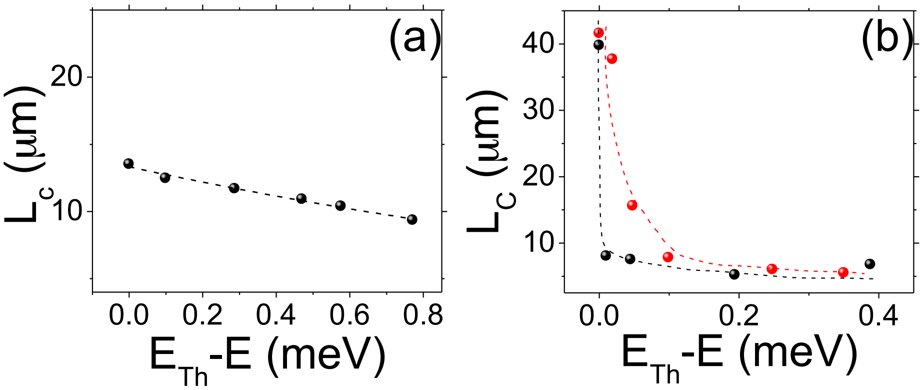

Figure 3.10: Coherence length L_c as a function of the energy distance from the threshold energy $\delta E \equiv E_{Th} - E$. (a) Depicts the case for the 10 μm spot size, where a smooth decay of the coherence length is observed. In (b) the case of 40 μm is presented, here the coherence length shows a pronounced decay, when δE is increased. Dashed lines are guides to the eye.

about 13 μm (this is a few micrometer wider than the spot size and is due to a diffusion of polaritons outside the pump spot). On the other hand, when the system is pumped by a spot size of 40 μm, for detunings as small as δE =10 μeV, the condensate is brought out of resonance, as in shown in Fig. 3.10(b): black points represent the typical behavior, where the coherence length falls from 40 μm, at the parametric threshold, to a value of about 7 μm. Red points in Fig. 3.10(b) present a different case where a less abrupt decay of the coherence length is observed for small δE, nonetheless, the behavior is similar for both cases presented in Fig 3.10(b).

The marked difference between Figs. 3.10(a) and 3.10(b) is mainly due to the fact that the range of k values used to pump the cavity increases with decreasing pump the size.

3.2 Coherence of coexisting 2D and 1D condensates

This section deals with the coherence properties of a hybrid system, where we exploit the presence of otherwise undesired defects in the sample. Most semiconductor microcavities exhibit different kinds of defects due to strain relaxation during the growth process, which originates from impurities or lattice constant mismatch of the different semiconductor layers.

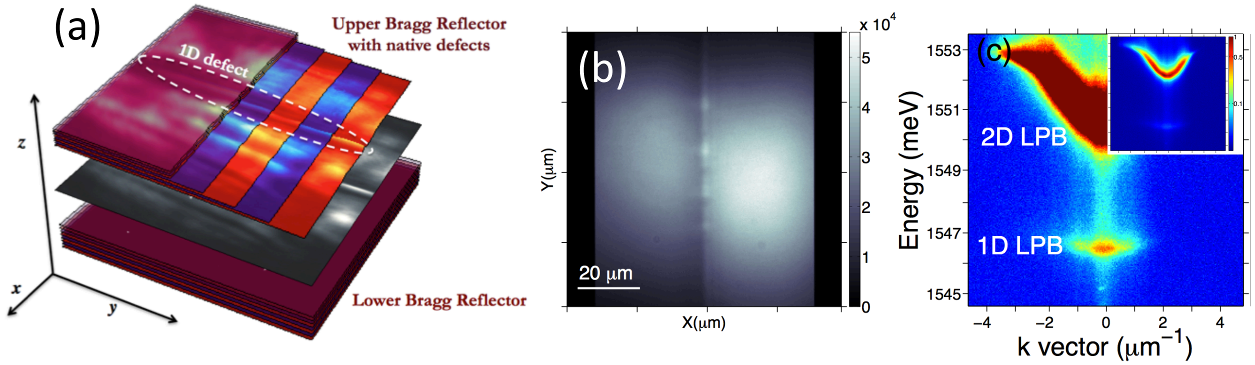

Figure 3.11: System under study. (a) Displays a schematic representation of the sample with a defect due to the imperfections of the top Bragg mirrors, developing along the y-direction, and resulting in the confinement along the x-direction. (b) Shows the PL for non-resonant excitation of the sample's region where the defect is present. In (c) the emission in momentum space is shown, the scale is saturated in order to better observe the emission. The inset displays the emission in a non-saturated logarithmic scale.

The latter is a typical phenomenon of the multilayer DBR structures and leads to cross-hatching [78], with 1D defects along the crystallographic axes. This is the plausible origin of the 1D defect we choose to investigate. Figure 3.11(a) depicts a schematic draw of the microcavity with a defect in the upper Bragg mirror. The defect presents an approximated width of 3 μm and length of 60 μm. Figure 3.11(b) shows an actual real space image, for non-resonant low power pumping, of the microcavity region where the defect is placed. Figure 3.11(c) presents momentum space emission (in a saturated scale) of the same region of the microcavity displayed in Fig. 3.11(b), where the 1D LPB is seen. The inset is the same momentum space image in a logarithmic non-saturated scale

In Ref. [58] a theoretical study of the coherence properties of a 1D OPO system is presented and it is found that the first order spatial correlation function is expected to decay rapidly along the condensate length even when pumping at the parametric threshold, E_{Th}. For atomic condensates, which are equilibrium systems, the theory developed in [35] for the 1D case predicts an exponential decay of the phase coherence. In the case of polariton condensates, which are rather out of equilibrium, the theory does not necessarily hold anymore. Such a non-trivial theoretical issue of coherence of OPO condensates generated in 1D systems has been further developed in a subsequent work of Wouters and Carusotto [79], who predicted the coherence behavior by means of numerical simulations. For the 1D system they found that the effects of long-wavelength fluctuations are expected to be stronger than those in the 2D case, being able to destroy the long-range order [35, 53]. For these systems, in the case of an ideal disorder-less scenario, they predict that the spatial coherence along the 1D condensate direction (y) decays with an exponential law: $g^{(1)}(y) \propto e^{-|y|/lc}$, with l_c being the coherence length, which they estimate to be of the order of a few hundreds of microns. The coherence degree of 1D condensates has also been addressed in a recent work of Malpuech and Solnyshkov [80], in which they take into account the presence of disorder; in this case they predict a fluctuating degree of coherence in space, with the maxima of coherence in correspondence to potential minima.

We carry out the study of coherence in two different cases: (a) generating the OPO in the 1D, pumping close to the inflection point of the 1D branch, and (b) generating the OPO in the 2D system, by phase-matching the 2D branch. The results of this procedure are depicted in Figs. 3.12(a)–(d), where, using a dove prism, we are able to record the OPO emission along two directions, parallel and orthogonal to the line defect. Figure 3.12(a) shows the emission of the 1D-OPO condensate generated by pumping at the inflection point of its LPB [case (a)], tuning the pump laser at $E_{Th} = 1551.1\ meV$ and with an average power $P = 0.07\ W$. The condensate emission coming from the direction k_x shows a flat dispersion due to the confinement along x. However, the emission coming from the direction k_y, parallel to the defect, exhibits a small curvature in its dispersion [see Fig. 3.12(b)]. The dramatic effect of excitonic interactions is witnessed by the strong blueshift experienced by the emission energy of the region enclosed by line defect, of the order of $E = 3.3\ meV$. Tuning the laser toward high energies and increasing the pump power from $P = 0.07\ W$ to $P = 0.1\ W$, we phase-match the 2D system at $E_{Th} = 1551.6\ meV$ [case (b)] achieving an OPO condensate as depicted in Fig. 3.12(c) for emission collected orthogonally to the line defect and in Fig. 3.12(d) for parallel collection. In this case, the blueshift for the LPB of the 2D condensate is only $E = 0.4\ meV$, much lower than that of the 1D case, but the 1D system still experiences the same strong blueshift and shows a very narrow emission as when it was resonantly pumped, indicating that the line defect is still massively occupied and the condensation is still present.

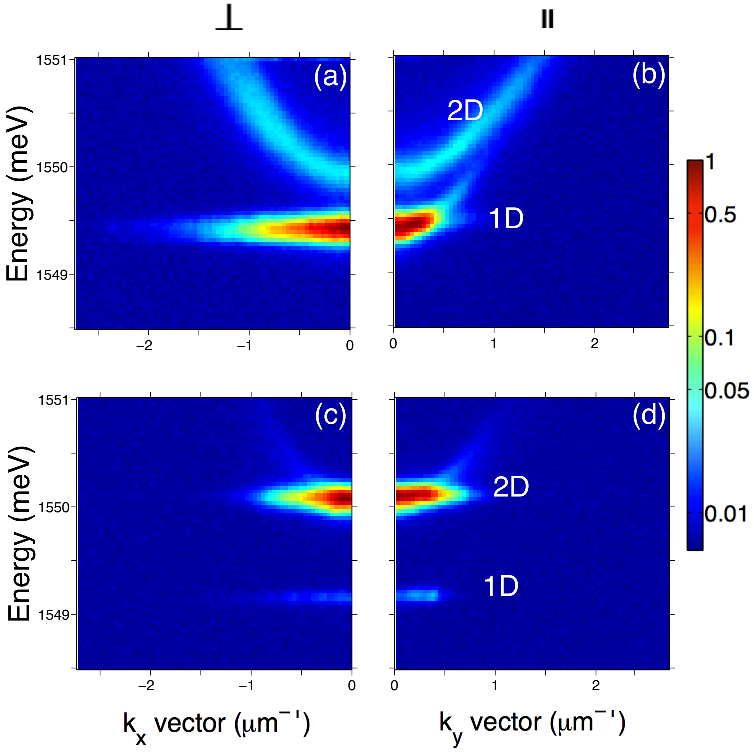

Figure 3.12: k-space OPO emission from the orthogonal (a) and parallel (b) directions to the line defect when phase-matching the line defect at $E_{Th} = 1551.1\ meV$ at the average pump power $P = 0.07\ W$. The 1D emission shows a blueshift of $E = 3.3\ meV$ when the OPO takes place. (c, d) Emission from the orthogonal and parallel directions to the defect, respectively, for the case of the OPO achieved by phase-matching the 2D LPB. The pump laser is tuned at $E_{Th} = 1551.6\ meV$ at a power $P = 0.1\ W$. Both the 2D and 1D energy levels experience a blueshift of $E = 0.4\ meV$ and $E = 3.2\ meV$, respectively, indicating that in this case the 2D and 1D systems are massively occupied.

Figures 3.13(a) and 3.13(d) display the real space emission counterparts of the two cases presented in Fig. 3.12. When we phase-match only the line defect energy dispersion, a bright emission is collected only from the defect area [Fig. 3.13(a)]. In order to extract the coherence of the 1D condensate, we used the procedure detailed in § 2.4. This time, when the phase-matching conditions allow to generate parametric scattering only in the 1D system, the interference pattern is present only in the wire-like region [Fig. 3.13(b)]. The corresponding coherence map presents a maximum degree of coherence of 0.5 at the center of the condensate, and decaying along the axis of the defect, with a modulation ascribable to the fluctuations of the potential landscape [see Fig. 3.13(c)].

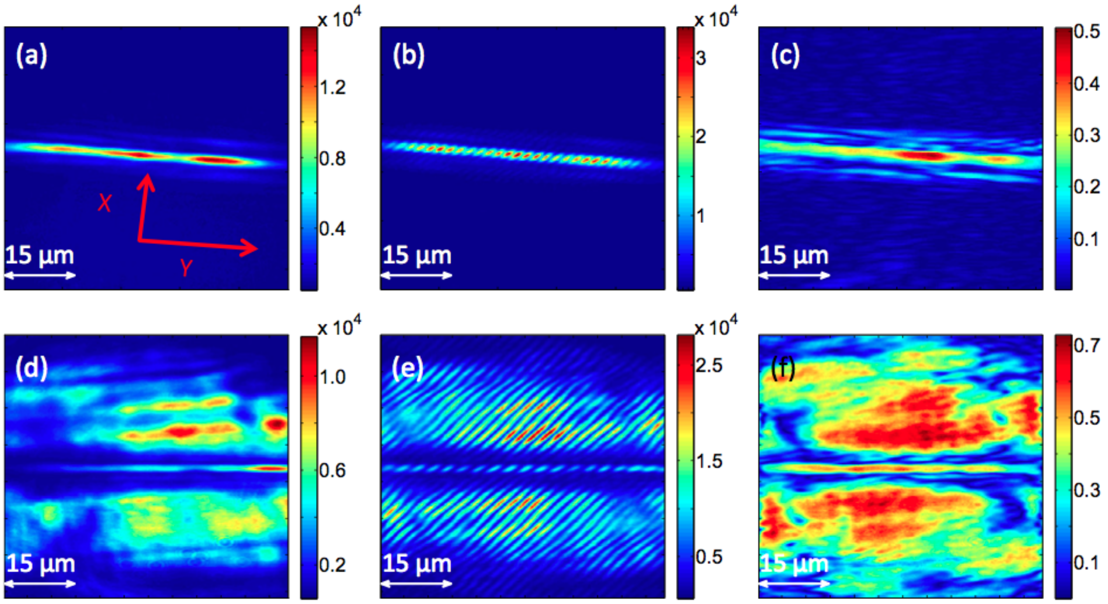

Figure 3.13: (a) Real space emission from the line defect condensate, the corresponding interference pattern (b) and coherence map (c) when phase-matching the line defect at $E_{Th} = 1551.1\ meV$ and $P = 0.07\ W$. (d) Real space emission from the line defect condensate along with the 2D condensate emission; a dark region of 6 μm separates the 2D and the 1D emission; the corresponding interference (e) and coherence map (f) when phase-matching the 2D emission at $E_{Th} = 1551.6\ meV$ and $P = 0.1\ W$.

To better visualize the spatial decay of the coherence, we present a cross-section of the coherence map [Fig. 3.14(a)], which demonstrates a fast decay of coherence along the defect direction dropping from the maximum value of 0.5 at the center to 0.25 at a distance of only 10 μm. This result agrees qualitatively with the prediction of a decaying coherence in 1D systems presented in Refs. [58, 79]. From these data it is not possible to extract the predicted decay law, because the coherence is modulated by the disorder of the sample. In fact, the reduced dimensionality makes the coherence more sensitive to the effects of sample disorder. A similar modulation of the spatial coherence along a line has already been observed for condensates created by non-resonant pumping in $CdTe$ microcavities by Manni et al. [81],

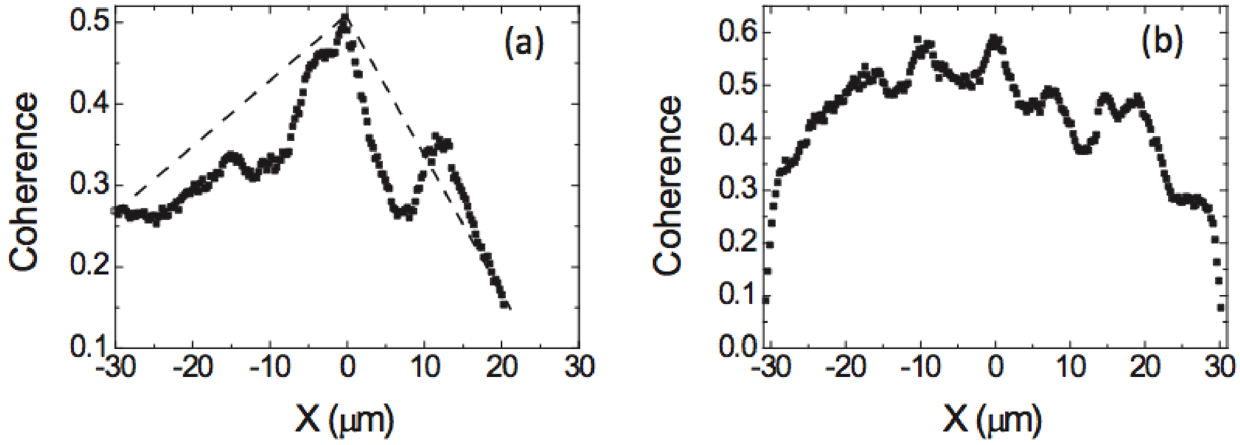

Figure 3.14: Horizontal slice of the coherence map of the line defect presented in Fig. 3.13(c), showing a fast spatial decay modulated by the sample inhomogeneities (the dashed line is a guide for the eye). (d) Horizontal slice of the coherence map of the line defect presented in Fig. 3.13(e), where higher degree of coherence and longer coherence length are reached, and with less dramatic effects of the sample inhomogeneities.

who attributed the effect to disorder. It is worth mentioning that a very high and extended spatial coherence, lasting up to hundreds of microns, has been demonstrated in 1D systems by Wertz et al [77]. The observation of such coherence has been possible thanks to two main factors, *i.e.* the extremely high quality of the sample and the fact that they study, unlike us, propagating condensates which preserve their original spontaneous coherence during the propagation along the wire.

On the other hand, when the 2D system is phase-matched, we observe in real space the coexistence of the emission from both the 2D and the line defect as shown in Fig. 3.13(d), with a dark region of about 6 μm separating them. The interference pattern presented in Fig. 3.13(e) reveals a higher contrast in the 2D region than that in the line defect region. It is worth noting that the fringes corresponding to the upper and the lower 2D part have the same orientation and periodicity, which indicates that the same phase is obtained in the two split 2D condensates, while the central region, where the line defect is located, presents fringes with a slightly different periodicity with respect to that of the 2D, which could be given by a different angle of emission. The coherence map presented in Fig. 3.13(f) reveals

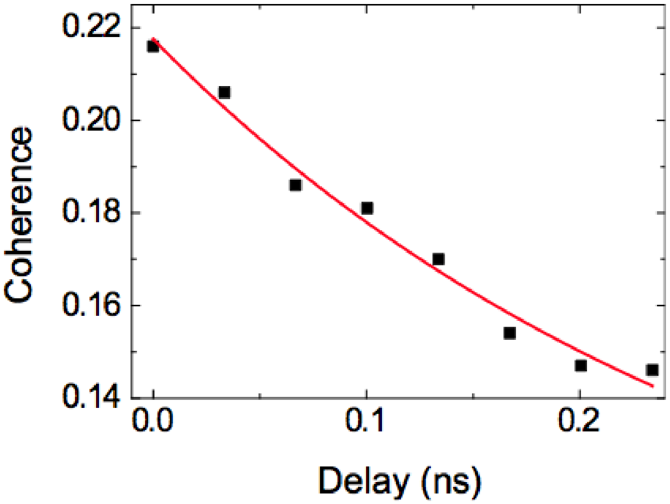

Figure 3.15: Temporal coherence decay of the line defect condensate when phase-matching the 1D system at $E_{Th} = 1551.1\ meV$. Each point of the curve corresponds to an average of points around the center of the line defect. A coherence decay time of $\tau_c = 280\ ps$ is extracted from fitting the experimental data with a exponential function.

quite a large coherence modulated by the sample disorder in a less pronounced way than that observed for 1D phase-matching conditions. This is well evidenced in Fig. 3.14(b), where the horizontal profile of the coherence map of the line defect is shown. Under these conditions we observe an increase in the coherence length of the line defect as well; in this case two condensates coexist: one related to the 2D system created by parametric scattering and the other in the defect created by a sort of migration of polaritons from the 2D condensate toward the line defect, energetically favored by the lower energy of the 1D system.

It is well known that excitonic interactions lead to fluctuations in the number of particles in the condensate, and that these fluctuations, broadening the energy of the emission, are responsible for a faster decay of the coherence [64]. To test the effect of interactions in the 1D system, we have also measured the temporal decay of the coherence when the OPO condensate is created only in the quasi-1D system. For this purpose we use the method described in § 2.4, this time measuring $g^{(1)}$ at a given point for different time delays τ, $g^{(1)}(\tau) = \left(\frac{\langle E^*(t)E(t+\tau)\rangle}{\langle E^*(t)\rangle\langle E(t)\rangle}\right)$, which permits the evaluation of the signal temporal coherence. In this manner, we obtain $g^{(1)}$ from zero up to a maximum delay of ~0.3 ns. A typical result of the temporal behavior of the coherence is presented in Fig. 3.15, where an exponentially decaying coherence is found. A fit of the data obtains a decay time of $\tau_c = 280\ ps$, which is a long time compared to the polariton lifetime, but is almost an order of magnitude lower than the best value found in § 3.1.2 for 2D OPO polariton condensates. We suggest that, as in the 2D case, this coherence time is limited by the interactions in the system. However, converting it into a coherence length using the polariton mass would give a coherence length of the order of 100 μm, of the same order as those calculated in [79], but much longer than the coherence decay seen in Fig. 3.14(a). Thus, we propose that disorder is the dominant factor limiting the coherence decay in our experiments on 1D systems.

3.3 Summary

In this chapter we have presented a study of the coherence properties, both spatial and temporal, of polaritons condensate in the OPO regime. The spatial coherence was investigated below and at the OPO condensation threshold, obtaining a very large coherence length for 2D $GaAs$ microcavity polaritons. Measurements of the temporal coherence reveal a predominantly exponential decay caused by polariton-polariton interactions in a motional narrowing regime. Although similar to the exponential decay associated with the Schawlow-Townes linewidth, the mechanism is different, and gives a different dependence of coherence time on condensate area. By varying the area of the condensate and comparing with scaling laws, we observe that the dephasing time follows the predictions of the coherence theory of polariton condensates. Constructing condensates of large area, we are able to achieve long coherence times, which is a crucial step forward for exploiting polariton condensates in quantum and ultrafast devices.

On the other hand, for an isolated 1D condensate we find that the coherence decays rapidly over length scales much smaller than our spot size. We also find a coherence time one order of magnitude smaller than that of a 2D condensate created in the same sample. Such a behavior may reflect the increasing importance of fluctuations as the dimensionality is reduced. However, some of the effects may be also related to changes in the effective disorder strength.

Chapter 4

Polarization properties of OPO condensates

In this chapter we report on the polarization properties of the polariton condensate. The study is focused in the peculiar system described in § 3.2 where the coexistence of a 2D and 1D condensate allows us to investigate and compare the polarization behavior of the OPO process in microcavity exciton-polaritons [82]. Polaritons present an one-to-one correspondence between the polarization of the emitted photon and the polariton pseudospin, this allows to obtain the polariton spin by directly measuring the polarization of light.

The rich spin dependent phenomena offered by exciton polaritons, especially the phenomena found in the parametric scattering, make them a suitable system in order to develop optical spin devices.

4.1 Polarization behavior of the OPO process

Polaritons are promising candidates for novel optical devices due to their spin structure, consisting in two spin with opposite projections on the structure growth axis. Their spin dynamics was studied for non-resonant pumping [16], where a sign reversal of the circular degree of polarization was found; the reversal is related with the sign of the splitting between the energies of the σ^+/σ^- polarized components of the PL. The spin of the lowest energy state changes from +1, for positive cavity-exciton detuning, to -1 for negative cavity-exciton detuning; the results were modeled in the framework of a quantum theory describing the momentum and spin relaxation by Kavokin *et al.* [83]. On the other hand, for the parametric scattering process in the OPA configuration, mechanisms for scattering between polaritons with opposite spin were observed, moreover spin-flip was found for linearly polarized pump together with the amplification of a σ^+ probe beam [19, 20, 84].

Other spin dependent phenomena have been proposed and demonstrated experimentally: spin switches [85], whose results resemble the findings of Ref. [19], where a localized probe (σ^+ or σ^-) switches on a large emission of a pump controlling its polarization; the optical spin Hall effect proposed by Kavokin *et al.* [86] was experimentally achieved in Ref. [87] and a similar non-linear effect was observed in Ref. [88]; polarization pattern formation in real space with high degree of circular polarization was proposed in Ref. [89], and independently experimentally observed in Refs. [90, 91]. Moreover, for possible future devices that might exploit spin properties, room temperature operation is a further requirement. In this context, polariton lasing has been achieved in GaN-based microcavities [92].

Let us start here by reviewing the aspects related with the rotation of the polarization of the emission with respect to that of the excitation laser. This is the main result found in our study, where we have done a full study of the polarization properties of the emitted light from of the OPO signal as a function of the angle of the linear polarization of the excitation. An inversion of the linear polarization (∼90° rotation) of the 2D-OPO signal with respect to the polarization of the pump has been reported previously [84]. This was explained in terms of the negative ratio of the scattering cross-sections of polaritons with opposite and parallel spins, which are dominated by exchange interaction. Rotation of the linear polarization as well as conversion from linear to circular polarization have been observed in Ref. [93]. These results were modeled taking into account the self-induced Larmor precession (due to the splitting between spin-up and spin-down polaritons and polariton-polariton interactions) and the additional splitting, caused by the TE-TM splitting of excitons with dipole momentum aligned along and perpendicular to the wavevector and the different reflectivities of the microcavity for the TE and TM polarization (both dependent on the in-plane wavevector). In 1D-microcavities, an inversion of the linear polarization of the signal and idler with respect to that of the pump, in inter-band parametric scattering processes, has been reported, [94, 95] but only for particularly selected polarization conditions of the excitation.

The TE-TM splitting has been reported in Refs. [16, 96, 97], amounting to $\sim$100 μeV, this value supports a key hypothesis made usually in the literature to theoretically describe these phenomena, that the splitting between polarized eigenmodes is small. Two polarization eigenstates are modeled as a single state of given energy subject to an effective magnetic field, which induces rotation of the polariton pseudo-spin. This approach neglects that the scattering rates toward the split states are slightly different, and in fact the description breaks down if the polarization splitting is large. This is in general the case in 1D systems, where the splitting between longitudinal and transverse modes is comparable with the splitting between different confined modes.

In this chapter, we present a full study of the polarization properties of the light emitted from coexisting 2D and 1D polariton condensates in a $GaAs$-based microcavity pumped in the conventional intra-band OPO regime, as a function of the angle of the linear polarization of the excitation. Our experiments confirm the previously reported results for the 2D case, however, by reducing the dimensionality of the system from 2D to 1D, the polarization properties are strongly modified. In the latter case by rotating the polarization plane of the pump beam, we observe an abrupt switching behavior of the OPO condensate emission between two highly linearly polarized states. Interestingly, the switching between these states occurs with the double frequency of that of the rotation of the pump's polarization plane. In collaboration with the group of Prof. G. Malpuech, we have developed an extension of the existing spin-dependent semi-classical Boltzmann kinetic equations, taking explicitly into account the large polarization splitting value, which fits excellently the experimental data. Real space simulations done with Gross-Pitaevskii equations also confirm our interpretation of the experiments.

4.2 Polarization exciting the 2D system

In section § 3.2 we presented the coherence properties of a hybrid system found in the microcavity studied in this thesis; in this section, we investigate the polarization properties of the same system, when the phase-matching conditions are set for the 2D branch. The experimental setup is described in § 2.5 and here we choose the pump power to be 164 mW, well above the threshold $P_{th} = 76\ mW$, the temperature is kept at 10 K, and the spot size is $\sim 40\ \mu m$, under these conditions two condensates are formed at the lowest sub-bands, $E^{1D} = 1549.5\ meV$ and $E^{2D} = 1550.2\ meV$, respectively. In Fig. 4.1(a) the real space emission, integrated in energy, of an area around the defect is shown for excitation in the OPO configuration using the appropriate phase-matching conditions. The system is pumped $\sim$1.7 meV above the bottom of the 2D-LPB with an excitation energy of 1551.9 meV and an in-plane wavevector of $k_x \sim 2.0\ \mu m^{-1}$, corresponding to a pump angle of 14.7°. Figures 4.1(b) and 4.1(c) show the energy-momentum dispersion along the k_y and k_x directions, respectively. For the momentum space imaging, we use a telescope, with a slit in the real space plane, to filter spatially, reducing the collection area, the emission from the 2D area (otherwise the emission from the 2D condensate would completely hide any feature of the emission from the 1D condensate). More details about the procedure to obtain the momentum space images are given in § 4.3. In order to obtain Fig. 4.1(b) the slit in the telescope has been set in such a way that the intensities of the 2D and 1D condensates are similar and the dispersion characteristics can be compared simultaneously. One can infer by inspection of the dispersion relations images that, there are emission from non-condensed region (soft blue color) coexisting within the same spatial region with a condensed. In the k_y direction, parallel to the wire [Fig. 4.1(b)], two dispersions are clearly observed, an energetically lower and another higher one corresponding to the LPBs of the 1D and 2D system, respectively. Strong emission located in momentum-space at the bottom of the LPBs at $k = 0$ indicates that phase-matching conditions are sufficiently fulfilled for both the 1D and 2D systems. Figure 4.1(c) shows the dispersion along the k_x direction, perpendicular to the wire. The additional confinement in this direction leads to a further quantization of the microcavity states [77, 98] and in particular to a flat polariton dispersion in the direction normal to the wire at the lowest energy.

It is worth to notice that, the angle (or, equivalently, the corresponding k-value) of the excitation cannot be extracted from the momentum space images [Figs. 4.1(b) and 4.1(c)]. What is seen there at 1551.9 meV is reflected plus scattered laser light. The component of the wave-vector parallel to the wire is basically negligible. Furthermore, in order to keep the experimental realization of the OPO configuration as simple as possible, the experiments are restricted to the most symmetric situation, *i.e.* keeping the plane of incidence normal to the

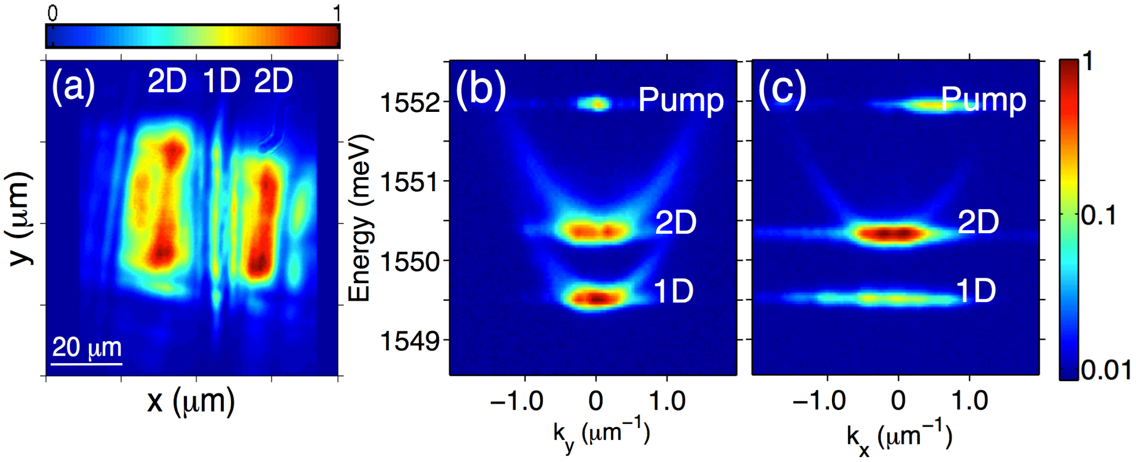

Figure 4.1: Real space emission and polariton dispersion for 2D phase-matching conditions. In (a) the normalized real space emission, integrated in energy, is shown in a region of the sample where the planar cavity is split by a line defect in a linear false-color scale. (b) shows the dispersion taken along the axis of the 1D system. Here both systems show nonlinear emission from the bottom of their respective branch coexisting with non-condensed polaritons. In (c) the dispersion is normal to the 1D system: marked difference are seen, the 1D system shows no dispersion, both for the condensed and non-condensed polaritons, while the 2D remains the same as in the previous case. A logarithmic scale is used for (b) and (c).

axis of the wire ($k_y = 0$). If the plane of incidence would not be normal to the axis wire, one would be changing the OPO configuration and simultaneously more complicated polarization selection rules would apply.

The emission in the area of the spot shows two rather rectangular shaped 2D condensates, with an 1D wire condensate vertically aligned in-between them. The particular rectangular shape and lines of the emission support the idea of strong cross-hatching due to DBR strain relaxation, as it was pointed out in § 3.2. The long-range coherence properties of this system have been presented in Chapter 3 and confirm the presence of a macroscopic quantum condensate.

In § 2.5 the procedure to analyze the emitted light in its polarized components, in order to obtain the Stokes parameters, was described. In Fig. 4.2 we show the polarized emission decomposed in the six main components: four linear components (in the horizontal/vertical and the diagonal/anti diagonal basis) and the circular ones, for a laser's linear polarization oriented perpendicularly to the axis of the defect. This orientation of the laser's polarization plane, is chosen to be the horizontal axis in the Poincare sphere [see Fig. 1.8] so that the degree of linear polarization (DLP) of the laser results in a positive value, calculated according to $DLP = (I_H - I_V)/(I_H + I_V)$.

Figure 4.2(a) depicts a map of the polarized emission in the horizontal direction, which shows light mainly emitted by the wire. The polarized emission in the vertical direction is depicted in Fig. 4.2(b), this reveals emission from the 2D. Figure 4.2(c) represents the S_1 component of the Stokes vector, *i.e.* the DLP in the H/V basis. In the second row, the emission polarized along the diagonal and anti-diagonal directions are presented in Figs. 4.2(d) and 4.2(e), respectively, and the S_2 component of the Stokes vector is shown in Fig. 4.2(f). The circularly polarized emission is shown in Figs. 4.2(g) and 4.2(h) which corresponds to the σ^+ and σ^- -polarized emitted light, respectively; the degree of circular polarization is extracted from these two maps and the result is compiled in Fig. 4.2(i). As one can see from the Stokes parameters, the S_1 component shows a high degree of polarization in both the 2D and 1D besides of marked difference in their orientation. The other two components of the Stokes vector show a rather low degree of polarization and therefore no significant differences between the 2D and the 1D system can be appreciated.

As clearly observed in Fig. 4.2(a), there is a markedly different behavior in the S_1 component for the 2D and 1D system, therefore we investigate in detail the DLP in the H/V basis as a function of the angle, θ_P, of the linear polarization of the laser. Polarization maps for the DLP corresponding to the S_1 component are shown in Fig. 4.3 for different θ_P: $\theta_P = 0$ (normal to the wire), $\theta_P = 20°$, $\theta_P = 45°$ (diagonal) and $\theta_P = 90°$ (parallel to the wire). In Fig. 4.3(a) the pump polarization is aligned perpendicularly to the wire and it is observed that the polarization of the 2D polaritonic emission is rotated by 90° with respect to that of the pump laser (blue colors). However, the polarization of the light emitted from the wire coincides with that of the pump polarization (red colors). In Fig. 4.3(b), for $\theta_P = 20°$, the 2D emission shows a slight decrease in the DLP, while the DLP of the 1D system becomes nearly zero. Figure 4.3(c) corresponds to the diagonally polarized excitation: now the DLP of the 2D emission vanishes, whereas in the 1D system a high negative DLP is observed. Finally, when the system is excited with polarization parallel to the wire (Fig. 4.3(d), $\theta_P = 90°$), both polarizations of the 1D and 2D emissions are rotated by 90° with respect to that of the pump

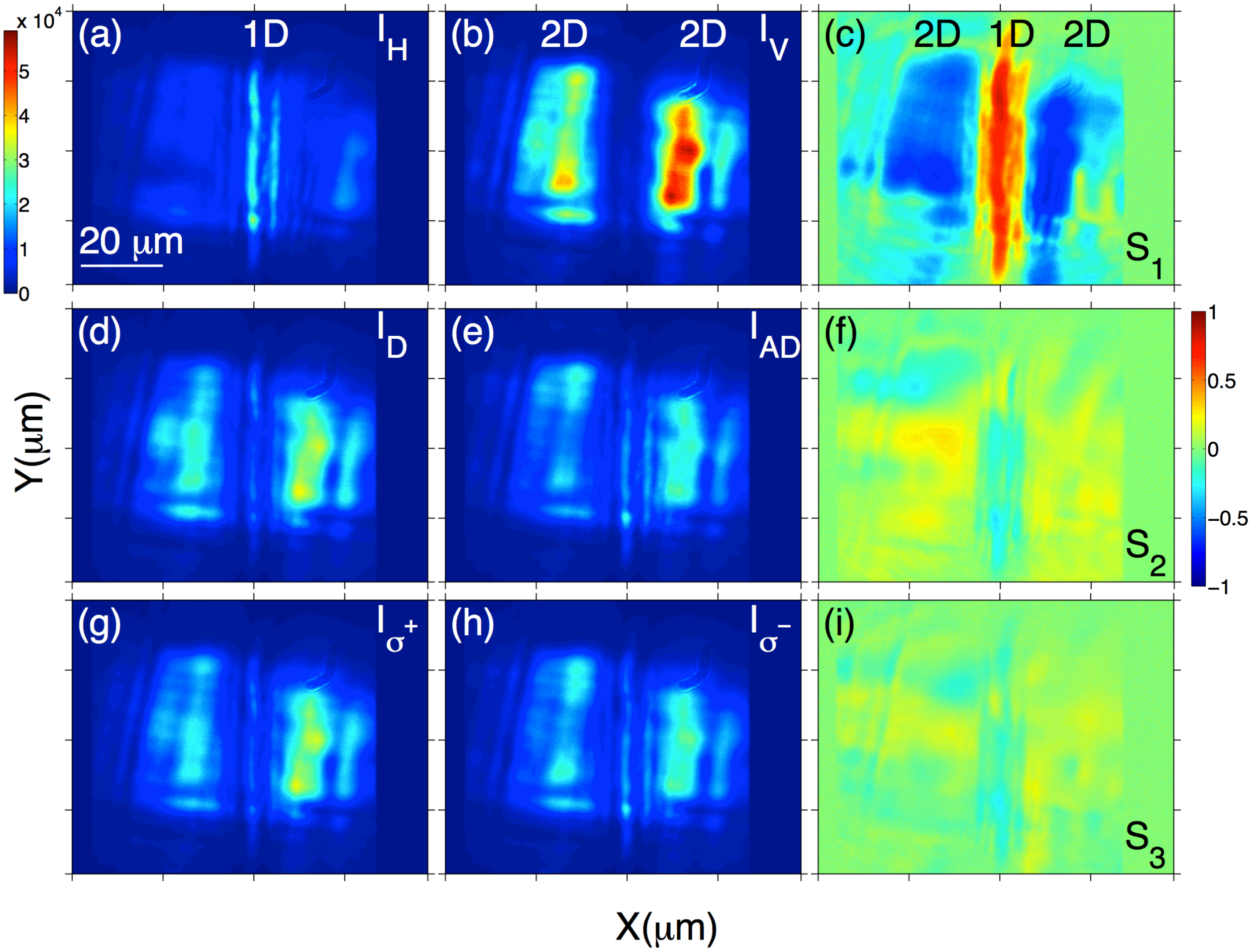

Figure 4.2: Polarized emission. (a)/(b) depicts the polarized emission in the horizontal/vertical direction. In (c) the corresponding false-color intensity map for the emitted light in the S_1 component is shown. The second row (d)/(e) shows the light emitted in the diagonal/antidiagonal direction. (f) depicts the Stokes parameter calculated in the diagonal basis. In (g)/(h) is presented the emission in the right/left handed circularly polarized basis. (i) shows the S_3 component, which is the degree of circular polarization. In (c) a high degree of polarization is seen in both systems, moreover a marked difference is observed between them, the 2D system presents a polarized emission vertical direction (rotated with respect to the laser's polarization), on the other hand the 1D system shows polarized emission with the same polarization of the laser. The S_2 and the S_3 components depict a rather small degree of polarization and significant differences are appreciated neither in the S_2 nor S_3 components.

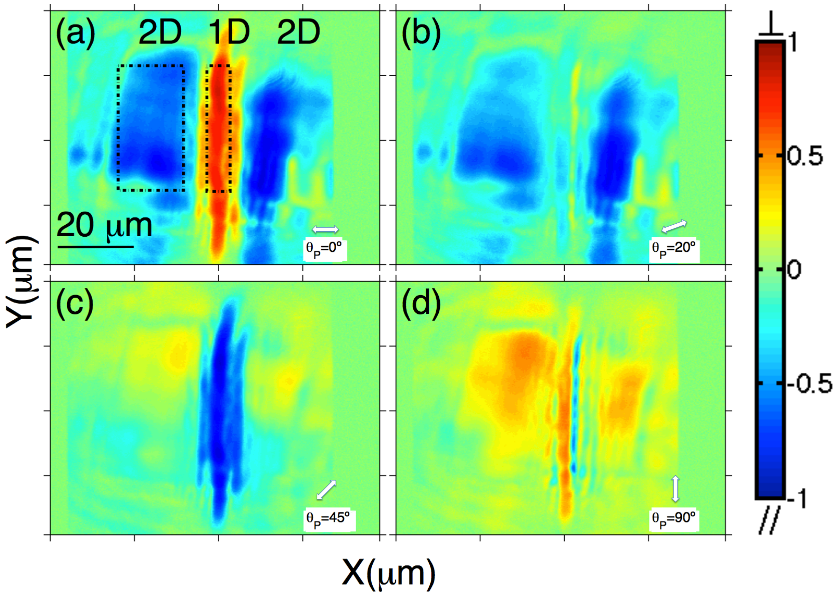

Figure 4.3: S_1 Stokes component for selected values of θ_P. The arrows depict the plane of the pump's polarization. In (a), $\theta_P = 0$, the polarization of the emission from the 2D system is opposite to that of the laser, while the 1D condensate keeps the same polarization of the pump. In (b), $\theta_P = 20°$, the DPL of the 2D condensate decreases and that of the 1D system vanishes. In (c), $\theta_P = 45°$, the 2D condensate exhibits a negligible DLP, while the 1D emission is highly polarized parallel to the wire. In (c), $\theta_P = 90°$, both condensates show an inversion of the polarization plane with respect to that of the laser. Dashed boxes show the area of integration, used to obtain the curves in Fig. 4.7.

laser.

For the sake of completeness, the polarization properties were also studied for elliptically polarized pump laser, in Figs. 4.4(a)-(c) the Stokes components for a pump ellipticity ($e = -1$) are shown, here inversion is neither observed for the 2D nor 1D condensate, *i.e.* the emission of the signal state is completely driven by the laser, as in Ref. [19]. When the ellipticity of the pump is null ($e = 0$), it corresponds to horizontally linearly polarization, Figs. 4.4(d)-(f) depict similar polarization maps as those shown Fig. 4.2.

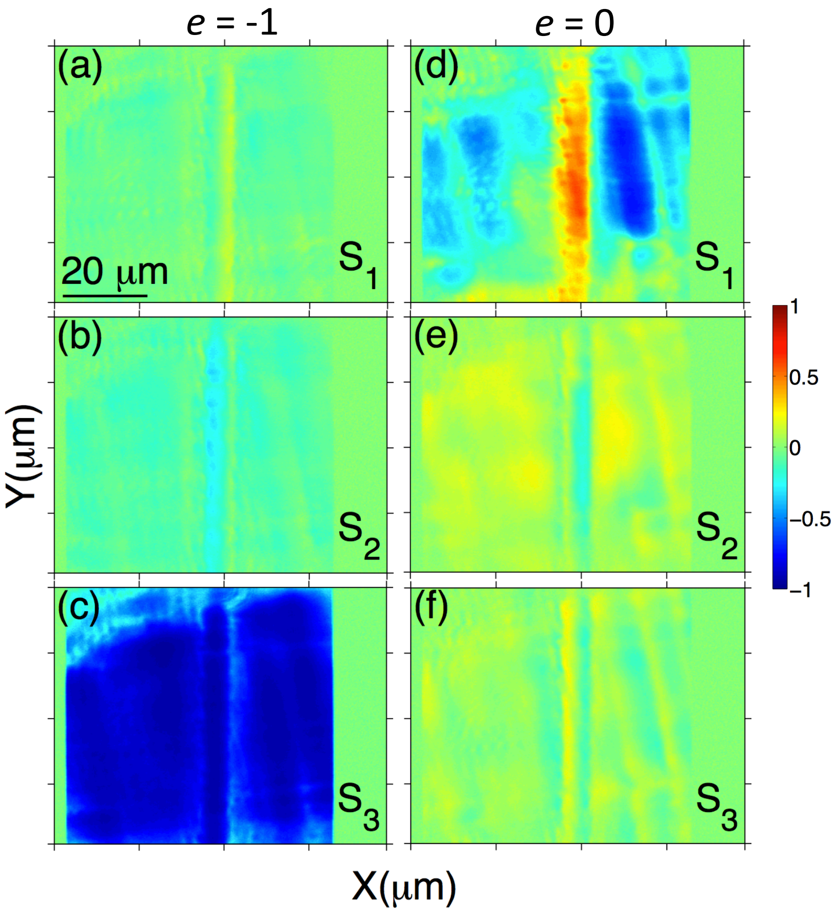

Figure 4.4: Stokes parameters for elliptically polarized pump. (a)-(c) Show the case for $e = -1$, where the dominant component is the S_3. Figures (d)-(f) are the Stokes parameters for $e = 0$.

4.3 Polarization exciting the 1D system

As it was shown in § 3.2, it is possible to selectively generate only the 1D condensate by fine-adjusting the excitation to the phase-matching conditions of the wire, *i.e.* lowering the excitation energy to $E = 1550.8\ meV$ and choosing an in-plane wavevector of $k_x \sim 1.55\ \mu m^{-1}$, corresponding to a pump angle of 11.4°, as demonstrated in the real space image in Fig. 4.5(a). Now, only the emission of the 1D wire is observed, while no condensation occurs in 2D.

Figures 4.5(b) and 4.5(c) show the polariton dispersion parallel and perpendicular to the wire, respectively, and confirm the presence of a wire condensate at $k = 0$ and the absence of the 2D condensate. Note, that the excitation energy is still well above the 2D condensate energy, as observed in Fig. 4.1, and also above the LPB, but the strict 2D phase-matching conditions impede the formation of the 2D OPO.

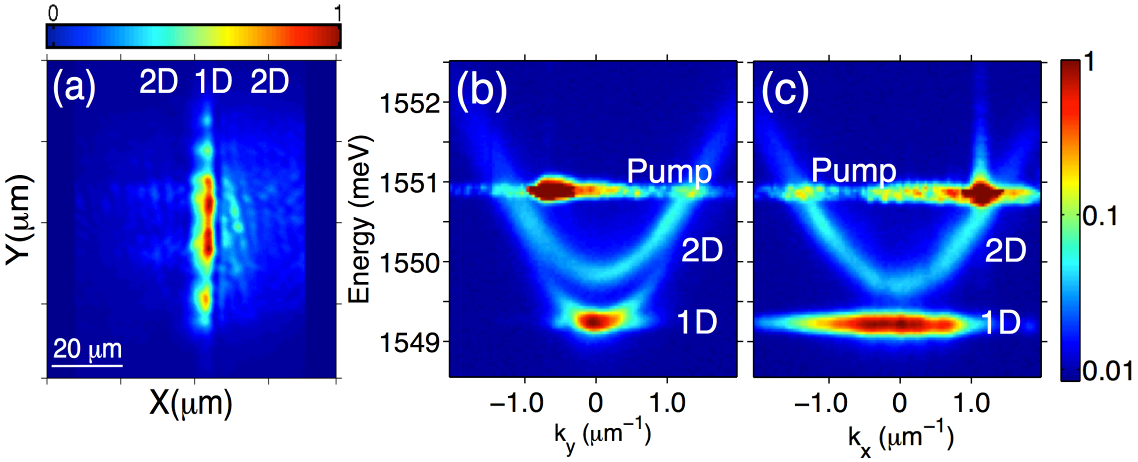

Figure 4.5: Real space emission, and polariton dispersion for 1D phase-matching conditions. In (a) the normalized real space emission, integrated in energy, at the same region as in Fig. 4.1, is shown in a linear false-color scale, but now there is only significant emission from the 1D condensate. (b) Dispersion taken along the axis of the 1D system. Here the 2D polariton dispersion does not show condensation, whereas in the 1D system nonlinear emission is found; besides, the presence of the quasi-parabolic dispersion in the 1D system indicates coexistence of non-condensed and condensed polaritons. In (c) the dispersion is normal to the 1D system: marked difference are seen, the 1D system shows no dispersion while the 2D remains basically the same. A logarithmic scale is used for (b) and (c).

One should note that the main purpose of the momentum space images, shown in the Figs. 4.1(b), 4.1(c), 4.5(b) and 4.5(c) is to visualize the dispersion relations of the 1D and 2D system for different directions. A quantitative analysis of the results shown in these figures is neither needed nor performed for our studies. Slightly different alignment of the imaging optics produces differences between Figs. 4.1(b) and 4.1(c) regarding intensities, energy shifts and dispersion curvatures. The same effect is observed comparing Figs. 4.5(b) and 4.5(c). The larger energy-blueshifts seen in Figs. 4.1(b) and 4.1(c) as compared to those in Figs. 4.5(b) and

4.5(c) arise from differences in the occupancy of the different states. The higher density of 2D polaritons, and consequently the increased polariton-polariton interactions in the condensed phase [Figs. 4.1(b) and 4.1(c)], leads to a blueshift of $\sim$0.5 meV for the 2D system with respect to the noncondensed situation [Figs. 4.5(b) and 4.5(c)]. For the same reason, the condensed 1D polariton state shifts also to higher energies, although by a smaller amount.

Turning back again to the polarization properties, in Fig. 4.3, where the phase-matching conditions were set for the 2D branch, the 1D system showed a different evolution of the S_1 component with respect to the 2D system as the angle θ_P was varied. In Fig. 4.6 we present polarization maps for the same selected values as in Fig. 4.3, when the phase-matching conditions are now set for the 1D branch.

The orientation, θ_P, of the linearly polarized excitation varies for the four panels: $\theta_P = 0$ (normal to the wire), $\theta_P = 20°$, $\theta_P = 45°$ (diagonal) and $\theta_P = 90°$ (parallel to the wire). The results found are qualitatively the same as those obtained in the previous section: in Fig. 4.6(a) the pump polarization is aligned perpendicularly to the wire and it is observed that the polarization of the light emitted from the wire coincides with that of the pump polarization (red colors). In Fig. 4.6(b), for $\theta_P = 20°$, the DLP of the 1D system becomes nearly zero. Figure 4.6(c) corresponds to the diagonally polarized excitation: now in the 1D system a high negative DLP is observed. Finally, when the system is excited with polarization parallel to the wire (Fig. 4.6(d), $\theta_P = 90°$), the polarization of the 1D emissions is rotated by 90° with respect to that of the pump laser.

Looking into the details of the DLP patterns shown in Figs. 4.3 and 4.6 , a fine structure is observed in the region of the wire, which was not further studied since we were only interested in the overall DLP behavior as a function of the laser polarization plane. However, the resolution of this fine structure demonstrates the power of polarization-resolved emission studies compared to regular photoluminescence ones (see Figs. 4.1(a) and 4.5(a), where this fine structure is not resolved).

4.4 Differences between the 2D and 1D systems

Here we compare the main results obtained for the DLP as the laser's polarization plane is rotated, Figure 4.7 compiles the emission DLP as a function of θ_P in more detail. These data

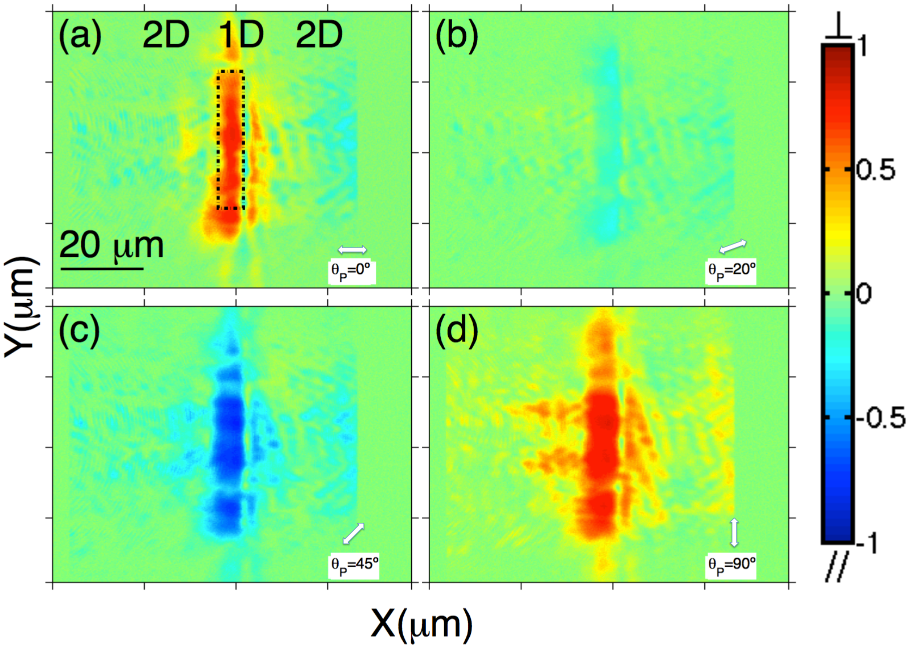

Figure 4.6: S_1 Stokes component for selected values of θ_P. The arrows depict the plane of the pump's polarization. In (a), $\theta_P = 0$, the polarization of the emission from the 1D condensate keeps the same polarization of the pump. In (b), $\theta_P = 20°$, the DPL of the 1D system vanishes. In (c), $\theta_P = 45°$, the 1D emission is highly polarized parallel to the wire. In (c), $\theta_P = 90°$, the condensate shows an inversion of the polarization plane with respect to that of the laser. Dash box shows the area of integration, used to obtain the curves in Fig. 4.3.

are obtained by integration and normalization of areas in the DLP maps that are depicted as dashed boxes in Figs. 4.3(a) and 4.6(a). Figures 4.7(a) and 4.7(b) show the results discussed above for 2D phase-matching conditions, while Fig. 4.7(c) corresponds to 1D phase-matching conditions.

Analysis of the 2D-case: For the 2D condensate, Fig. 4.7(a), it is observed that the DLP changes, in a sinusoidal-like fashion, between -0.5 and 0.4, when varying the pump polarization angle θ_P. In particular, for perpendicular ($\perp$) and parallel ($\|$) polarized excitation with respect to the wire, the emission polarization is rotated by $\sim 90°$. Linear polarization inversion is a typical behavior of microcavity polariton systems, which has been previously observed experimentally [93] and explained theoretically [84] in terms of polariton-polariton

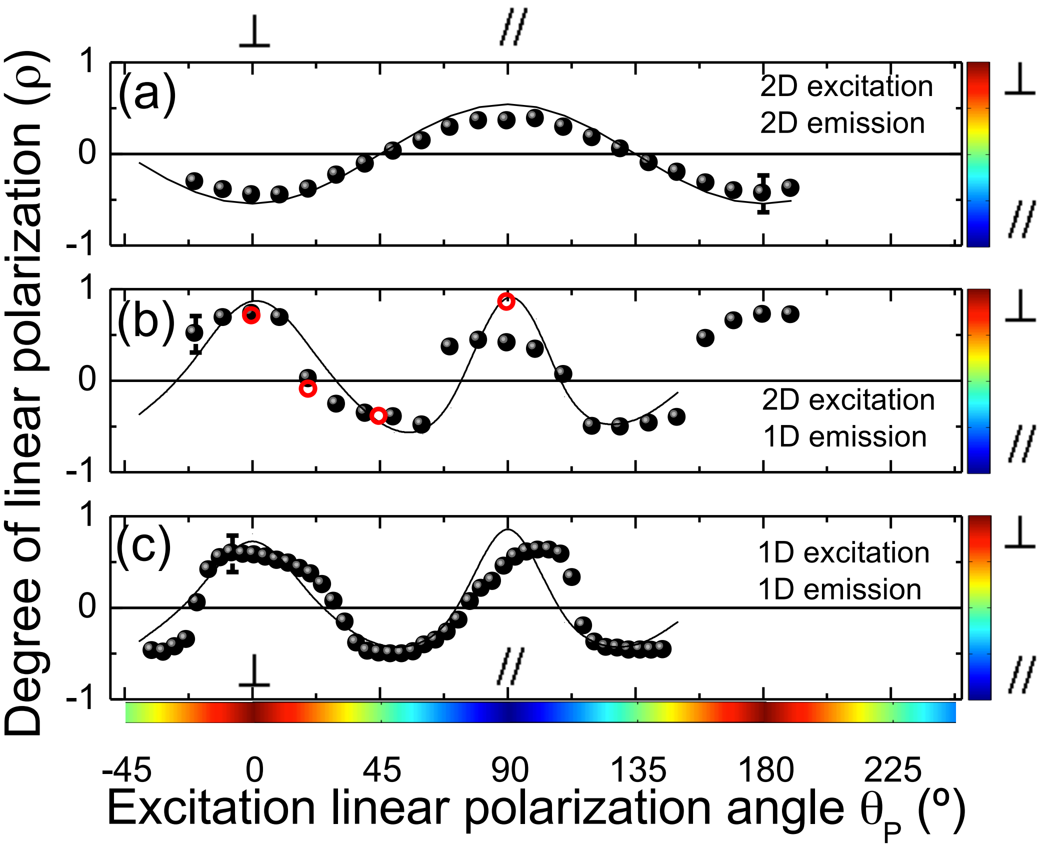

Figure 4.7: Degree of linear polarization as a function of the linear polarization angle of the pump: Colorbars next to the vertical and bottom axis represent the DLP of the emission and the pump, respectively. At $\theta_P = 0$ ($\theta_P = 90°$) the laser is polarized normal (parallel) to the wire, as indicated by the ⊥ (∥) symbol. The symbols at the ordinates indicate the main orientation of the emission's polarization plane: ⊥ (∥) perpendicular (normal) to the wire axis. (a) Shows the evolution of the DLP for the 2D system, for 2D phase-matching conditions. (b) Depicts the evolution of the DLP for the 1D system, for 2D phase-matching conditions. (c) Compiles the evolution of the DLP for the 1D system, for 1D phase-matching conditions. The solid lines (red open points) are calculated DLPs using the Boltzmann (GP) model (see § 4.5).

scattering. It confirms that in our system the interaction constants of same-(α_1) and opposite-(α_2)spin polaritons, described in § 1.4, are of opposite signs and that the interaction between polaritons of opposite spins is attractive [17].

Analysis of the 1D-case: The DLP of the 1D wire emission for the 2D phase-matching conditions, Fig. 4.7(b), is remarkably different to the one observed for the 2D condensate. Now the emission is polarized either parallel or normal to the wire with high DLP up to -0.7 and 0.8, respectively. Moreover, the transition between these two polarization states is very abrupt. Linear polarization inversion has also been observed in inter-band parametric scattering processes in polariton wires [94, 95], where a linearly polarized TM pump laser excites the TM mode and the parametric scattering brings the signal and idler polaritons to the TE mode of a different branch. Furthermore, our study, performed over the full range of the angles of the pump's polarization, reveals not only the inversion but also switching of the polarization with the double frequency of the rotation of the pump's polarization plane. Figure 4.7(c) shows the evolution of the wire DLP for 1D condensate phase-matching conditions: compared with Fig. 4.7(b) no significative differences are observed, suggesting that the 2D and 1D system are decoupled.

4.5 Theoretical model

In order to describe and interpret our experimental results, we profited from the collaboration with the group of professor G. Malpuech. Two complementary models were used to model the results: (i) the coupled 2D spinor Gross-Pitaevskii equation for excitons and Schrödinger equation for photons [99]; (ii) the semi-classical Boltzmann equations for populations and pseudo-spins of pump, signal and idler [100]. The former model allows to obtain spatial images similar to the experimental ones (Fig. 4.3), but is numerically very heavy, while the latter one captures the essence of the physics involved and allows to reproduce the DLP in the 2D and 1D cases (Fig. 4.7) when there is no need for spatial resolution.

4.5.1 Gross-Pitaevskii approach

In the first model, we write the coupled equations for a 2D four-component exciton-photon wave-function composed of a photonic fraction $\psi_{\uparrow\downarrow}(x,y)$ and a excitonic fraction $\varphi_{\uparrow\downarrow}(x,y)$:

$$\begin{gathered} i\hbar\frac{\partial\psi_{\uparrow\downarrow}}{\partial t} = -\frac{\hbar^2}{2m_C}\Delta\psi_{\uparrow\downarrow} + \frac{\hbar\Omega_R}{2}\varphi_{\uparrow\downarrow} + H_x\psi_{\downarrow\uparrow} \\ +U\psi_{\uparrow\downarrow} - \frac{i\hbar}{2\tau_{ph}}\psi_{\uparrow\downarrow} + P_{\uparrow\downarrow} + f_{\uparrow\downarrow} \end{gathered} \tag{4.1}$$

$$\begin{gathered} i\hbar\frac{\partial\varphi_{\uparrow\downarrow}}{\partial t} = -\frac{\hbar^2}{2m_X}\Delta\varphi_{\uparrow\downarrow} + \frac{\hbar\Omega_R}{2}\psi_{\uparrow\downarrow} + \alpha_1\left|\varphi_{\uparrow\downarrow}\right|^2\varphi_{\uparrow\downarrow} \\ +\alpha_2\left|\varphi_{\downarrow\uparrow}\right|^2\varphi_{\uparrow\downarrow} \end{gathered} \tag{4.2}$$

Here, $m_C = 4\times10^{-5}\,m_0$ is the photon mass, $m_X = 0.6\,m_0$ is the exciton mass, m_0 is the free electron mass, $\hbar\Omega_R = 4.2\ meV$ is the Rabi splitting, $\alpha_1 = 6\,E_b\,a_B^2$ and $\alpha_2 \sim -0.01\,\alpha_1$ are the triplet and singlet interaction constants [17], respectively. $E_b = 10\,meV$ is the exciton binding energy and $a_B = 10\,nm$ is the exciton Bohr radius. The potential acting on photons, confining them in the trap of width 4.25 μm and depth 0.6 meV, is described by U. $\tau_{ph} = 1ps$ is the photon lifetime (the exciton decay is neglected), P is the quasi-resonant pumping term, exciting the system at a given frequency $\omega \approx 1.6\,meV/\hbar$ above the bottom of the polariton branch and f is the noise, which serves to account for the effects of spontaneous scattering. Pumping provides an average of 10 particles in a 0.25 μm-wide unit cell in the steady state, and the spontaneous scattering creates 0.01 particles. The term $H_x = 30\ \mu eV$ describes the effective magnetic field (polarization splitting of 60 μeV) acting only inside the 1D wire.

The results of the simulations performed for the same four orientations of the pump polarization as in the experiments ($\theta_P = 0°,\ 20°,\ 45°$ and $90°$) are presented in the Fig. 4.8: they reproduce qualitatively the experimental observations of Fig. 4.3.

In these simulations, as in the experiments, in the 2D region the polarization is always inverted because of the opposite signs of α_1 and α_2, while in the quantized 1D region the polarization is determined by an interplay between the signs of the α's coefficients and the splitting between the parallel and transverse polarized modes, as explained in detail below.

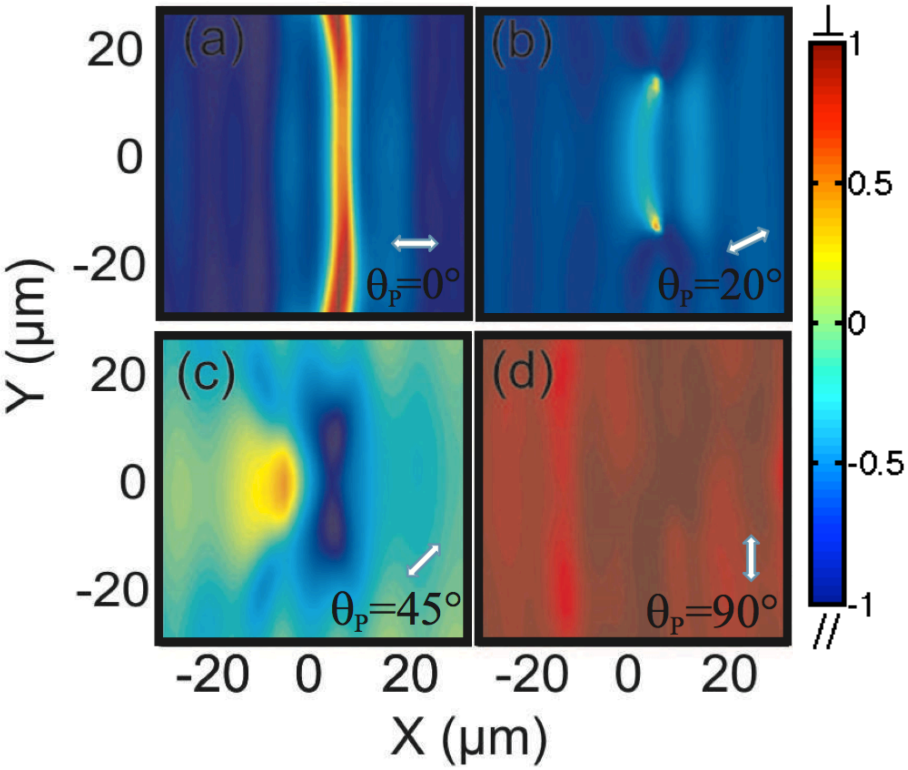

Figure 4.8: Calculated S_1 Stokes component for selected values of θ_P: (a) $\theta_P = 0°$, (b) $\theta_P = 20°$, (c) $\theta_P = 45°$ and (d) $\theta_P = 90°$.

Note, that in the simulations the 2D condensate extends over the entire area shown in the figure, in contrast to the experiments, where the condensate's extension is about 40 μm. Also, the DLP is higher in the calculations than in the experiments, however, a qualitative overall agreement between experiment and theory is evident. Although this model is nicely fitting the experiments, it is quite demanding numerically because of the need for a large 2D grid, a small step size to describe accurately the potential defect and the profiles of the modes, and long calculation times necessary to obtain spontaneous OPO with a relatively weak noise. In Figure 4.8(c), one can notice a small asymmetry between the left and the right side of the wire. This asymmetry is due to the direction of the propagation of the pump polaritons. The left part is "before" the defect and right part is "after" the defect.

4.5.2 Semi-classical Boltzmann approach

This approach considers only the three strongest populated modes (pump, signal and idler), while all others are neglected, which greatly improves the computational efficiency of the model. Using the experimental evidence of decoupled 2D and 1D systems, we calculate these sub-systems separately. The system of equations describing the dynamics of the pump, signal and idler populations and their pseudo-spins is written as:

$$\frac{dN_{k\uparrow,\downarrow}}{dt} = -\frac{N_{k\uparrow,\downarrow}}{\tau_k} + \left(\frac{dN_{k\uparrow,\downarrow}}{dt}\right)\bigg|_{rot} + \left(\frac{dN_{k\uparrow,\downarrow}}{dt}\right)\bigg|_{p-p} + P_k \tag{4.3}$$

$$\frac{d\mathbf{S}_k}{dt} = -\frac{\mathbf{S}_k}{\tau_k} + \left(\frac{d\mathbf{S}_k}{dt}\right)\bigg|_{rot} + \left(\frac{d\mathbf{S}_k}{dt}\right)\bigg|_{p-p} + \mathbf{P}_k \tag{4.4}$$

where $N_{k\uparrow,\downarrow}$ are the z projections of the populations and $\mathbf{S}_k$ is the in-plane pseudo-spin. Thus, $\mathbf{S}_k$ contains the S_x and S_y components, while the S_z projection is given by $N_\uparrow - N_\downarrow$. Here $k = p, s, i$ corresponds to the pump, signal and idler states. τ_k is the lifetime of the corresponding state, and P_k is the pumping term ($P_p = P$, $P_{s,i} = 0$). The semi-classical equations take into account the spontaneous and the stimulating scattering processes. We solve these equations separately for each case presented in Fig. 4.7: 2D [Fig. 4.7(a)], 1D out-of-resonance [Fig. 4.7(b)] and 1D resonant case [Fig. 4.7(c)]. All other relevant details of the model are given in the Annex.

These equations were used very efficiently to describe the polarization dynamics in various OPO configurations [93, 101], but always in the 2D case of planar cavities. The result of the simulation for the 2D system is presented as a solid line in Fig. 4.7(a) giving a very good agreement with the experimental data and showing polarization inversion.

However, the observed effects in the 1D case are not limited to a simple polarization inversion, and the model requires to be extended. The strong splitting between the linearly polarized polariton modes has not been treated so far. This splitting is of the order of 0.1 meV, and its effect is not limited to a simple precession of the polariton pseudo-spin in an effective magnetic field, analogous to the TE-TM field. It also affects energy conservation of polariton-polariton inelastic scattering processes, causing slightly different scattering rates into parallel and normal modes. This can be taken into account in the three-level model by introducing a new term to Eq. (4.4) describing the pseudo-spin dynamics of signal and idler:

$$+\mathbf{e}_x \delta W \left(\frac{dN_j}{dt} \right) \Bigg|_{p-p} \tag{4.5}$$

where $j = s, i$ stands for signal and idler, respectively. This term describes the dynamics of pseudo-spin projection on the unit vector $\mathbf{e}_x$ along the x-axis of polaritons scattered into s and i and is proportional to the relative difference between the scattering amplitudes into the linear modes $\delta W = (W_\perp - W_\parallel)/(W_\perp + W_\parallel)$. δW originates from the difference in the overlap integrals between the states localized in the trap and the extended propagating states of the pump and the idler. Indeed, the trap is wide enough to contain several quantized levels. The highest levels of the two orthogonal polarizations that become strongly populated in the experiments [see Figs. 4.3 and 4.9] do not have the same transverse quantum number n. Otherwise the transverse-polarized state $\perp$ would be higher in energy than the longitudinal-polarized state $\parallel$ because of the longitudinal-transverse splitting. The overlap integrals, contained in the scattering rates W, exhibit a $1/n$ dependence, implying that scattering into the lower lying states is favored. On the other hand, phase-matching conditions favor the population of higher lying ones. This balance leads actually to a further decrease of δW. Thus, this term is comparable to the one responsible for polarization inversion (the latter is proportional to α_2/α_1) and the competition between them can determine the relative sign of the signal's and pump's DLP. Values of $\alpha_2/\alpha_1 = -0.01$ and $\delta W = 0.008$ are typically used in the simulations.

This additional contribution would produce a linear polarization in the signal even for an unpolarized pump. Since scattering into one of the two polarization eigenstates is more efficient, it becomes populated stronger, which leads to an increase of the DLP. The interplay between the polarization inversion and the generation of linear polarization explains the observed DLP of the signal state in Figs. 4.7(b) and 4.7(c) for 2D and 1D phase-matching conditions, respectively. Since the linear polarization is generated by the presence of the confining potential, the resulting behavior is essentially the same for both cases.

A good agreement between both models concerning the DLP of the wire is obtained:

the results of the GP simulation of Fig. 4.8 are depicted as red open points in Fig. 4.7(b). They coincide well with the results of the Boltzmann model. Both theoretical approaches allow us to conclude that the peculiar behavior of the DLP for the 1D case is a result of the competition between the polarization inversion mechanism and the difference between the scattering rates towards the polarization eigenstates, which are quantized in the wire. The inversion mechanism is based on the spin-anisotropy of the interactions, which acts both for 2D and 1D. The nonlinearity of the OPO configuration does not allow representing the signal DLP simply as the sum of the two effects and the resulting curve becomes not sinusoidal. Finally, it is important to mention that this competition and the nonlinearities imply that the results would differ for a wire characterized by different parameters.

4.6 Polarization fine structure

The Boltzmann model renders well the change of the DLP for the 1D and 2D condensates and implies orthogonal, linearly polarized states with different polariton-polariton scattering rates. Indeed, our experiments reveal the existence of such polarization fine structure. We show in Fig. 4.9 spectrally and spatially resolved polarization false-color intensity maps of the 1D system for varying angle θ_P of the polarization of the pump under 2D phase-matching conditions. A length of ~ 1 μm in the x direction has been integrated to obtain these maps. Red and blue represent, as in the previous figures, linear polarizations normal and parallel to the wire axis, respectively. Note that higher values for the DLP than those depicted in Figs. 4.3 and 4.7 are obtained, since the non-polarized emission arising from the uncondensed phase is now spectrally filtered out.

The two energetically highest lying lines at ~1552 meV and ~1550 meV correspond to the excitation laser and the emission from the 2D system, respectively. In Fig. 4.9(a) the angle θ_P is zero and the polarization of the emission at ~1549 meV of the 1D system is the same as that of the excitation. However, for $\theta_P = 20°$, shown in Fig. 4.9(b), the emission of the 1D system consists of two split lines, each one with opposite linear polarization. In Fig. 4.9(c), $\theta_P = 45°$and the 1D system again shows just a single emission line polarized parallel to the wire. For an angle of $\theta_P = 90°$ the 1D system exhibits again emission of high DLP and polarization inversion occurs [see Fig. 4.9(d)].

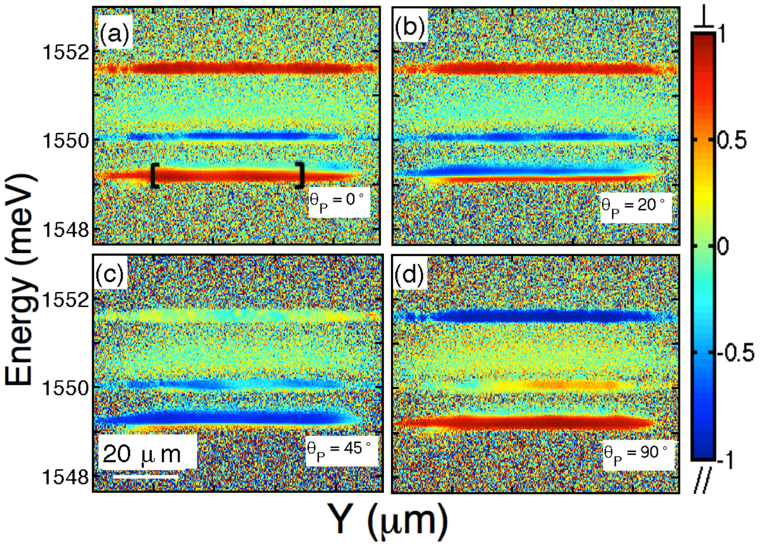

Figure 4.9: Spectrally resolved S_1 Stokes component, with the same selected values of θ_P as in previous figures. In (a) the 1D system shows emission polarized normal to the wire at ∼1549 meV. (b) Two lines with opposite polarization in the 1D condensate are resolved: at low (high) energy the emission is polarized normal (parallel) to the wire. In (c) again a single line is emitting. (d) The emission from the 1D system becomes again polarized normal to the wire. The square brackets in (a) delimit the range, along the wire, used to integrate the polarized emission that is shown in Fig. 4.10.

The polarized wire emission integrated along the wire, in the range enclosed by square brackets in Fig. 4.9(a), is shown in more detail in Fig. 4.10 for selected polarizations of the pump. The emission spectra exhibit shoulders, which suggests that more than one mode are excited, however, in the presented measurements they cannot be resolved due to experimental limitations. Furthermore, for all pump polarizations, a polarization splitting of the wire LPB into two orthogonal linearly polarized modes $LP^{1D}_{\parallel}$ and $LP^{1D}_{\perp}$ is obtained: they are polarized parallel and normal to the wire, respectively. Large polarization splitting in polariton wires has been observed previously and attributed to external strain [77, 94, 95] . In our samples, we observe marked cross-hatching suggesting the presence of large internal strain fields, which are possibly the source of the polarization splitting [78]. In Fig. 4.10 the splitting between the linearly polarized modes appears to be different in each of the Figs. 4.10(a)-4.10(d). One must consider that several components are present in each emission band (not resolvable due

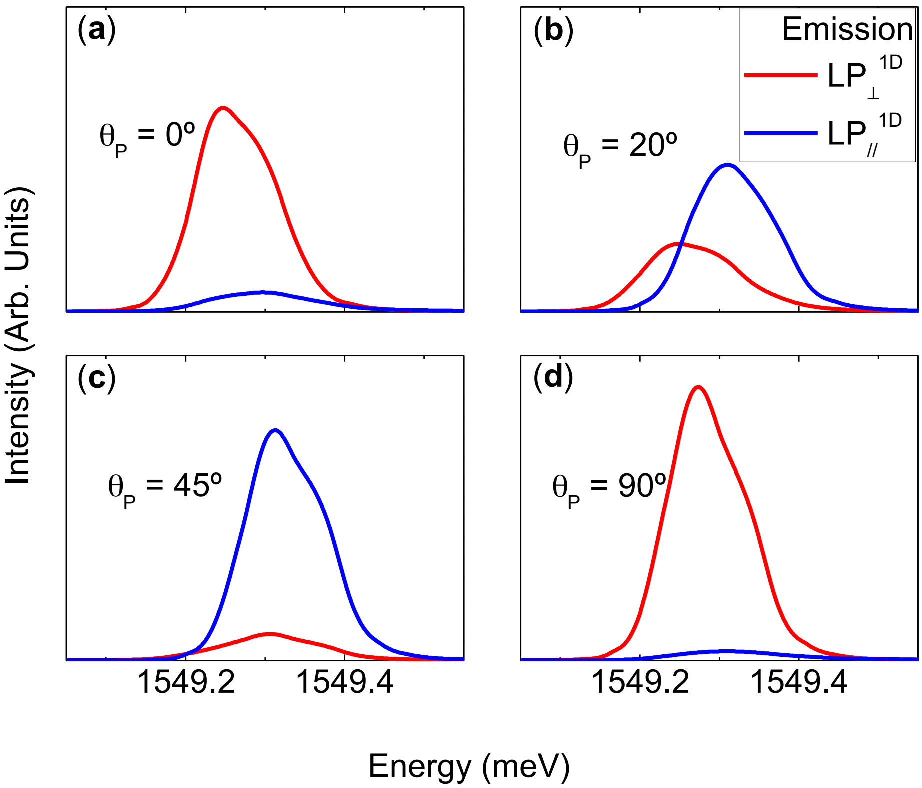

Figure 4.10: Emission spectra of the wire condensate for different θ_P. Polarization fine structure is observed and attributed to internal strain. The modes $LP_{\parallel}^{1D}$ and $LP_{\perp}^{1D}$ are polarized parallel and normal to the wire, respectively.

to experimental limitations) and that the relative changes of intensity of each component, together with the blueshifts due to polariton-polariton interactions, lead to an apparent change of the splitting. In Figs. 4.10(a) and 4.10(d) the pump is polarized normal and parallel to the wire, respectively: in both cases the dominant emission originates from the energetically lower lying, polarized normal to the wire, mode $LP_{\perp}^{1D}$, while the intensity of parallel polarized mode $LP_{\parallel}^{1D}$ is small, giving rise to a high DLP. The spectra in Fig. 4.10(b) ($\theta_P = 20°$) exhibit closer emission intensities from both lines, and therefore a vanishing DLP is observed in Figs. 4.3(b) and 4.7(b). Finally, in Fig. 4.10(c) the pump's polarization is diagonal and the emission arises mainly from the parallel polarized mode $LP_{\parallel}^{1D}$ rendering again a high DLP. In both cases shown in Figs. 4.10(b) and 4.10(c), the larger emission arises from the energetically higher lying state, $LP_{\parallel}^{1D}$, in contrast to what would be expected for a thermal distribution. However, polariton condensates, especially in the OPO regime, are highly non-thermal. This behavior is similar to the observation made in Ref. [96], where a splitting in the linear polarization is reported and a larger occupancy of the higher lying state is observed. This fact has been attributed to crystallographic anisotropy and pinning.

4.7 Summary

To sum up, we have investigated polarization properties of 2D and 1D polariton condensates as a function of angle of the pump's polarization plane, θ_P. In both cases, we observe polarization inversion for a pump polarization parallel to the wire. However, for the 1D wire, as the polarization plane of the excitation is rotated, we observe a switching between two states of high DLP. The switching between the two states occurs with the double frequency of the rotation of the pump's polarization plane. Two models, based on semiclassical Boltzmann kinetic equations and the Gross-Pitaevskii equation, respectively, are presented and reproduce well the polarization rotation for the 2D condensate and in particular the halved periodicity of the rotation for the 1D limit.

4.8 Annex

Here we give the details of the semi-classical Boltzmann approach used to simulate the DLP in the 2D and 1D cases. The rotational terms in Eq. (4.3) and (4.4) describe the action of various effective magnetic fields associated with polarization splittings:

$$\left(\frac{dN_{k\uparrow}}{dt}\right)\bigg|_{rot} = -\left(\frac{dN_{k\downarrow}}{dt}\right)\bigg|_{rot} = \mathbf{e}_z \cdot \left[\mathbf{S}_k \times \mathbf{\Omega}_{LT,\,k}\right] \;, \tag{4.6}$$

$$\left(\frac{d\mathbf{S}_k}{dt}\right)\bigg|_{rot} = \left[\mathbf{S}_k \times \mathbf{\Omega}_{int,\,k}\right] + \frac{N_{k\uparrow} - N_{k\downarrow}}{2}\mathbf{\Omega}_{LT,\,k} \;. \tag{4.7}$$

$\mathbf{\Omega}_{LT,k}$ is the effective magnetic field induced by the polariton TE-TM splitting [5], $\mathbf{\Omega}_{int}$ is an effective field due to spin-anisotropic interactions

$$\hbar\mathbf{\Omega}_{\mathrm{int},\mathbf{k}} = 2\mathbf{e}_z \sum_{\mathbf{k}'} \left(V^{(1)}_{\mathbf{k},\mathbf{k}',0} - V^{(2)}_{\mathbf{k},\mathbf{k}',0} \right) \left(N_{\mathbf{k}'\uparrow} - N_{\mathbf{k}'\downarrow} \right) , \tag{4.8}$$

where $V^{(1)}$and $V^{(2)}$ are the matrix elements of polariton-polariton interactions described in detail below, and $\mathbf{e}_z$ is a unit vector in the z direction of the Stokes spaces, corresponding to circularly polarized light. Finally, the polariton-polariton scattering terms can be expressed as

$$\begin{aligned}
\left(\frac{dN_{k\uparrow}}{dt}\right)\Bigg|_{p-p} \quad = \quad & \sum_{k',k''} \{ W^{(1)}_{k,k',k''} [(N_{k\uparrow} + N_{k'\uparrow} + 1) N_{k+k''\uparrow} N_{k'-k''\uparrow} \\
- \quad & (N_{k+k''\uparrow} + N_{k'-k''\uparrow} + 1) N_{k\uparrow} N_{k'\uparrow}] \\
+ \quad & W^{(1)}_{k,k',k''} [(N_{k\uparrow} + N_{k'\downarrow} + 1)(N_{k+k''\uparrow} N_{k'-k''\downarrow} + N_{k+k''\downarrow} N_{k'-k''\uparrow}) \\
+ \quad & 2\mathbf{S}_{k+k''} \cdot \mathbf{S}_{k'-k''}] \\
- \quad & (N_{k\uparrow} N_{k'\downarrow} + (\mathbf{S}_k \cdot \mathbf{S}_{k'}))(N_{k+k''\uparrow} + N_{k'-k''\downarrow} + N_{k+k''\downarrow} + N_{k'-k''\uparrow} + 2) \\
+ \quad & 2W^{(12)}_{k,k',k''} [N_{k''\uparrow} (\mathbf{S}_{k'} \cdot \mathbf{S}_{k'-k''}) + N_{k'-k''\uparrow} (\mathbf{S}_{k'} \cdot \mathbf{S}_{k+k''}) \\
- \quad & N_{k\uparrow} \mathbf{S}_{k'} \cdot (\mathbf{S}_{k'-k''} + \mathbf{S}_{k+k''})] \\
+ \quad & W^{(12)}_{k,k',k''} [(\mathbf{S}_k \cdot \mathbf{S}_{k+k''})(N_{k'-k''\uparrow} + N_{k'-k''\downarrow} - N_{k'\uparrow} - N_{k'\downarrow}) \\
+ \quad & (\mathbf{S}_k \cdot \mathbf{S}_{k'-k''})(N_{k+k''\uparrow} + N_{k+k''\downarrow} - N_{k'\uparrow} - N_{k'\downarrow})]\}
\end{aligned} \tag{4.9}$$

$$
\begin{array}{rcl}
\left(\dfrac{dS_k}{dt}\right)\Bigg|_{p-p} & = & \displaystyle\sum_{k',q}\{\frac{W^{(1)}_{\mathbf{k},\mathbf{k}',\mathbf{q}}}{2}\mathbf{S}_{\mathbf{k}}[N_{\mathbf{k}+\mathbf{q}\uparrow}N_{\mathbf{k}'-\mathbf{q}\uparrow}+N_{\mathbf{k}+\mathbf{q}\downarrow}N_{\mathbf{k}'-\mathbf{q}\downarrow} \\
 & - & N_{\mathbf{k}'\uparrow}(N_{\mathbf{k}+\mathbf{q}\uparrow}+N_{\mathbf{k}'-\mathbf{q}\uparrow}+1)-N_{\mathbf{k}'\downarrow}(N_{\mathbf{k}+\mathbf{q}\downarrow}+N_{\mathbf{k}'-\mathbf{q}\downarrow}+1)] \\
 & + & W^{(1)}_{\mathbf{k},\mathbf{k}',\mathbf{q}}\left(\mathbf{S}_{\mathbf{k}+\mathbf{q}}(\mathbf{S}_{\mathbf{k}'}\cdot\mathbf{S}_{\mathbf{k}'-\mathbf{q}})+\mathbf{S}_{\mathbf{k}'-\mathbf{q}}(\mathbf{S}_{\mathbf{k}'}\cdot\mathbf{S}_{\mathbf{k}+\mathbf{q}})-\mathbf{S}_{\mathbf{k}'}(\mathbf{S}_{\mathbf{k}+\mathbf{q}}\cdot\mathbf{S}_{\mathbf{k}'-\mathbf{q}})\right) \\
 & + & \dfrac{W^{(2)}_{\mathbf{k},\mathbf{k}',\mathbf{q}}}{2}\,[2(\mathbf{S}_{\mathbf{k}}+\mathbf{S}_{\mathbf{k}'})\left(N_{\mathbf{k}+\mathbf{q}\uparrow}N_{\mathbf{k}'-\mathbf{q}\downarrow}+N_{\mathbf{k}+\mathbf{q}\downarrow}N_{\mathbf{k}'-\mathbf{q}\uparrow}+2(\mathbf{S}_{\mathbf{k}+\mathbf{q}}\cdot\mathbf{S}_{\mathbf{k}'-\mathbf{q}})\right) \\
 & - & (\mathbf{S}_{\mathbf{k}}(N_{\mathbf{k}'\uparrow}+N_{\mathbf{k}'\downarrow})+\mathbf{S}_1(N_{\mathbf{k}\uparrow}+N_{\mathbf{k}\downarrow}))(N_{\mathbf{k}+\mathbf{q}\uparrow}+N_{\mathbf{k}'-\mathbf{q}\uparrow}+N_{\mathbf{k}+\mathbf{q}\downarrow}+N_{\mathbf{k}'-\mathbf{q}\downarrow}+2)] \\
 & - & 2W^{(12)}_{\mathbf{k},\mathbf{k}',\mathbf{q}}\mathbf{S}_{\mathbf{k}}\left((\mathbf{S}_{\mathbf{k}'}\cdot\mathbf{S}_{\mathbf{k}+\mathbf{q}})+(\mathbf{S}_{\mathbf{k}'}\cdot\mathbf{S}_{\mathbf{k}'-\mathbf{q}})\right) \\
 & + & \dfrac{W^{(12)}_{\mathbf{k},\mathbf{k}',\mathbf{q}}}{2}\mathbf{S}_{\mathbf{k}'-\mathbf{q}}[2((N_{\mathbf{k}'\uparrow}+1)N_{\mathbf{k}+\mathbf{q}\uparrow}+(N_{\mathbf{k}'\downarrow}+1)N_{\mathbf{k}+\mathbf{q}\downarrow}) \\
 & + & (N_{\mathbf{k}+\mathbf{q}\uparrow}+N_{\mathbf{k}+\mathbf{q}\downarrow}-N_{\mathbf{k}'\uparrow}-N_{\mathbf{k}'\downarrow})(N_{\mathbf{k}\uparrow}+N_{\mathbf{k}\downarrow})] \\
 & + & \dfrac{W^{(12)}_{\mathbf{k},\mathbf{k}',\mathbf{q}}}{2}\mathbf{S}_{\mathbf{k}+\mathbf{q}}[2((N_{\mathbf{k}'\uparrow}+1)N_{\mathbf{k}'-\mathbf{q}\uparrow}+(N_{\mathbf{k}'\downarrow}+1)N_{\mathbf{k}'-\mathbf{q}\downarrow}) \\
 & + & +(N_{\mathbf{k}'-\mathbf{q}\uparrow}+N_{\mathbf{k}'-\mathbf{q}\downarrow}-N_{\mathbf{k}'\uparrow}-N_{\mathbf{k}'\downarrow})(N_{\mathbf{k}\uparrow}+N_{\mathbf{k}\downarrow})]
\end{array}
\tag{4.10}
$$

describe numerous experiments on the polariton OPO [93, 101]. They are presented here for the reader's convenience. The terms $W^{(1)}$, $W^{(2)}$ and $W^{(12)}$ represent polariton-polariton interactions in different spin configurations:

$$
W^{(1)}_{k,k',k''} = \frac{2\pi}{h}\left|V^{(1)}_{k,k',k''}\right|^2 \delta(\Omega_k+\Omega_{k'}-\Omega_{k+k''}-\Omega_{k-k''}) \tag{4.11}
$$

$$
W^{(2)}_{k,k',k''} = \frac{2\pi}{h}\left|V^{(2)}_{k,k',k''}\right|^2 \delta(\Omega_k+\Omega_{k'}-\Omega_{k+k''}-\Omega_{k-k''}) \tag{4.12}
$$

$$
\begin{array}{l}
W^{(12)}_{k,k',k''} = \dfrac{2\pi}{h}\mathrm{Re}(V^{(1)}_{k,k',k''}V^{*(2)}_{k,k',k''}) \\
\\
\times\,\delta(\Omega_k+\Omega_{k'}-\Omega_{k+k''}-\Omega_{k-k''})
\end{array}
\tag{4.13}
$$

Equations (4.11)-(4.13) are written for the most general case. Taking into account the excitonic fraction of the relevant states, and assuming a contact interaction for the matrix elements V, therefore not depending on k, $V^{(1)}$ and $V^{(2)}$ correspond to the α_1 and α_2 parameters of the Gross-Pitaevskii Eq. (4.2). We assume for the calculations the usual ratio $\alpha_2/\alpha_1 \sim -0.01$ (see Refs. [17, 93]), which obtains a negative $W^{(12)}_{0,k_p,k_p}$. Since the expression for the in-plane pseudo-spin reduces to

$$\frac{d\mathbf{S}_s}{dt} = W^{(12)}_{0,k_p,k_p} \left(N_{\uparrow p} + N_{p\downarrow} \right) \mathbf{S}_p \ , \tag{4.14}$$

the negative sign of $W^{(12)}_{0,k_p,k_p}$ leads to polarization inversion during spontaneous scattering from the pump to the signal state.

Chapter 5

General conclusions

In this thesis we have investigated polaritons condensates created under the OPO configuration. Its coherence properties were addressed in Chapter 3 and the polarization properties presented in Chapter 4.

The measurements for the first order correlation function have shown that very long coherence times and extended spatial coherence can be obtained even for polaritons with lifetimes of the order of $\sim 2\,ps$. Coherence times lasting up to $\sim 3\,ns$, the longest ones reported in microcavities, were achieved either by increasing the size of the condensates (increasing the pump spot size and keeping the excitation power density fixed) or by increasing the pump power leaving fixed the condensate size. The main effect of both approaches is to increase the number of condensed particles and this causes that the condensates fall into a motional narrowing regime.

The appearance of spontaneous spatial coherence has been demonstrated following the proposal by Carusotto and Ciuti [58], where the threshold for condensation is achieved by varying the excitation laser energy.

Different regimes were observed as a function of the pump power:

- Below power threshold for condensation, both the spatial and temporal coherence showed a fast decay, the former decayed within the polariton's de Broglie wavelength, and the latter attained a coherence time of $\sim 7\,ps$ with a well defined exponential decay.
- Slightly above power threshold both, spatial and temporal coherence displayed an in-

crease of its characteristic decay, the coherence time went up to ∼80 *ps* and the spatial coherence became 3 time more extended than that in the non-condensed case.

- Well above the power threshold, the condensate showed remarkable features like a flat spatial coherence, limited only by the pump spot size, and coherence times of the order of ∼3 *ns*.

Moreover it has been shown that defects in the DBR can trap polaritons and form a condensate. By properly adjusting the phase-matching conditions, one can create either solely a 1D condensate or coexisting 1D and 2D condensates. In the case of an isolated 1D condensate, it has been found that the coherence decays rapidly over length scales much smaller than the excitation spot size. It has been also obtained that the coherence time is one order of magnitude smaller than that of a 2D condensate created in the same sample. Such a behavior reflects the increasing importance of fluctuations as the dimensionality is reduced. Additionally, the larger disorder in the 1D system, as compared with the 2D one, is responsible for the degradation of the coherence in the condensate trapped by the defects.

The polarization properties of the coexisting 2D-1D condensates have been studied, the 2D condensate showed that its emission is polarized and rotated about ∼90º with respect to the linear polarization of the laser, presenting a sinusoidal-like behavior, with a period $T = \pi$, as a function of the orientation of the laser's plane polarization. The 1D condensate, on the other hand, presented a different behavior:

- Its polarized emission was aligned with respect to the polarization of the laser when the pump's plane polarization is perpendicular to the main axis of the defect.
- On the other hand its polarized emission was inverted ∼90º with respect to the laser's plane polarization for pump's plane polarization along the axis of the defect.
- When the pump's plane polarization laid in either of the diagonals with respect to the axis of the defect, the polarized emission was oriented along the defect's axis.

This behavior has been successfully explained theoretically by the group of G. Malpuech considering that the state of the polarized emission is a result of two effects: a precession due to the presence of a induced magnetic field by the TE-TM splitting and the difference in the scattering rate towards the different highly linearly polarized states present in the 1D system, which is determined by the overlap integrals between the states localized in the trap and the extended propagating states of the pump and the idler.

Conclusiones generales

En esta tesis hemos investigado condensados de polaritones creados en la configuración de excitación de oscilador paramétrico óptico (OPO). En el Capítulo 3 se han estudiado sus propiedades de coherencia, mientras que en el Capítulo 4 se han abordado sus propiedades de polarización.

Las medidas de la función de correlación de primer orden ($g^{(1)}$) han mostrado la posibilidad de obtener tiempos de coherencia muy largos y coherencia espacial macroscópica, incluso cuando los polaritones tienen tiempos de vida del orden de $\sim$2 ps. Se han obtenido tiempos de coherencia del orden de $\sim$3 ns, los más largos reportados en microcavidades. Este resultado experimental se consiguió a través de dos procedimientos: aumentando el tamaño del haz de excitación y manteniendo su densidad de potencia constante o manteniendo fijo el tamaño del haz y aumentando su potencia de bombeo. El principal efecto de los dos métodos es aumentar el número de partículas condensadas, provocando que el condensado entre en un régimen de estrechamiento debido al movimiento ("motional narrowing").

Además, se ha demostrado la aparición de coherencia espacial espontánea siguiendo la propuesta teórica de Carusotto y Ciuti [58], donde el umbral de condensación se define en función de la energía de excitación del láser.

Se han observado diferentes regímenes del estado de los polaritones que dependen de la potencia de bombeo:

- Cuando ésta se encuentra bajo la potencia umbral de condensación, en el que la coherencia espacial y la coherencia temporal han mostrado un decaimiento rápido. La coherencia espacial decae en el rango de la longitud de onda de de Broglie de los polaritones, mientras que la coherencia temporal es del orden de $\sim$7 ps, con un marcado decaimiento exponencial.

- Cuando la potencia de bombeo tiene un valor justo por encima de la potencia umbral. En este caso las coherencias temporal y espacial muestran un incremento del decaimiento característico: la coherencia temporal decae en el rango de los $\sim$80 ps, y la coherencia espacial incrementa 3 veces con respecto al caso anterior.

- Por último, cuando la potencia de bombeo excita muy por encima del valor de la potencia umbral para la condensación de polaritones. Éste adquiere propiedades notables como una coherencia espacial plana (únicamente limitada por el tamaño del haz de bombeo) y una coherencia temporal del orden de $\sim$3 ns.

Por otra parte, se ha mostrado que los defectos en los espejos de Bragg de la microcavidad pueden generar estados localizados donde los polaritones quedan condensados y atrapados por ellos. Bajo condiciones apropiadas de ajuste de fase se puede crear un condensado 1D aislado (sin condensación en la región 2D) o un condensado extendido a un sistema 2D-1D. En el caso del condensado 1D aislado, se ha encontrado que la coherencia decae rápidamente en distancias mucho más pequeñas que el tamaño del haz de excitación. También se ha obtenido que el tiempo de coherencia es un orden de magnitud más pequeño que el correspondiente al condensado en la región 2D en la misma zona de la muestra. Este comportamiento refleja la importancia de las fluctuaciones cuando la dimensionalidad se reduce. Adicionalmente, el desorden que presenta el sistema 1D, comparado con el sistema 2D, es responsable de la degradación de la coherencia en un condensado confinado en un defecto.

Finalmente se detallan los resultados obtenidos en la investigación de las propiedades de polarización del condensado en los sistemas 2D-1D. El condensado bidimensional muestra una emisión linealmente polarizada y rotada $\sim$90º con respecto a la polarización lineal del haz de excitación. También se observa una oscilación sinusoidal con un periodo T $= \pi$ en función del ángulo de orientación del plano de polarización lineal del láser. Por otro lado, el condensado 1D presenta un comportamiento significativamente diferente:

- Cuando el plano de polarización del láser está alineado perpendicularmente al eje longitudinal del defecto, la emisión linealmente polarizada del defecto está alineada con el plano de polarización del láser.

- Por otra parte, cuando el plano de polarización de la excitación está alineado paralelamente al eje longitudinal del defecto, la emisión polarizada del condensado 1D está invertida ∼90º con respecto al plano de polarización del láser.
- En el caso intermedio en el que el plano de polarización de la excitación yace a lo largo de cualquiera de las direcciones diagonales con respecto al eje del defecto, la emisión polarizada se orienta a lo largo del eje del mismo.

Este comportamiento se ha explicado teóricamente con las simulaciones realizadas por el grupo de investigación del Prof. G. Malpuech, considerando que la emisión polarizada es el resultado de dos efectos: una precesión debida a la presencia de un campo magnético efectivo, inducido por la separación TE-TM, y la diferencia en la tasa de "scattering" hacia los distintos estados polarizados presentes en el sistema 1D, dicha tasa queda determinada por las integrales de solapamiento entre estados localizados en la trampa 1D y la propagación extendida de los estados de bombeo y ocioso (“idler”).

Bibliography

[1] C. Kittel, *Introduction to Solid State Physics* (John Wiley & Sons, Inc., New York, 2005), 8th ed. 1

[2] M. Yu., P. Cardona., *Fundamentals of Semiconductors: Physics and Materials Properties* (Springer, Berlin, 2010), URL `http://www.springer.com/materials/optical+26+electronic+materials/book/978-3-642-00709-5`. 2, 3, 4

[3] E. Rosencher, *Optoelectronics* (Cambridge University Press, Cambridge, 2002), ISBN 9780521778138. 5

[4] A. Kavokin, J. Baumberg, G. Malpuech, and F. Laussy, *Microcavities*, Oxford science publications (Oxford University Press, Oxford, 2011), ISBN 9780199602278, URL `http://books.google.es/books?id=2g7wHcMcaJ0C`. 6, 20, 34

[5] G. Panzarini, L. C. Andreani, A. Armitage, D. Baxter, M. S. Skolnick, V. N. Astratov, J. S. Roberts, A. V. Kavokin, M. R. Vladimirova, and M. A. Kaliteevski, Phys. Rev. B **59**, 5082 (1999), URL `http://link.aps.org/doi/10.1103/PhysRevB.59.5082`. 7, 13, 95

[6] G. Bastard and J. A. Brum, IEEE Journal of Quantum Electronics **22**, 1625 (1986), ISSN 0018-9197, URL `http://ieeexplore.ieee.org/xpl/articleDetails.jsp?arnumber=1073186`. 9

[7] R. Winkler, *Spin-orbit Coupling Effects in Two-Dimensional Electron and Hole Systems* (Springer, Berlin, 2003), ISBN 9783540011873. 9

[8] F. Tassone, F. Bassani, and L. C. Andreani, Phys. Rev. B **45**, 6023 (1992), URL `http://link.aps.org/doi/10.1103/PhysRevB.45.6023`. 10

[9] M. Z. Maialle, E. A. de Andrada e Silva, and L. J. Sham, Phys. Rev. B **47**, 15776 (1993), URL `http://link.aps.org/doi/10.1103/PhysRevB.47.15776`. 10, 13

[10] C. Weisbuch, M. Nishioka, A. Ishikawa, and Y. Arakawa, Phys. Rev. Lett. **69**, 3314 (1992), URL `http://link.aps.org/doi/10.1103/PhysRevLett.69.3314`. 10

[11] E. M. Purcell., Phys. Rev. **69**, 681 (1946), URL `http://link.aps.org/doi/10.1103/PhysRev.69.674.2`. 10

[12] M. S. Skolnick, T. A. Fisher, and D. M. Whittaker, Semicond. Sci. Technol. **13**, 645 (1998), ISSN 0268-1242, URL `http://iopscience.iop.org/0268-1242/13/7/003`. 10

[13] V. Savona, L. C. Andreani, P. Schwendimann, and A. Quattropani, Solid State Communications **93**, 733 (1995), ISSN 0038-1098, URL `http://www.sciencedirect.com/science/article/pii/0038109894008655`. 11

[14] J. J. Hopfield, Phys. Rev. **112**, 1555 (1958), URL `http://link.aps.org/doi/10.1103/PhysRev.112.1555`. 11

[15] I. A. Shelykh, A. V. Kavokin, Y. G. Rubo, T. C. H. Liew, and G. Malpuech, Semicond. Sci. Technol. **25**, 013001 (2010), ISSN 0268-1242, URL `http://iopscience.iop.org/0268-1242/25/1/013001`. 13

[16] M. D. Martín, G. Aichmayr, L. Viña, and R. André, Phys. Rev. Lett. **89**, 077402 (2002), URL `http://link.aps.org/doi/10.1103/PhysRevLett.89.077402`. 14, 73, 75

[17] M. Vladimirova, S. Cronenberger, D. Scalbert, K. V. Kavokin, A. Miard, A. Lemaître, J. Bloch, D. Solnyshkov, G. Malpuech, and A. V. Kavokin, Phys. Rev. B **82**, 075301 (2010), URL `http://link.aps.org/doi/10.1103/PhysRevB.82.075301`. 14, 86, 87, 97

[18] P. G. Savvidis, J. J. Baumberg, R. M. Stevenson, M. S. Skolnick, D. M. Whittaker, and J. S. Roberts, Phys. Rev. Lett. **84**, 1547 (2000), URL `http://link.aps.org/doi/10.1103/PhysRevLett.84.1547`. 16, 17

[19] P. G. Lagoudakis, P. G. Savvidis, J. J. Baumberg, D. M. Whittaker, P. R. Eastham, M. S. Skolnick, and J. S. Roberts, Phys. Rev. B **65**, 161310 (2002), URL `http://link.aps.org/doi/10.1103/PhysRevB.65.161310`. 74, 80

[20] A. Kavokin, P. G. Lagoudakis, G. Malpuech, and J. J. Baumberg, Phys. Rev. B **67**, 195321 (2003), URL `http://link.aps.org/doi/10.1103/PhysRevB.67.195321`. 16, 74

[21] R. M. Stevenson, V. N. Astratov, M. S. Skolnick, D. M. Whittaker, M. Emam-Ismail, A. I. Tartakovskii, P. G. Savvidis, J. J. Baumberg, and J. S. Roberts, Phys. Rev. Lett. **85**, 3680 (2000), URL `http://link.aps.org/doi/10.1103/PhysRevLett.85.3680`. 16, 27

[22] A. I. Tartakovskii, D. N. Krizhanovskii, and V. D. Kulakovskii, Phys. Rev. B **62**, R13298 (2000), URL `http://link.aps.org/doi/10.1103/PhysRevB.62.R13298`.

[23] J. J. Baumberg, P. G. Savvidis, R. M. Stevenson, A. I. Tartakovskii, M. S. Skolnick, D. M. Whittaker, and J. S. Roberts, Phys. Rev. B **62**, R16247 (2000), URL `http://link.aps.org/doi/10.1103/PhysRevB.62.R16247`. 16, 27

[24] C. Ciuti, P. Schwendimann, B. Deveaud, and A. Quattropani, Phys. Rev. B **62**, R4825 (2000), URL `http://link.aps.org/doi/10.1103/PhysRevB.62.R4825`. 17

[25] S. Kundermann, M. Saba, C. Ciuti, T. Guillet, U. Oesterle, J. L. Staehli, and B. Deveaud, Phys. Rev. Lett. **91**, 107402 (2003), URL `http://link.aps.org/doi/10.1103/PhysRevLett.91.107402`. 17, 18, 27

[26] A. Einstein., Sitzungber. Preuss. Akad. Wiss. **1**, 3 (1925). 19

[27] F. London, Nature **141**, 643 (1938). 19

[28] O. Penrose and L. Onsager, Phys. Rev. **104**, 576 (1956), URL `http://link.aps.org/doi/10.1103/PhysRev.104.576`. 19, 25, 47

[29] J. Goldstone, Nuovo Cim **19**, 154 (1961), ISSN 0029-6341, 1827-6121, URL `http://link.springer.com/article/10.1007/BF02812722`.

[30] P. W. ANDERSON, Rev. Mod. Phys. **38**, 298 (1966), URL `http://link.aps.org/doi/10.1103/RevModPhys.38.298`. 19, 24

[31] M. H. Anderson, J. R. Ensher, M. R. Matthews, C. E. Wieman, and E. A. Cornell, Science **269**, 198 (1995), ISSN 0036-8075, 1095-9203, PMID: 17789847, URL `http://www.sciencemag.org/content/269/5221/198`. 19

[32] J. Kasprzak, M. Richard, S. Kundermann, A. Baas, P. Jeambrun, J. M. J. Keeling, F. M. Marchetti, M. H. Szymańska, R. André, J. L. Staehli, et al., Nature **443**, 409 (2006), ISSN 0028-0836, URL `http://www.nature.com/nature/journal/v443/n7110/full/nature05131.html`. 19, 25, 26, 48

[33] R. P. Feynman, *Statistical Mechanics: A Set Of Lectures* (Westview Press, 1998), ISBN 081334610X. 20

[34] A. Griffin, D. W. Snoke, and S. Stringari, *Bose-Einstein Condensation* (Cambridge University Press, 1996), ISBN 9780521589901. 20

[35] L. P. Pitaevskii and S. Stringari, *Bose-Einstein Condensation* (Oxford University Press, Oxford, 2003), ISBN 9780198507192. 22, 64, 66, 67

[36] N. N. Bogoliubov., Journal of Physics **11** (1947). 22

[37] M. O. Scully and M. S. Zubairy, *Quantum Optics* (Cambridge University Press, 1997), ISBN 9780521434584. 24, 55

[38] R. J. Glauber, Phys. Rev. **130**, 2529 (1963), URL `http://link.aps.org/doi/10.1103/PhysRev.130.2529`. 25

[39] A. Imamoglu, R. J. Ram, S. Pau, and Y. Yamamoto, Phys. Rev. A **53**, 4250 (1996), URL `http://link.aps.org/doi/10.1103/PhysRevA.53.4250`. 25

[40] L. S. Dang, D. Heger, R. André, F. Bœuf, and R. Romestain, Phys. Rev. Lett. **81**, 3920 (1998), URL `http://link.aps.org/doi/10.1103/PhysRevLett.81.3920`. 25

[41] C. Schneider, A. Rahimi-Iman, N. Y. Kim, J. Fischer, I. G. Savenko, M. Amthor, M. Lermer, A. Wolf, L. Worschech, V. D. Kulakovskii, et al., Nature **497**, 348 (2013), ISSN 0028-0836, URL `http://www.nature.com/nature/journal/v497/n7449/full/nature12036.html`. 25

[42] H. Deng, G. Weihs, C. Santori, J. Bloch, and Y. Yamamoto, Science **298**, 199 (2002), ISSN 0036-8075, 1095-9203, PMID: 12364801, URL `http://www.sciencemag.org/content/298/5591/199`. 25

[43] R. Balili, V. Hartwell, D. Snoke, L. Pfeiffer, and K. West, Science **316**, 1007 (2007), ISSN 0036-8075, 1095-9203, URL `http://www.sciencemag.org/content/316/5827/1007`. 26

[44] C. W. Lai, N. Y. Kim, S. Utsunomiya, G. Roumpos, H. Deng, M. D. Fraser, T. Byrnes, P. Recher, N. Kumada, T. Fujisawa, et al., Nature **450**, 529 (2007), ISSN 0028-0836, URL `http://www.nature.com/nature/journal/v450/n7169/full/nature06334.html`. 26

[45] K. G. Lagoudakis, M. Wouters, M. Richard, A. Baas, I. Carusotto, R. André, L. S. Dang, and B. Deveaud-Plédran, Nature Physics **4**, 706 (2008), ISSN 1745-2473, URL `http://www.nature.com/nphys/journal/v4/n9/full/nphys1051.html`. 26

[46] K. G. Lagoudakis, T. Ostatnický, A. V. Kavokin, Y. G. Rubo, R. André, and B. Deveaud-Plédran, Science **326**, 974 (2009), ISSN 0036-8075, 1095-9203, PMID: 19965506, URL `http://www.sciencemag.org/content/326/5955/974`. 26

[47] G. Tosi, F. M. Marchetti, D. Sanvitto, C. Antón, M. H. Szymańska, A. Berceanu, C. Tejedor, L. Marrucci, A. Lemaître, J. Bloch, et al., Phys. Rev. Lett. **107**, 036401 (2011), URL `http://link.aps.org/doi/10.1103/PhysRevLett.107.036401`. 26

[48] A. Amo, D. Sanvitto, F. P. Laussy, D. Ballarini, E. d. Valle, M. D. Martin, A. Lemaître, J. Bloch, D. N. Krizhanovskii, M. S. Skolnick, et al., Nature **457**, 291 (2009), ISSN 0028-0836, URL `http://www.nature.com/nature/journal/v457/n7227/full/nature07640.html`. 26

[49] A. Amo, J. Lefrère, S. Pigeon, C. Adrados, C. Ciuti, I. Carusotto, R. Houdré, E. Giacobino, and A. Bramati, Nature Physics **5**, 805 (2009), ISSN 1745-2473, URL `http://www.nature.com/nphys/journal/v5/n11/full/nphys1364.html`. 26

[50] D. Sanvitto, F. M. Marchetti, M. H. Szymańska, G. Tosi, M. Baudisch, F. P. Laussy, D. N. Krizhanovskii, M. S. Skolnick, L. Marrucci, A. Lemaître, et al., Nat Phys **6**, 527 (2010), ISSN 1745-2473, URL `http://www.nature.com/nphys/journal/v6/n7/full/nphys1668.html`. 26

[51] A. Amo, S. Pigeon, D. Sanvitto, V. G. Sala, R. Hivet, I. Carusotto, F. Pisanello, G. Leménager, R. Houdré, E. Giacobino, et al., Science **332**, 1167 (2011), ISSN 0036-8075, 1095-9203, URL `http://www.sciencemag.org/content/332/6034/1167`. 26

[52] M. Sich, D. N. Krizhanovskii, M. S. Skolnick, A. V. Gorbach, R. Hartley, D. V. Skryabin, E. A. Cerda-Méndez, K. Biermann, R. Hey, and P. V. Santos, Nature Photonics **6**, 50 (2012), ISSN 1749-4885, URL `http://www.nature.com/nphoton/journal/v6/n1/full/nphoton.2011.267.html`. 26

[53] M. Wouters and I. Carusotto, Phys. Rev. A **76**, 043807 (2007), URL `http://link.aps.org/doi/10.1103/PhysRevA.76.043807`. 26, 64, 67

[54] D. Ballarini, D. Sanvitto, A. Amo, L. Viña, M. Wouters, I. Carusotto, A. Lemaitre, and J. Bloch, Phys. Rev. Lett. **102**, 056402 (2009), URL `http://link.aps.org/doi/10.1103/PhysRevLett.102.056402`. 27

[55] M. H. Szymańska, J. Keeling, and P. B. Littlewood, Phys. Rev. Lett. **96**, 230602 (2006), URL `http://link.aps.org/doi/10.1103/PhysRevLett.96.230602`. 27

[56] R. Butté, M. S. Skolnick, D. M. Whittaker, D. Bajoni, and J. S. Roberts, Phys. Rev. B **68**, 115325 (2003), URL `http://link.aps.org/doi/10.1103/PhysRevB.68.115325`. 27

[57] D. N. Krizhanovskii, D. Sanvitto, A. P. D. Love, M. S. Skolnick, D. M. Whittaker, and J. S. Roberts, Phys. Rev. Lett. **97**, 097402 (2006), URL `http://link.aps.org/doi/10.1103/PhysRevLett.97.097402`. 27, 48, 57

[58] I. Carusotto and C. Ciuti, Phys. Rev. B **72**, 125335 (2005), URL `http://link.aps.org/doi/10.1103/PhysRevB.72.125335`. 27, 47, 48, 53, 61, 63, 66, 69, 99, 103

[59] J. M. Hvam, *Private communication.* 29

[60] P. Borri, W. Langbein, U. Woggon, J. R. Jensen, and J. M. Hvam, Phys. Rev. B **63**, 035307 (2000), URL `http://link.aps.org/doi/10.1103/PhysRevB.63.035307`. 29, 30

[61] E. D. Black, **69**, 79 (2001), ISSN 00029505, URL `http://scitation.aip.org/content/aapt/journal/ajp/69/1/10.1119/1.1286663`. 32

[62] (lugar, ????). 34

[63] T. Kreis, J. Opt. Soc. Am. A **3**, 847 (1986), URL `http://josaa.osa.org/abstract.cfm?URI=josaa-3-6-847`. 40

[64] D. M. Whittaker and P. R. Eastham, EPL **87**, 27002 (2009), ISSN 0295-5075, URL `http://iopscience.iop.org/0295-5075/87/2/27002`. 48, 57, 59, 61, 71

[65] F. Tassone and Y. Yamamoto, Phys. Rev. A **62**, 063809 (2000), URL `http://link.aps.org/doi/10.1103/PhysRevA.62.063809`. 48

[66] D. Porras and C. Tejedor, Phys. Rev. B **67**, 161310 (2003), URL `http://link.aps.org/doi/10.1103/PhysRevB.67.161310`.

[67] F. P. Laussy, G. Malpuech, A. Kavokin, and P. Bigenwald, Physical Review Letters **93**, 016402 (2004), URL `http://link.aps.org/doi/10.1103/PhysRevLett.93.016402`. 48

[68] A. Berthelot, I. Favero, G. Cassabois, C. Voisin, C. Delalande, P. Roussignol, R. Ferreira, and J. M. Gérard, Nat Phys **2**, 759 (2006), ISSN 1745-2473, URL `http://www.nature.com/nphys/journal/v2/n11/full/nphys433.html`. 48

[69] D. N. Krizhanovskii, K. G. Lagoudakis, M. Wouters, B. Pietka, R. A. Bradley, K. Guda, D. M. Whittaker, M. S. Skolnick, B. Deveaud-Plédran, M. Richard, et al., Phys. Rev. B **80**, 045317 (2009), URL `http://link.aps.org/doi/10.1103/PhysRevB.80.045317`. 48, 63

[70] H. Deng, G. S. Solomon, R. Hey, K. H. Ploog, and Y. Yamamoto, Phys. Rev. Lett. **99**, 126403 (2007), URL `http://link.aps.org/doi/10.1103/PhysRevLett.99.126403`. 48

[71] H. P. Baltes, Appl. Phys. **12**, 221 (1977), ISSN 0340-3793, 1432-0630, URL `http://link.springer.com/article/10.1007/BF00915197`. 48

[72] G. Slavcheva and P. Roussignol, *Optical Generation and Control of Quantum Coherence in Semiconductor Nanostructures* (Springer, 2010), ISBN 9783642124914. 48

[73] A. P. D. Love, D. N. Krizhanovskii, D. M. Whittaker, R. Bouchekioua, D. Sanvitto, S. A. Rizeiqi, R. Bradley, M. S. Skolnick, P. R. Eastham, R. André, et al., Phys. Rev. Lett. **101**, 067404 (2008), URL `http://link.aps.org/doi/10.1103/PhysRevLett.101.067404`. 57, 63

[74] P. R. Eastham and P. B. Littlewood, Phys. Rev. B **73**, 085306 (2006), URL `http://link.aps.org/doi/10.1103/PhysRevB.73.085306`. 57

[75] P. R. Eastham, Phys. Rev. B **78**, 035319 (2008), URL `http://link.aps.org/doi/10.1103/PhysRevB.78.035319`. 59

[76] A. Baas, J.-P. Karr, M. Romanelli, A. Bramati, and E. Giacobino, Phys. Rev. Lett. **96**, 176401 (2006), URL `http://link.aps.org/doi/10.1103/PhysRevLett.96.176401`. 63

[77] E. Wertz, L. Ferrier, D. D. Solnyshkov, R. Johne, D. Sanvitto, A. Lemaître, I. Sagnes, R. Grousson, A. V. Kavokin, P. Senellart, et al., Nature Physics **6**, 860 (2010), ISSN 1745-2473, URL `http://www.nature.com/nphys/journal/v6/n11/full/nphys1750.html`. 63, 70, 76, 92

[78] J. M. Zajac, E. Clarke, and W. Langbein, Applied Physics Letters **101**, 041114 (2012), ISSN 0003-6951, 1077-3118, URL `http://scitation.aip.org/content/aip/journal/apl/101/4/10.1063/1.4739245`. 66, 92

[79] M. Wouters and I. Carusotto, Phys. Rev. B **74**, 245316 (2006), URL `http://link.aps.org/doi/10.1103/PhysRevB.74.245316`. 67, 69, 72

[80] G. Malpuech and D. Solnyshkov, arXiv e-print 1204.2151 (2012), URL `http://arxiv.org/abs/1204.2151`. 67

[81] F. Manni, K. G. Lagoudakis, B. Pietka, L. Fontanesi, M. Wouters, V. Savona, R. André, and B. Deveaud-Plédran, Phys. Rev. Lett. **106**, 176401 (2011), URL `http://link.aps.org/doi/10.1103/PhysRevLett.106.176401`. 69

[82] J. Cuadra, D. Sarkar, L. Viña, J. M. Hvam, A. Nalitov, D. Solnyshkov, and G. Malpuech, Phys. Rev. B **88**, 235312 (2013), URL `http://link.aps.org/doi/10.1103/PhysRevB.88.235312`. 73

[83] K. V. Kavokin, I. A. Shelykh, A. V. Kavokin, G. Malpuech, and P. Bigenwald, Phys. Rev. Lett. **92**, 017401 (2004), URL `http://link.aps.org/doi/10.1103/PhysRevLett.92.017401`. 74

[84] K. Kavokin, P. Renucci, T. Amand, X. Marie, P. Senellart, J. Bloch, and B. Sermage, physica status solidi (c) **2**, 763 (2005), ISSN 1610-1642, URL `http://dx.doi.org/10.1002/pssc.200460313`. 74, 84

[85] A. Amo, T. C. H. Liew, C. Adrados, R. Houdré, E. Giacobino, A. V. Kavokin, and A. Bramati, Nat Photon **4**, 361 (2010), ISSN 1749-4885, URL `http://www.nature.com/nphoton/journal/v4/n6/full/nphoton.2010.79.html`. 74

[86] A. Kavokin, G. Malpuech, and M. Glazov, Phys. Rev. Lett. **95**, 136601 (2005), URL `http://link.aps.org/doi/10.1103/PhysRevLett.95.136601`. 74

[87] C. Leyder, M. Romanelli, J. P. Karr, E. Giacobino, T. C. H. Liew, M. M. Glazov, A. V. Kavokin, G. Malpuech, and A. Bramati, Nature Physics **3**, 628 (2007), ISSN 1745-2473, URL `http://www.nature.com/nphys/journal/v3/n9/full/nphys676.html`. 74

[88] E. Kammann, T. C. H. Liew, H. Ohadi, P. Cilibrizzi, P. Tsotsis, Z. Hatzopoulos, P. G. Savvidis, A. V. Kavokin, and P. G. Lagoudakis, Phys. Rev. Lett. **109**, 036404 (2012), URL `http://link.aps.org/doi/10.1103/PhysRevLett.109.036404`. 74

[89] I. A. Shelykh, T. C. H. Liew, and A. V. Kavokin, Phys. Rev. Lett. **100**, 116401 (2008), URL `http://link.aps.org/doi/10.1103/PhysRevLett.100.116401`. 74

[90] D. Sarkar, S. S. Gavrilov, M. Sich, J. H. Quilter, R. A. Bradley, N. A. Gippius, K. Guda, V. D. Kulakovskii, M. S. Skolnick, and D. N. Krizhanovskii, Phys. Rev. Lett. **105**, 216402 (2010), URL `http://link.aps.org/doi/10.1103/PhysRevLett.105.216402`. 74

[91] C. Adrados, A. Amo, T. C. H. Liew, R. Hivet, R. Houdré, E. Giacobino, A. V. Kavokin, and A. Bramati, Phys. Rev. Lett. **105**, 216403 (2010), URL `http://link.aps.org/doi/10.1103/PhysRevLett.105.216403`. 74

[92] S. Christopoulos, G. B. H. von Högersthal, A. J. D. Grundy, P. G. Lagoudakis, A. V. Kavokin, J. J. Baumberg, G. Christmann, R. Butté, E. Feltin, J.-F. Carlin, et al., Phys. Rev. Lett. **98**, 126405 (2007), URL `http://link.aps.org/doi/10.1103/PhysRevLett.98.126405`. 74

[93] D. N. Krizhanovskii, D. Sanvitto, I. A. Shelykh, M. M. Glazov, G. Malpuech, D. D. Solnyshkov, A. Kavokin, S. Ceccarelli, M. S. Skolnick, and J. S. Roberts, Phys. Rev. B **73**, 073303 (2006), URL `http://link.aps.org/doi/10.1103/PhysRevB.73.073303`. 74, 84, 89, 96, 97

[94] M. Abbarchi, V. Ardizzone, T. Lecomte, A. Lemaître, I. Sagnes, P. Senellart, J. Bloch, P. Roussignol, and J. Tignon, Phys. Rev. B **83**, 201310 (2011), URL `http://link.aps.org/doi/10.1103/PhysRevB.83.201310`. 75, 86, 92

[95] G. Dasbach, C. Diederichs, J. Tignon, C. Ciuti, P. Roussignol, C. Delalande, M. Bayer, and A. Forchel, Phys. Rev. B **71**, 161308 (2005), URL `http://link.aps.org/doi/10.1103/PhysRevB.71.161308`. 75, 86, 92

[96] Ł. Kłopotowski, M. Martín, A. Amo, L. Viña, I. Shelykh, M. Glazov, G. Malpuech, A. Kavokin, and R. André, Solid State Communications **139**, 511 (2006), ISSN 0038-1098, URL `http://www.sciencedirect.com/science/article/pii/S0038109806006211`. 75, 94

[97] A. Brunetti, M. Vladimirova, S. Cronenberger, D. Scalbert, M. Nawrocki, and J. Bloch, Superlattices and Microstructures **41**, 429 (2007), ISSN 0749-6036, URL `http://www.sciencedirect.com/science/article/pii/S074960360700047X`. 75

[98] A. I. Tartakovskii, V. D. Kulakovskii, A. Forchel, and J. P. Reithmaier, Phys. Rev. B **57**, R6807 (1998), URL `http://link.aps.org/doi/10.1103/PhysRevB.57.R6807`. 76

[99] I. A. Shelykh, Y. G. Rubo, G. Malpuech, D. D. Solnyshkov, and A. Kavokin, Phys. Rev. Lett. **97**, 066402 (2006), URL `http://link.aps.org/doi/10.1103/PhysRevLett.97.066402`. 86

[100] M. Glazov, I. Shelykh, G. Malpuech, K. Kavokin, A. Kavokin, and D. Solnyshkov, Solid State Communications **134**, 117 (2005), ISSN 0038-1098, URL `http://www.sciencedirect.com/science/article/pii/S0038109804010257`. 86

[101] D. D. Solnyshkov, I. Shelykh, M. Glazov, G. Malpuech, T. Amand, P. Renucci, X. Marie, and A. Kavokin, Semiconductors **41**, 1099 (2007). 89, 96